Summer 2010

In vivo non-invasive monitoring of optically resonant metal nanoparticles using multi-wavelength photoplethysmography

Gregory J. Michalak

IN VIVO NON-INVASIVE MONITORING OF OPTICALLY RESONANT METAL NANOPARTICLES USING MULTI-WAVELENGTH PHOTOPLETHYSMOGRAPHY

by

Gregory J. Michalak, B.S.

A Dissertation Presented in Partial Fulfillment
of the Requirements for the Degree of
Doctor of Philosophy

COLLEGE OF ENGINEERING AND SCIENCE
LOUISIANA TECH UNIVERSITY

August 2010

UMI Number: 3532946

UMI®

Dissertation Publishing

ProQuest®

LOUISIANA TECH UNIVERSITY

THE GRADUATE SCHOOL

May 10, 2010
_____
Date

We hereby recommend that the dissertation prepared under our supervision

by Gregory Michalak
_____

entitled_____

In Vivo Non-invasive Monitoring of Optically Resonant Metal Nanoparticles

Using Multi-Wavelength Photoplethysmography

_____

_____

be accepted in partial fulfillment of the requirements for the Degree of

Doctor Of Philosophy in Biomedical Engineering
_____

_____
Supervisor of Dissertation Research

_____
Head of Department

Biomedical Engineering
_____
Department

Recommendation concurred in:

Sandra Zivanovic
_____

_____

_____

Advisory Committee

Approved:
_____
Director of Graduate Studies

_____
Dean of the College

Approved:
_____
Dean of the Graduate School

GS Form 13a
(6/07)

ABSTRACT

Nanotechnology has recently emerged as a powerful modality in many biomedical applications. In particular, several classes of nanoparticles have been employed as cancer therapy and imaging contrast agents. These particles can have architecture of varying complexity, depending on their specific application. These complex architectures are achieved by various chemical techniques usually performed in specific sequences to add complexity and functionality. One such class of nanoparticle, used in tumor treatment and as contrast agents in several optical imaging techniques, is the plasmon resonant metal nanoparticle. The most common metal used for these particles is gold because of its biocompatibility, lack of cellular toxicity, and simple surface chemistry. These particles have specific optical properties in the near infrared spectrum making them ideal for modern cancer therapy and optical imaging. Two examples of these particles are gold nanoshells and gold nanorods, both of which are highly absorptive and scattering at near infrared wavelengths. It is for this reason that they are often employed in photo thermal ablation of tumors using near infrared light. In this type of tumor treatment, the particles are injected intravenously and accumulate in the tumor. After accumulation, a near infrared laser is used to heat the particles and destroy the tumor.

These gold nanoparticles must be modified with biocompatible "stealthing" compounds before they can be injected. This is because of the high efficiency of the body's reticuloendotheial system, which will quickly eliminate materials foreign through

cellular phagocytosis. Although techniques for quality control in manufacturing these nanoparticles are used to confirm proper surface modification, their *in vivo* behavior is very difficult to predict. It is for this reason that real time feedback in nanoparticle therapy is an urgent need and will greatly improve its efficacy.

This dissertation reports the development of a non-invasive optical system capable of reporting the *in vivo* vascular concentration of these nanoparticles in near real time. The device, termed the pulse photometer, utilizes a technique similar to that used in pulse oximetry. This technique is photoplethysmography, which has many medical applications. One of these is determining the optical characteristics of pulsatile arterial blood, which are affected after the injection of these optically resonant particles. Several prototypes of this are presented in this dissertation. The culmination of this work is the prototype III pulse photometer capable of concurrent nanoparticle monitoring and oximetry. Final testing of this prototype revealed its ability to accurately determine the vascular optical density of gold nanorods compared to *ex vivo* spectrophotometry, a technique also verified in this dissertation, by statistical Bland-Altman analysis.

APPROVAL FOR SCHOLARLY DISSEMINATION

The author grants to the Prescott Memorial Library of Louisiana Tech University the right to reproduce, by appropriate methods, upon request, any or all portions of this Dissertation. It is understood that "proper request" consists of the agreement, on the part of the requesting party, that said reproduction is for his personal use and that subsequent reproduction will not occur without written approval of the author of this Dissertation. Further, any portions of the Dissertation used in books, papers, and other works must be appropriately referenced to this Dissertation.

Finally, the author of this Dissertation reserves the right to publish freely, in the literature, at any time, any or all portions of this Dissertation.

Author _____

Date _____

TABLE OF CONTENTS

LIST OF TABLES

LIST OF FIGURES

ACKNOWLEDGEMENTS

First and foremost, I want to thank all of my family and friends for their support during my time here at Louisiana Tech. I would not have become interested in math and science early in my life and would not have become a biomedical engineer if it had not been for my parents. My siblings were always very supportive and would keep in touch with me from far away in Milwaukee, Wisconsin. My brother, Tyler, studied with me for three years at Tech and was my roommate for two of those years. My brother, Adam, my Dad, and my Mom came to visit several times to help get my mind off of research and to give me some familiar company.

Secondly, I want to thank all of the members of my committee: Dr. Patrick O'Neal, Dr. Katie Evans, Dr. Eric Guilbeau, Dr. Alan Chiu, and Dr. Sandra Zivanovic. Dr. O'Neal provided financial support for me to build my instruments and perform my experiments and oversaw my research as my advisor. Dr. Evans, Dr. Chui, and Dr. Zivanovic each gave me guidance and support during my graduate research and served as valuable instructors. Dr. Guilbeau offered to help get me in touch with other schools in search of a post-doctoral position. Each member provided very constructive and useful feedback during my dissertation defense.

I would like to thank Dr. James Spaulding for his help with care and use of the animals used in my experiments. He also helped us draft protocols for anesthesia and got them

CHAPTER 1

INTRODUCTION

1.1 Nanoparticles in Cancer Treatment

Nanotechnology has emerged as a powerful tool in many medical applications. In

particular, many research groups have turned to using nanoparticles in the imaging,

sensing, and treatment of cancerous tumors. These nanoparticles can be designed and

manufactured to be multi-functional, often having complex architecture and unique

properties advantageous to their specific function. These particles are manufactured

using a variety of assembly techniques such as colloidal and printing chemistries, layer-

by-layer electrostatic assembly techniques, self-assembled monolayers, and conjugate

immuno-chemistry [1-5]. Often their *in vivo* and *in vitro* activity can be tailored by

modifying their size, surface, and composition. This necessitates the use of a variety of

characterization methods in nanoparticle manufacturing to ensure that these

characteristics are achieved. These include techniques such as electron microscopy, light

scattering and spectroscopic techniques, and chemical assays to detect surface modifying

compounds.

In the treatment of tumors, it is essential that nanoparticles be designed that will

effectively deliver treatment, whether it is a drug or the nanoparticle itself, to the tumor

preferentially to avoid collateral damage to normal tissue. This is often a complication of

treatments such as conventional chemotherapy and radiation, where patients undergoing

these treatments are subjected to unpleasant side effects. Preferential treatment of tumors is often achieved by using a targeting scheme where the particle has a specific affinity for the tumor. This scheme can be either employ active or passive targeting. *Passive targeting* often consists of exploiting the specific anatomy of certain types of tumors, making them susceptible to the preferential accumulation of the particles. For example, certain tumors have abnormal vascular organization because of the hyperactive angiogenesis associated with uncontrolled cellular proliferation. This results in characteristically defective and leaky blood vessels supplying nutrients to the tumor cells. Manufacturing therapeutic nanoparticles smaller than these defects allows them to passively accumulate in tumor tissue, a phenomenon referred to the enhanced permeability and retention effect (EPR). *Active targeting* refers to the attachment of biochemically active compounds with specific affinity for cells expressing oncoprotiens at their surface. For example, epidermal growth factor receptor (EGFR) is a transmembrane protein that responds after binding to its specific ligand epidermal growth factor (EGF) by sending proliferative signals to the interior of the cell. There is evidence that in up to one third of carcinomas, this protein is over expressed and is often mutated causing it to lose its ligand binding specificity and/or in some cases uncontrolled release of proliferative signals to the cell without binding to any ligand [6]. In one study [7], monoclonal anti-EGFR antibodies were conjugated to 30 nm diameter hollow gold nanoshells, giving the nanoshells specific affinity for EGFR. *In vivo* and *in vitro* performance was assessed by comparing the activity of the modified nanoparticles with IgG labeled nanoparticles, with no specific affinity for EGFR. *In vitro* analysis was performed in cell culture using A431 human squamous carcinoma cells. Microscopy

revealed preferential attachment of the anti-EGFR nanoparticles to the cancer cells and

minimal attachment of the IgG nanoparticles. *In vivo* performance was assessed using

subcutaneous tumors grown in mice after injection of the cancer cell line. The two types

of nanoparticles were injected intravenous and tissue examination was performed to

determine the biodistribution of the nanoparticles. Tissue analysis revealed increased

uptake in the tumors treated with anti-EGFR nanoparticles compared to IgG labeled

nanoparticles.

1.2 Physiological Response to Nanoparticles

Another important issue to address in nanoparticle therapy is the response of the

body to these foreign objects. Unmodified nanoparticles, when introduced to the body

intravenously, will elicit an immune response resulting in rapid removal. Depending on

the size and composition of the nanoparticles, this can be either via renal excretion if the

particles are small enough, or cell mediated by the reticuloendotheial system (RES).

Primarily, the nanoparticles are removed from the vasculature by tissue macrophages in

the liver and spleen called Kupffer cells. These cells can quickly identify and eliminate

nanoparticles via phagocytosis. Complete removal of nanoparticles can often be

achieved in a matter of minutes, resulting in minimal tumor accumulation and therapeutic

value.

To avoid this unwanted removal, the surface of nanoparticles can be modified

with certain compounds that allow the particles to become invisible to the RES. This is

possible because what is presented on the surface of nanoparticles determines the

response of the RES. These modifications are usually in the form of polymers linked to

the surface of the particles, the most common of which is poly(ethylene glycol) (PEG).

The attachment of PEG has been shown to dramatically increase the circulation time of several types of nanoparticles, which is usually reported as the circulation half-life of the particle assuming an exponential decay in concentration over time. One recent report [8] demonstrated the manufacture of PEG coated carbon nanotubes having a circulation half life of 22.1 hours using a specific linking chemistry, a dramatic increase compared to what was previously achieved. Increased circulation and stability as well as reduced cytotoxicity of CTAB stabilized gold nanorods has been demonstrated by using PEG surface modification [9]. The PEG modification was achieved by a simple wet chemistry technique using thiol modified 5 kD PEG that readily binds to gold, thus stabilizing the particles and reducing surface charge. The effects of different degrees of PEG coating on gold nanorods has also been investigated [10]. This report demonstrated increased RES avoidance and tumor accumulation in murine models with increased PEG/Au molar ratios.

1.3 Classes of Optically Resonant Nanoparticles

One class of nanoparticles that has become particularly popular in many biomedical applications is metal nanoshells (NS) [11]. These nanoparticles usually consist of a dielectric core surrounded by a metal shell. Gold is the most often used metal to build these particles. They have vast utility in biomedical applications mainly because of their optical properties and biocompatibility. Many bulk metals exhibit a phenomenon called plasmon resonance which occurs when light at particular wavelengths interacts with oscillating conducting electrons, called surface plasmons, in the metal near the surface. Most of these resonances occur when visible light interacts with the surface, causing extremely high absorption and scattering of light at these wavelengths. Metal

NS, because of their geometry, can be tuned to interact with light at wavelengths spanning from the visible to infrared (IR) by changing the ratio of the NS's core diameter to shell thickness [12]. This is advantageous because *in vivo* biomedical applications of optics often use near infrared (NIR) wavelengths because of their ability to penetrate tissues much more effectively than visible light, reaching penetration depths of up to 15 cm. These particles have been found useful in biomedical applications like immunoassays, optically responsive hydrogels, photo thermal ablation (PTA), and imaging contrast agents.

Gold nanorods (NR) are another type of optically resonant nanoparticle. These particles are rod shaped like the name suggests and also have optical resonances in the NIR spectrum. They too have high absorption and scattering cross sections and are useful in many of the same applications as NS. Gold NR, like NS, are optically tunable and can have peak optical densities ranging from the visible to NIR [13]. This is dependent on the aspect ratio of the particle (the ratio of its longitudinal dimension to its transverse dimension). The higher the aspect ratio, the more red shifted its primary extinction peak.

1.4 Applications of Metal Nanoshells and Nanorods

PTA is a cancer treatment modality using preferential heating of tumor tissue to the point of irreversible cell damage by illumination with a light source. NIR extinguishing gold NS can be used in PTA to enhance absorption and localized heating in tissues where they collect. In the treatment of tumors, NS can be injected in the vasculature and extravasate at the tumor site. Once optimal NS collection is achieved, a laser emitting a wavelength corresponding to its resonant wavelength is used to irradiate

the tumor. The absorption of this energy causes a localized significant increase in temperature, causing damage to the cells in the tumor but leaving tissues not containing NS unaffected. This localized NS enhanced heating during PTA has been modeled and confirmed when compared to magnetic resonance temperature imaging (MRTI) [14]. Effective treatment of superficial tumors from several cell lines in mice has been demonstrated using NS enhanced PTA in several reports [96,97,15,16]. Mild hyperthermia in tumors has also been demonstrated using gold NS enhanced PTA. Often the core of tumors becomes hypoxic because of the rapid metabolism of the expanding outer tissue and defective vasculature due to mutation. This hypoxia has been found to increase the resistance of cancer cells to radiation therapy. These resistant cells are thought to be one of the causes of tumor recurrence. A study exploring the effects of tumor treatment using a combination treatment of mild hyperthermia with radiation treatment showed that a significant increase in tumor core temperature could be achieved using NS enhanced PTA [17], thus increasing blood flow and reducing cellular hypoxia making the cells more susceptible to radiation treatment. The coupling of this hyperthermia treatment with conventional radiation treatment caused significant decrease in tumor growth rate as compared to radiation treatment alone.

PTA has also been reported using gold NR. One report described the use of gold NR as an integral part of a multi-nanoparticle based system for the treatment of tumors [18]. The system was comprised of gold NR coupled with either peptide labeled magnetic nanoworms or liposomes. The liposomes were loaded with the anticancer drug doxorubicin. The NR served the purpose of acting as NIR antennas for the photo thermal sensitization of tumors. The sensitization entailed heating of the tumors which would

cause amplification of an already over expressed stress protein receptor, p32, seen in MDA-MB-435 cancer cells. The liposomes and nanoworms were modified with a LyP-1 peptide chain, a ligand for the p32 receptor. Heating of the tumors coupled with injection of either therapeutic nanoparticle was shown to cause a significant increase in tumor accumulation. Gold-silver NR have also been synthesized and proven feasible for use in PTA for tumor treatment [19]. The gold-silver NR were targeted to a specific cancer cell line using a novel approach employing aptamers and showed excellent specificity in binding to only cancer cells. In vitro PTA was performed showing preferential killing of cancer cells as compared to control cells. NR's have also been proven useful in killing pathogenic bacteria using antibody enhanced cell targeting and photo thermal lysis [20]. This has the potential to serve as an alternative method of treatment in patients with drug resistant bacterial infections. Photo thermal activation of polymer gels has also been shown to be achieved using gold NR. One study reported the production of nanogels assembled on gold NR templates [21]. The NR served as an activator of the gel when irradiated with an NIR laser, causing change in the hydrophobicity and size of the gel. This could have applications in controlled drug release. A similar scheme employed coating NR with polyelectrolytes for the stabilization of the NR and delivery of DNA plasmids to human prostate cancer cells [22].

Nanoshells and nanorods are also effective as contrast agents in imaging modalities such as microscopy and optical coherence tomography (OCT) [23]. Because of their high scattering cross section, nanoshells add contrast to dark field microscope images. This has been used to visualize the preferential binding of antibody conjugated nanoshells to specific cancer cell lines in vitro [7,97]. Contrast enhancement due to

increased light scattering has also been shown in OCT images of tumors after intravenous injection and accumulation of nanoshells [24].

1.5 Monitoring of Nanoparticle Therapy

One important issue in cancer treatment with nanoparticles is treatment monitoring. Researchers need to know the bioavailability and biodistribution of the nanoparticles in order to ensure that they reach the desired anatomical location. Non-invasive monitoring of gold nanoshell accumulation in tumors has been demonstrated with the use of diffuse reflection spectroscopy capable of rapidly determining nanoshell concentration [25]. This technique showed good agreement with *ex vivo* analysis of tumor tissue and offered a technique for real time assessment of tumor accumulation. *In vivo* monitoring of nanoparticle activity in the vasculature is possible through the use of invasive techniques that require blood draws, but this information is not obtainable in real time. A standard accepted method of determining gold concentration with instrumental nuclear activation analysis (INAA) has been shown to be effective in determining the biodistribution of gold nanoshells [26]. However, this technique requires the use of a neutron source to convert the gold in the sample into its radioactive gamma emitting isotope. This type of analysis almost always warrants sending samples off site, delaying the analysis of biodistribution often times by weeks. This is not an acceptable situation in dealing with eventual patient treatment. One method exploiting the scattering properties of NS was proposed as a solution to monitoring their vascular concentration [27]. This method employed dynamic light scattering (DLS) analysis of blood samples mixed with a surfactant, Triton-X 100. The surfactant served two purposes. The first was to lyse the cellular components of the sample that would interfere with the scattering of light in the

sample. The second was to add a small reference scattering signal for comparison to the scattering signal from the NS. Empirical techniques were used to calibrate a particular DLS system to correlate the ratio of scattering signals between NS and Triton-X with the NS concentration in the sample. The technique showed good correlation with INAA and offered the possibility for determining NS concentration within minutes. The short analysis time of each sample allowed for near real time evaluation of NS circulation time and quick evaluation of individual batches. However, DLS is very susceptible to sample contamination requiring careful and reproducible blood drawing and sample preparation, and is not feasible for clinical use. There has been a report of *in vivo* non-invasive optical monitoring of PEG and CTAB modified gold NR in mice using a spectrometer coupled to an integrating sphere [28]. A mouse could be placed on a PMMA window over the integrating sphere and absorbance spectra after NR injection could be obtained. This report demonstrated optical tracking of NR in the mouse abdomen showing dramatically increased clearance of non-PEG modified NR as compared to PEG-modified NR. However, the device consisted of several expensive optical instruments and the animal could only be monitored for as long as it was under anesthesia. A background spectrum of the normalized scattered light was also required before injection and the spectrum did not supply the actual vascular NR concentration. Regardless of its imitations, this technique proved that it was possible to track optically extinguishing nanoparticles using NIR light.

Non-invasive real-time monitoring of the vascular concentration of nanoparticles will be essential for the progression of these therapies to human use. This dissertation addresses this issue by presenting the development of a non-invasive optical device

capable of determining optically active nanoparticle concentration in murine models. The system is designed to be compatible with a plethora of different nanoparticles with the only requirement being that they have an acceptable optical density (OD) in the NIR spectrum. Using techniques similar to pulse oximetry, this newly developed modality is achieved by adapting the principles of photoplethysmography for the spectral analysis of arterial blood. The device is comprised of off-the-shelf opto-electronics and integrated circuitry coupled to signal analysis in LabVIEW. Optical probes have been developed for murine models, but are also compatible with optically accessible locations of the human anatomy. In this dissertation, validation of this device is achieved through *in vivo* testing of its performance with both NIR extinguishing gold NS and gold NR.

CHAPTER 2

LITERATURE REVIEW

2.1 Photoplethysmography

The plethysmogram is a physiological signal that arises from the small change of volume in tissue due to pulsation. This signal can be measured using visible and infrared light by measuring small changes in its reflectance or transmission. Measuring this signal using the technique of detecting light is called photoplethysmography (PPG) and has many applications in physiological monitoring [29].

Since the optical properties of the pulsatile tissue are determined by its individual components, PPG can be used to gain spectral information about the pulsatile constituents of the tissue. An entire mass of perfused tissue will contain optically extinguishing components that are relatively constant in volume such as muscle, bone, and venous blood, and those that are not constant such as pulsing arterial blood. In examining the small changes in the attenuation of light interacting with the tissue, the contribution of only arterial blood is isolated from the other components. It is for this reason that PPG is applicable to the analysis of the optically extinguishing properties of arterial blood. A graphical illustration of the transmission style measurement of this pulsatile nature of tissue can be seen in Figure 1.
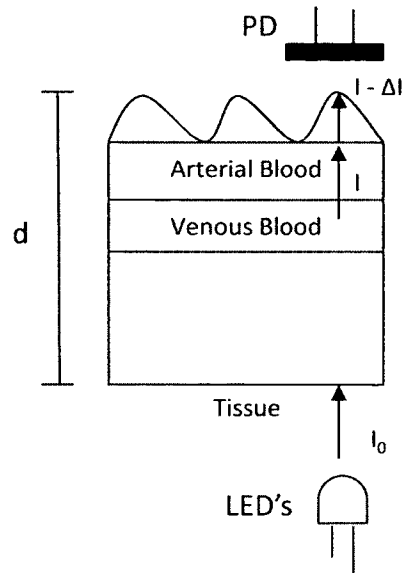
Figure 1. The extinction and transmission of light in tissue containing pulsating arterial blood and non-pulsating tissue

I_0 is the incident intensity of light on the tissue. I is the intensity of light that emerges from the non-pulsatile tissue and ΔI is the small change in the intensity of emerging light that results from a small increase in optical path length due to the injection of additional arterial blood into the medium during a heartbeat.

2.2 Pulse Oximetry

The earliest application of PPG was pulse oximetry, which was first developed by Takuo Aoyagi and Michio Kishi of the Nihon Kohden Corporation in Japan [30]. This is an optical technique that interrogates pulsatile tissue to measure arterial blood oxygen saturation (SpO_2). In his attempts to measure blood oxygen saturation using non-pulsatile attenuation of light, he noticed that his measurements were confounded by a repetitive change in the attenuation of light due to the pulsing arterial blood. He later found that he could use that signal to measure only properties of arterial blood and

eliminate the contribution of other attenuating tissue. Exploiting the fact that oxygenated

(HbO$_2$) and reduced hemoglobin (HbR) have different extinction spectra at visible and

infrared wavelengths, he determined that the change in attenuation due to the small

change in path length resulting from pulsation would be dramatically different at a visible

and infrared wavelength. This measurement could be used to determine the degree of

oxygenation of arterial blood. The spectra of HbO$_2$ and HbR can be seen in Figure 2 .
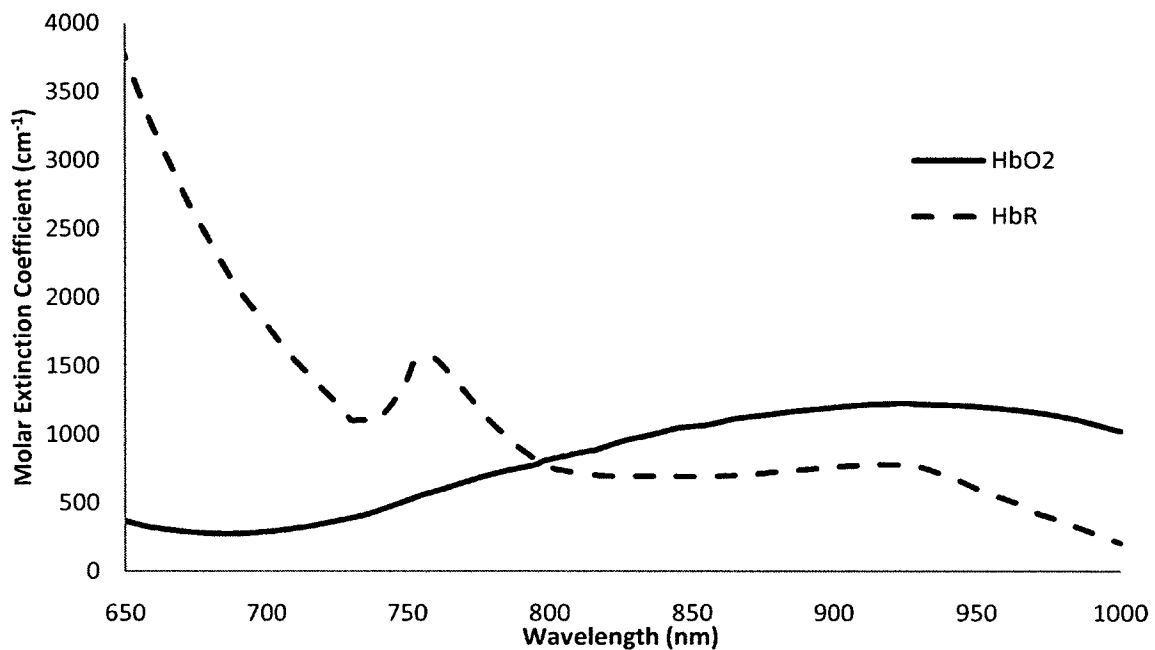
Figure 2. Molar extinction coefficients of HbO$_2$ and HbR.[31]

HbO$_2$ attenuates infrared light more so than red light, and therefore appears red.

HbR attenuates red light more so than infrared, and therefore appears a darker bluish red.

Aoyagi determined that in order to obtain the largest difference in optical attenuation

between two wavelengths, he would need to choose one red wavelength which would be

most affected by HbR, and one infrared wavelength which would be most affected by

HbO$_2$. His first choices of the wavelengths were 630 nm and 900 nm. As the arterial

blood became more or less oxygenated, the resulting spectrum of the blood would change, and therefore so would the magnitude of the change in attenuation at each wavelength. By using a ratio of the pulsing attenuation at each wavelength, and by applying the Beer-Lambert law (often referred to as Beer's law), several things could be accomplished. The first is that Beer's law states that the extinction of light (given in absorbance units or OD) was proportional to the attenuation coefficient of the medium and its optical path length. By using a ratiometric technique, the calculations would become path length independent. Secondly, since he only wanted to measure variants of the hemoglobin present in the arterial blood, the calculations would become concentration independent. Therefore, the degree of blood oxygenation was only dependant on the measured value of the ratio of extinction changes, often referred to as R, and on the molar extinction coefficients of HbO_2 and HbR (see APPENDIX A). R can be calculated using the DC and AC portions of the plethysmogram, which when collected using a photodetector circuit can be found using the voltage resulting from the induced photocurrent due to the changing intensity of light.

$$R = \frac{\log(\frac{V_{DC}}{V_{DC} - V_{AC}})_{\lambda_1}}{\log(\frac{V_{DC}}{V_{DC} - V_{AC}})_{\lambda_2}} \sim \frac{\left(\frac{V_{AC}}{V_{DC}}\right)_{\lambda_1}}{\left(\frac{V_{AC}}{V_{DC}}\right)_{\lambda_2}}$$

The molar extinction coefficients of HbO_2 and HbR are well known [31,32]. However, hemoglobin is not the only attenuating substance in whole blood. The presence of cells in whole blood causes scattering of light as it propagates through the tissue. This changes the apparent molar extinction coefficient of HbO_2 and HbR and complicates the measurement of SpO_2.

To avoid the problem of many confounding variables in the theoretical calculation of SpO_2, developers of pulse oximeters turned to empirical calibration of their devices [33]. A co-oximeter, which is a device that uses spectrophotometry to measure the relative blood concentrations of the variants of hemoglobin *ex vivo*, was used to calibrate the pulse oximeters to develop a relationship between R and SpO_2. It was found that a consistent value of R could be measured for a given oxygen saturation. Therefore, lookup tables depending on the particular wavelengths used were developed. Manufacturers of pulse oximeters would develop these tables and use them to calibrate their proprietary devices. This method is still used even in modern day pulse oximeters.

2.3 Physiological Measurements Using PPG

Reflectance PPG has been used to assess cardiovascular function by monitoring the shape and repetitive nature of pulses [34]. Abnormal heart beats and abnormal responses to physical stress can be detected by PPG. Assessment of the shape of pulses detected at different body locations can help locate areas of local vascular occlusion. Multiwavelength reflectance PPG has also been used to assess tissue pulsations at different depths [35]. This is possible because of the different penetration depths of various wavelengths. Different signal shapes have been observed for different wavelengths based on their penetration depth. The signal shape can be used to determine which layer of tissue is being examined. For example, long penetrating infrared and short penetrating visible reflections showed much a much less pronounced dichrotic notch than did near infrared light reflections. This was speculated to be due to the different dynamics of various layers of pulsating tissue. A similar technique has been used to separate skin pulsation and underlying muscle pulsation to determine their relative

perfusion [36]. An optical setup using a near infrared emitter situated far from the detector and a visible emitter situated near the detector was used. The near infrared light was used to monitor the pulsation of the muscles due to its larger penetration depth, and the visible source was used to measure the superficial skin pulsation due it its smaller penetration depth. This was illustrated by increasing blood flow to the muscles by static contraction and measuring increased pulse amplitude in only the near infrared signal. The opposite was true with the application of liniment, where pulsation of only the visible light increased. The light penetration, pulse amplitude, and heart rate determined by PPG have also been used to assess local blood volume and its low frequency fluctuation [37]. This can be used to gain information about the influence of the nervous system on regulating several cardiovascular parameters like blood pressure and vessel compliance.

The use of PPG in conjunction with laser Doppler flowmetry (LDF) was applied to the assessment of patient risk for pressure ulcers by detection of reactive hyperemia [38]. In this study, a probe was fabricated on a rigid plate housing green and infrared LED's, an LDF fiber, and a photodetector. This was placed on the sacrum of several patients and used to measure blood flow at different tissue depths before, during, and after loading the tissue. The green LED's and LDF were used to assess superficial blood flow while the IR LED's were used to assess flow in the deeper tissues and blood vessels. Blood flow was assessed relative to baseline readings when no load was applied to the sacrum. Increases in the pulse amplitude in the PPG readings meant an increase in blood flow, and decreases meant reduced blood flow. The study revealed that PPG coupled

with LDF could be used to measure blood flow at different tissue depths and was helpful

in identifying blood flow dynamics during and after pressure is applied to tissue.

The measurement of arterial blood glucose has been measured using PPG [39].

This was achieved by the spectral analysis of pulsatile blood at wavelengths between 900

and 1700 nm, where glucose has several absorption bands. A multiple regression model

was then developed using several spectral parameters and tested. PPG allows only the

analysis of arterial blood and therefore arterial glucose concentration was measured. In

ex vivo measurements, venous glucose is sampled and is typically 10-20 % lower than

arterial blood. Nevertheless, Bland-Altman and error grid analysis revealed that this

technique could measure blood glucose concentration with clinically acceptable accuracy.

The use of PPG has been demonstrated in pediatric dentistry. Pulpal blood flow was

assessed in a pilot study where the pulsatile signal from permanent teeth was obtained

[40]. Simultaneous recordings of finger and tooth PPG signals were recorded and

compared when examining vital and non-vital teeth. It was found that no pulsatile signal

could be obtained from non-vital teeth and a pulsatile signal could be obtained from vital

teeth. Thus, a technique for non-invasive optical assessment of pulpal vitality was

proven feasible.

Systolic blood pressure (SBP) has been measured using PPG. One study used a

transmission infrared oximetry probe to detect the disappearance and reappearance of the

photoplethysmogram in the finger as a proximal pressure cuff applied pressure above and

below the SBP [41]. The photoplethysmogram would disappear as the cuff was inflated

to a pressure above the SBP. Then, the cuff was slowly deflated until the

photoplethysmogram reappeared. The reappearance was determined by two parameters.

The first was an integral of the pulse signal which was compared to a threshold value, and the second was a cross correlation with the pulse waveform in adjacent segments. The results of testing this technique were compared to two standard methods of blood pressure measurement, sphygmomanometry and oscillometry. The comparisons showed good agreement between the measurements. A similar technique was demonstrated using a reflection probe modified to fit the ankle [42]. A pressure cuff placed proximal to the ankle was used to occlude the tibial arteries and the pressure was decreased until the pulses could be seen in both the anterior and posterior tibial arteries. This technique was compared to Doppler ultrasound and to invasive intra-arterial blood pressure measurement and showed good correlation. The purpose of using PPG at the ankle was to assess feasibility of measuring a parameter called ankle-brachial pressure index, which is an important follow up measurement in patients with leg ischemia and is a good indicator of atherosclerosis in the legs.

2.4 Pulse Dye Densitometry

An application of PPG that has recently been developed is pulse dye densitometry (PDD). This is a technique designed to estimate cardiac output, blood volume, and hepatic clearance rate by examining the removal of an injected dye. This is done by choosing a dye with a circulation half life on the order of minutes with an extinction spectrum having a peak value in the near infrared spectrum, injecting it intravenously, and tracking its concentration using near infrared light.

In PDD, the pulsatile arterial blood is examined just as in pulse oximetry. The ratio of the change in absorbance at several wavelengths is used to calculate the concentration of the injected dye over time by using the attenuating properties of reduced

and oxygenated whole blood and the molar extinction coefficient of the dye. In the first pulse dye densitometers, two wavelengths were used just as in pulse oximetry. One of these wavelengths was chosen to match the spectrum of the injected dye, and the other was chosen to find the contribution of the pulsatile signal due to hemoglobin. The near infrared absorbing dye, indocyanine green (ICG), is the most commonly used dye in PDD because of its extinction spectrum with a peak at 805 nm and its rapid hepatic clearance (4.1 min half life). It is also accepted as a non-toxic dye for human use. In most two wavelength PDD systems, 890 nm is used as the hemoglobin sensitive wavelength. Contrary to pulse oximetry, PDD uses different wavelengths of light to determine dye concentration. In systems using ICG, 805 nm is the wavelength of choice to help determine dye concentration. The HbR sensitive wavelength chosen is most often 890 nm since the extinction spectrum of ICG is negligible at this wavelength and the extinction coefficients of HbO_2 and Hb are very similar. This is done to reduce the effects of oxygenation on the measurement of ICG concentration. Upon injection of ICG, a change in R is measured and used to determine its concentration. While ICG is circulating, the pulse dye densitometer plots the concentration of ICG over time. A typical dilution curve constructed using the prototype III pulse photometer presented in this dissertation (explained in Chapter 5), the molar extinction coefficient of ICG, and empirically derived whole blood constants can be seen in Figure 3.

The chart shows ICG Concentration (mM) on the y-axis ranging from -0.1 to 0.7, and Time (min) on the x-axis ranging from 0 to 16.

$$y = 0.28689e^{-0.24241x}$$
$$R^2 = 0.98263$$
$$HL = 2.8 \text{ min}$$
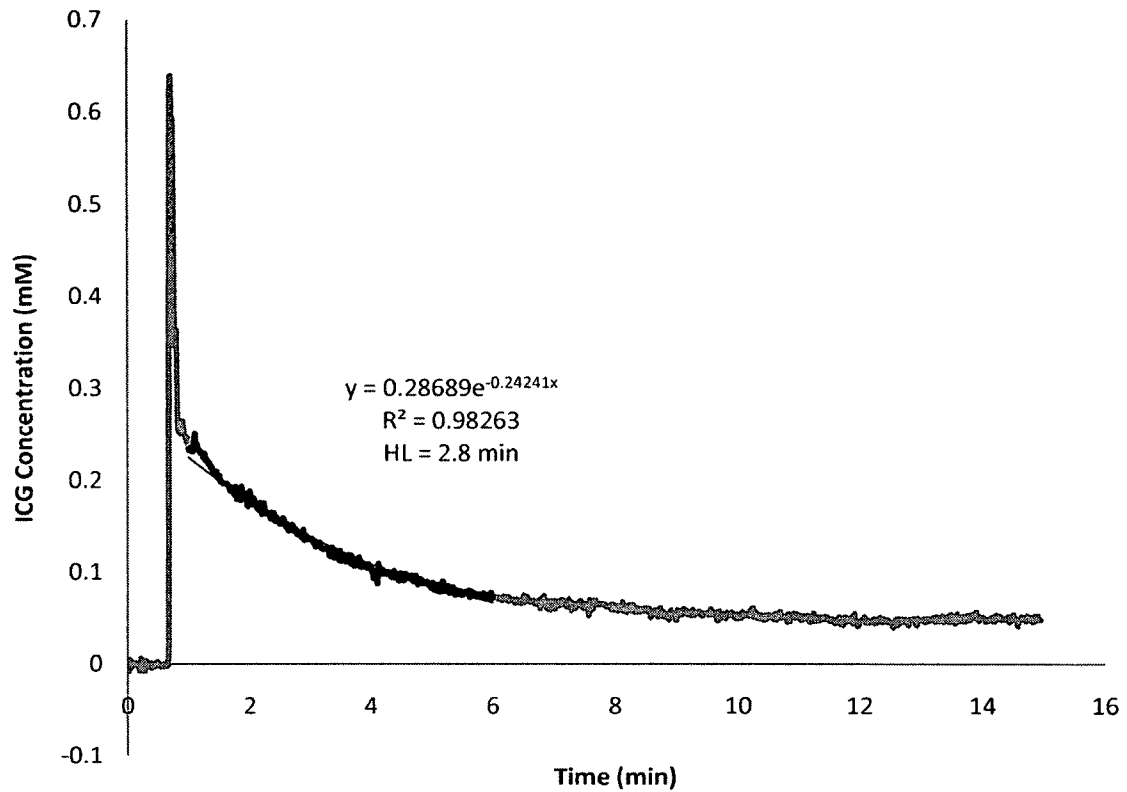
Figure 3. ICG clearance curve taken from a female BALB/c mouse showing a 2.8 minute circulation half life.

Cardiac output (CO) can be determined by dividing the total amount of ICG injected by the integral of its concentration over time. Circulating blood volume (CBV) is computed by dividing the initial injected dose of ICG by the initial concentration found by determining the slope of the clearance curve of ICG and back extrapolating it to its estimate after the mean transit time.

The earliest report of the use of PDD for measuring cardiac output and circulating blood volume was published in 1997 [43]. In this study, good agreement between ICG concentrations measured by PDD and by *ex vivo* spectrophotometry was demonstrated. Cardiac output determined by PDD was compared to the spectrophotometric method and

to thermodilution and also showed good agreement. However, comparison of CBV using PDD and an empirical calculation using the height and weight of each subject showed a large discrepancy between the measurements. This could have resulted from errors in the calculation of ICG concentration or from errors in determining the initial concentration of ICG just before the beginning of hepatic elimination.

The algorithm used in this first PDD prototype was based on Beer's law and modified using Schuster's Theory for radiation in a highly scattering medium [44]. This also included the contribution of the total optical density of the medium by pulsating tissue as well as pulsating arterial blood. The assumptions of these calculations were that the contribution of the tissue was constant throughout the experiment, and that the molar extinction coefficients of oxygenated and reduced blood were equal at 890 nm. The ICG measurement protocol called for the measurement of the tissue optical density before the injection of ICG. This value was used in all ICG measurements after the injection, but may have varied with time causing inaccuracies. The attenuation of oxygenated and reduced whole blood is also not exactly equal at 890 nm. If blood oxygenation was not stable during the experiments, this would have caused shifting hemoglobin background measurements and inaccuracies in ICG concentration estimates.

Probe placement was a topic of discussion in this first study. As in pulse oximetry, the photoplethysmogram can be obtained from several optically accessible locations. Finger probes were initially used for the detection of an acceptable pulsatile signal. In the case of weak pulse amplitude measurement at the finger, the probe was moved to the nose, where a stronger pulse could be obtained. The report gave examples of dye dilution curves obtained from both the finger and the nose. The authors reported

that in general the curves obtained by probing the finger tended to contain more noise. The change in the signal due to the presence of ICG was also less sharp and occurred later when compared to the signals measured at the nose. This made the identification of the first point after the mean transit time difficult and may have lead to the errors in CBV estimation.

The use of PDD in measuring blood volume in patients who had undergone cardiac surgery was assessed [45]. This was an important study because recovering patients are especially in need of accurate monitoring. CBV was determined in 11 patients who had undergone cardiac surgery for a variety of reasons using both PDD and a standard CBV measurement technique using radioactively tagged erythrocytes. PDD measurements were performed on both the finger and nose to assess variability due to probing location. Comparison of measurements at the same probe location for successive CBV measurements showed good repeatability, however there was some discrepancy between probe location measurements. The authors claimed that this may have been due to variations in tissue contribution to the pulsatile signals. CBV measurement by PDD at both locations showed acceptable agreement with the radioactive erythrocyte technique, thus providing evidence that PDD could be used to accurately measure CBV in critically ill patients.

Another study compared the measurements of CO and CBV using the finger and nose probes and found that PDD was not acceptable as a means for cardiovascular monitoring [46]. This assessment was made based on large variance in the measurements of both variables. The authors again claimed that the performance of PDD probably suffered from patient variables leading to low perfusion at the probes sites. They

suggested that variables such as probe site temperature, vasoconstriction, ambient light and signal strength be more tightly controlled in order to enhance signal quality. PDD has been used to monitor the change in blood volume during microgravity simulation by Head-Down-Tilt (HDT) bed rest over a period of 90 days [47]. This is applicable to monitoring CBV in astronauts who undergo long periods in space. HDT has been shown to cause significant decreases in plasma volume. PDD and Dill and Costill's (DC) equation were used to determine plasma volume before, during, and after HDT in 17 patients. Both methods showed significant decreases in plasma volume after 90 days of HDT. PDD showed good repeatability, although there was poor correlation between DC and PDD. However, PDD was acknowledged as an acceptable alternative method of plasma volume measurement because of its repeatable measurement of a 10-15% plasma volume decrease, which matched results of previous studies. The authors also claimed that PDD was superior to DC because of its ability to determine CBV in only a few minutes. Also, no reports of poor signal quality while PDD was performed were presented.

The non-invasive measurement of CBV in infants is another application of PDD [48]. CBV is an important variable in infant monitoring while in intensive care. However, there are few reports of accurate methods to measure CBV in infants. In one study, PDD was used to determine CBV in 13 infants. Its accuracy was determined by comparison to a CBV determined by a fetal hemoglobin dilution method. The bias between the two methods was low with acceptable precision suggesting good agreement between the two methods. The reproducibility was assessed by repeating the PDD measurement in each infant. Comparison of the first and second CBV measurements by

PDD showed poor reproducibility. The authors concluded that PDD was a feasible method to determine CBV in infants using a bedside measurement, but also claimed that its use was limited due to poor reproducibility.

Liver function can be assessed using PDD by examination of the ICG clearance curve. The liver is the main organ responsible for the removal of ICG from the circulation. Therefore, the removal rate of ICG can be used as a diagnostic indicator of hepatic function. The accuracy of the measurement of ICG plasma disappearance rate (PDR) by non-invasive transcutaneous PDD was confirmed when compared to invasive arterial measurement with a fiber optic probe [49]. This technique had been previously validated by comparison to a photometric method. The PDR measurements using PDD showed excellent agreement compared to the invasive arterial fiber-optic method, validating PDD as a method to measure PDR of ICG. One study showed a decreased removal rate in patients who underwent liver resection [50]. Decreased removal rate was seen in all patients after surgery as compared to removal rate before surgery. The residual liver volume was calculated using computed tomography (CT), and was then used to estimate the post operative hepatic clearance rate. The clearance rate measured using PDD was compared to the estimated clearance rate using CT and showed good correlation. There was also a significant difference in the post-operative clearance rate in patients presenting prolonged jaundice as compared to those who did not. The parameter ICG-R15, which is the ICG retention after 15 minutes post-injection, has also been used as an indicator of post- hepatectomy liver function [51]. PDD has also been evaluated as a prognostic indicator in patients with acute liver failure (ALF). In one study [52], the ICG removal rate of patients who later underwent spontaneous recovery was significantly

higher than in patients who did not, highlighting PDD's ability to identify ALF patients in need of urgent intervention. The feasibility of using ICG clearance as a predictor of liver failure after cardiac surgery in patients with preoperative liver dysfunction was also studied [53]. ICG clearance rate by PDD was determined in 27 patients prior to surgery. 6 of these patients died after surgery. The authors noted that the mean ICG-R15 during PDD measurement in these 6 patients was much higher than the other 21. Basic determination of hepatic function has also been demonstrated using the ICG clearance curve in one and two parameter mathematical models [54]. The one parameter model described the first order kinetics of the exchange of ICG between the blood and the liver characterized by the clearance rate, k. The two parameter model included both the exchange between blood and liver and also liver and bile. The two parameter model proved to be superior by determining several important diagnostic parameters capable of distinguishing between types of liver pathologies with 95% confidence.

2.5 Limitations of PPG Collection and Analysis

Attempts have been made to modify the theory of light transport through dense scattering biological media. The absorption coefficients of both HbR and HbO_2 are well documented [31]. However, the scattering properties of blood must be measured *ex vivo* and are dependent on variables such as oxygenation, hematocrit, and flow rate, and erythrocyte orientation [55]. Therefore, careful and precise measurements are needed. Several groups have reported values for absorption and scattering coefficients of whole blood, and also its anisotropy [56-59]. However, many of these values are conflicting or describe these variables under very particular circumstances or for only particular wavelengths associated with commonly used lasers.

The measurement of arterial pulsation can often be confounded by noise and interference. The most common confounder is motion artifact [60]. Changes in the extinction of light due to pulsation are very small and therefore require a probe that is securely attached to the anatomical location measured. Small shifts in the probe placement or anatomy will cause changes in the optical path length and will correspond to signal changes often much higher in magnitude than those due to arterial pulsation. One common result of improper probe placement is optical shunting. This occurs when light emitted by the sources does not pass through the vascular bed, but still reaches the detector. Respiratory artifact can also interfere with PPG. This will often cause a repetitive baseline drift making the measurement of the change in extinction from arterial pulsation difficult. Motion artifact can also arise from other normal physiological movements such as shivering and coughing. The most common result from motion artifact is that the signal for all wavelengths used by the device is affected. This is particularly problematic in pulse oximetry because this will cause erroneous measurement of SpO_2, regardless of whether the true oxygen saturation is normal or dangerously low.

Arterial pulse amplitude is often a variable in PPG. In patients with poor circulation it is often difficult to accurately measure a pulsatile signal because of its low magnitude. This degrades the signal-to-noise ratio and makes pulse detection difficult. Conditions such as hypovolemia, hypotension, hypothermia, and peripheral vascular disease can cause poor circulation resulting in poor signal strength at the probing location [60]. This is particularly problematic because accurate physiological monitoring is crucial to patients with these conditions. In general, vasoconstriction can affect PPG

measurements. This was shown in a study where vasoconstriction and vasodilation were induced and PPG measurements were taken at constant temperature [61].

Red and near-infrared absorbing dyes can interfere with spectral analysis of arterial blood since they influence the transmission of wavelengths often used in pulse oximetry [60]. This can cause errors in the SpO_2 measurement, making the apparent oxygen saturation appear lower than the actual saturation and can often complicate co-oximetry which will often report increased methemoglobin levels when certain dyes are present. Reports of patients displaying apparent moderate to severe hypoxemia as measured by pulse oximetry after the injection of dyes such as isosulfane blue, patent blue V, methylene blue, ICG, and indigo carmine (IDG) have been published in journal articles and case reports [62-65]. Quantitative effects dependant on the amount of dye administered [66] and time after injection [67] have also been reported. Blood gas analysis, which is insensitive to these dyes and can measure the partial pressures of blood gases, has been used to refute these false readings [68-71]. The purpose of injecting these exogenous dyes is to map the lymphatic vessels near resected tumors. The dyes are injected near the primary tumor site and allowed to collect in the local lymphatic vessels. This causes proximal lymph nodes, often referred to as sentinel nodes, to become stained making them identifiable by visual inspection. These are possible routes for metastases and often warrant biopsy. After injection, dye may also collect in the blood stream and cause a shift in the spectrum of whole arterial blood. This increases the optical density of the blood at the wavelengths most sensitive to HbR causing an artificial apparent reduction in SpO_2. The patients in these reports did not show other signs of hypoxia and their SpO_2 would return to normal after clearance of the dye from the blood stream.

In PDD, the loss of signal strength or an erratic signal can be detrimental to the measurement of circulating dye rendering the procedure useless. This can be caused by dislodgement of the probe or by physiological factors reducing pulse amplitude [72]. A study conducted on patients undergoing elective coronary artery bypass grafting reported that agreement between PDD and thermodilution was poor and that the error was dependant on the volume of the bolus injection of ICG [73]. Thermodilution is a clinically accepted technique for estimating CO by measuring the downstream change in temperature in the pulmonary artery when either warm or cold saline is injected into the right atrium and using the thermodynamic properties of blood [29]. The pulse dye densitometer used in this study was the DDG-2001 by the Nihon-Khoden Corporation which used wavelengths of 805 and 940 nm. The 805 nm source was standard for measuring ICG, and the 940 nm source was used to determine the contribution of hemoglobin. Blood gas analysis was performed before the PDD measurements in order to determine hemoglobin concentration and blood oxygenation, which were used in the determination of ICG concentration by PDD. The study was originally designed to assess the use of PDD in patients under anesthesia before and after cardiac surgery. However, there were problems in collecting an acceptable pulsatile signal, both before and after surgery. The pulsatile signal obtained from the fore finger was only considered acceptable if it comprised greater than 1% of the total signal. The study used 28 patients, each scheduled to undergo cardiac output measurements before and after surgery. Before surgery, an acceptable signal could not be obtained from one of the patients so they were excluded. Four more patients were excluded after ICG injection because of weak pulsatile signals. After surgery, acceptable signals could not be obtained from more than

half the patients. Therefore, the study only analyzed cardiac output as measured by PDD before surgery. This may have been a combined effect of patient recovery after cardiac surgery and age since the mean patient age was 63 years. PDD was performed twice in each patient that showed acceptable pulse strength, one using a 5 mg bolus and one using a 20 mg bolus. The authors reported that CO measured by PDD showed poor agreement with thermodilution. They also claimed that the errors in PDD measurements were dependant on the bolus size. Bolus injections of 5 mg tended to underestimate CO while the 20 mg bolus injections tended to overestimate CO. Therefore, the authors determined that PDD did not perform well enough to be considered clinically useful.

Signal strength and quality can also be an issue when monitoring the newborn. In determining CBV using PDD in infants, it was noted that several cases of probe dislodgement caused exclusion of data from that particular subject [48]. This was probably due to the physical size of the probing volume, since the probe was placed on either the finger or toe. To correct this problem, the authors suggested that a specially made probe for infants be used instead of the conventional probe for adults. The authors also reported that one measurement had to be excluded because of ICG injection error. This is problematic since PDD requires venous dye injection and it can be difficult to cannulate a blood vessel in small infants.

The presence of abnormal forms of hemoglobin can also affect PPG measurements, especially in the spectral analysis of blood [60]. Several variants of hemoglobin are present in blood. The majority of the hemoglobin present in blood is either reduced or oxygenated. Some of these variants do not facilitate the transport of oxygen in the blood and are termed dyshemoglobins. These compounds have spectral

properties different than HbR and HbO_2. Two of these variants that can often confound spectral analysis are carboxyhemoglobin (HbCO) and methemoglobin (HbMet). HbCO is formed when hemoglobin binds to carbon monoxide and can be present in high levels in smokers or in patients with carbon monoxide poisoning. The spectrum of HbCO is similar to that of HbR in that it absorbs red light preferentially over infrared light. HbMet is a form of hemoglobin that results as the iron in hemoglobin becomes oxidized to form its ferric state. The formation of HbMet is often the result of exposure to anesthetics, sulfa drugs, and nitrites. HbMet has an absorption spectrum having higher absorption at 940 nm than both HbO_2 and HbR and high absorption at 660 nm. In normal healthy blood, the percentage of hemoglobin in these forms is small, making their effects on the extinction spectrum of blood negligible. However, in cases where HbCO is present in high levels, the SpO_2 measured by pulse oximetry can either over or underestimate the true blood oxygenation depending on the wavelengths used by the instrument. One case report reported that CO poisoning caused an apparent reduction in SpO_2. While under anesthesia, an unexplained reduction of SpO_2 was noticed in a 2 year old patient. Since CO poisoning was suspected, analysis of an arterial blood sample was performed and confirmed CO poisoning, not hypoxemia. Other sources reported that high levels of HbCO caused overestimation of SpO_2. This is a much more dangerous circumstance since overestimation of SpO_2 will not necessarily warrant intervention during potential CO poisoning. High levels of HbMet will cause the measurement of the red to infrared ratio to approach one because of its contribution to both wavelengths. This results in apparent hypoxemia (80-85% O_2 saturation) by SpO_2 measurement in conventional pulse oximetry.

One other form of dysfunctional hemoglobin is sulfhemoglobin (HbS), which results from the reaction of hemoglobin and hydrogen sulfide. This reaction is not well understood, but often can be the result of long term prescription drug use. One case report reported sulfhemoglobinemia in a patient who had been prescribed the drug metoclopramide and had been using it for over a year [74]. This resulted in SpO_2 measurement of 85% by pulse oximetry prior to surgery. Blood gas analysis by spectrophotometry reported a sulfhemoglobin concentration of 28%. The absorption spectrum of HbS shows much higher absorbance at 660 nm than at 940 nm [75], which explained the apparent low SpO_2.

The pulse oximeter is one of the rare biomedical instruments that currently cannot be calibrated *ex vivo* [76]. This is because the behavior of light in tissue is not well enough understood to produce an accurate model to use as a calibrator. Therefore, calibration of commercial pulse oximeters is done using patient data concurrent with blood gas analysis or co-oximetry. This requires that large sets of data be taken on multiple patients every time a pulse oximeter is calibrated. It also requires that the oxygen saturation in people be modulated in order to produce a calibration curve that can only go as low as about 70%. The dynamic range of the instrument is therefore limited and its accuracy can only be as good as that of the calibration curve.

2.6 Novel Improvements in PPG

A short paper was published in 2002 addressing the theoretical calculations related to PPG [77]. The paper described the contribution of scattering to the attenuation of light in turbid media such as blood. It also addressed the fact that in analyzing the pulsatile signal in PPG, some of the contribution may be from tissue as well as arterial

blood. Schuster's Theory and Beer's law were employed in order to produce equations that could be used to calculate SpO_2 and also proposed that the effects of tissue were wavelength dependant and could vary over time. Aoyagi and other groups began to modify their PPG instruments to contain more wavelengths allowing for more thorough spectral PPG measurements.

A more recent report expanded this theory to using five wavelengths [78]. The influence of venous blood was added to the equations. The report also explained that tissue constants were empirically determined and when coupled with averaging could be effectively used to minimize the effects of motion artifact on SpO_2 determination. A similar device capable of measuring several cardiovascular variables was reported [79]. It also made use of novel application of optical and electrical instrumentation made possible by recent advances in miniaturization of these components. This device used a combination of five wavelengths, four of which were situated in the tissue optical window between 600 and 1100 nm. The fifth was an infrared wavelength, which is sensitive to water and could aid in the monitoring of tissue and blood water content. Each wavelength was provided by a laser diode coupled to a fiber optic delivery probe designed to fit on the finger. The probe also contained two photodetectors, one silicon photodetector for the visible and NIR sources and one InGaAs detector for the infrared source. The ability to monitor oxygen saturation in good agreement with co-oximetry was demonstrated. Semi-quantitative analysis of PPG signals obtained during ICG bolus injection and dialysis demonstrated the device's spectral specificity.

PDD systems using three wavelengths have also been recently reported. In one report, an 805 nm source was used to detect the concentration of ICG [80]. Two other

light sources (660 nm and 940 nm) were also used. By using these extra wavelengths, more information about the tissue could be obtained. Therefore, the effects of tissue pulsation could be accounted for concurrent to vascular ICG measurement. The study also examined the use of both a transmission and a reflectance probe. The main advantage to using a reflectance probe is that it can be attached to any part of the body. This expanded the realm of possible probe locations beyond the digits, ear lobe, and nose and permitted monitoring closer to the core of the body. The study was designed to simulate cardiovascular monitoring in small infants and therefore piglets were used. The transmission probe was placed in the tail to simulate peripheral circulation monitoring and the reflectance probe was placed on the ear. Comparisons of CO measurements taken at each probe location were made with ultrasound flowmetry. Both locations showed good agreement with ultrasound, and smaller bias was seen using the reflection measurements. Another report of 3 wavelength PDD was reported using IDG [81]. The wavelengths used were 620 nm, 730 nm, and 870 nm. The 620 nm source was chosen to match the extinction peak of IDG, while the 730 nm source was chosen to estimate the effect of the pulsatile tissue over time. The system was tested on mongrel dogs during hypovolemia, hypervolemia, and normovolemia induced with blood transfusion in order to test CBV calculation accuracy. The results were compared with a CBV calculation using radiolabeled red blood cells, but did not show good agreement. However, CO measurements using this dye in PDD showed good agreement with a thermodilution technique.

Development of different probe geometries has been proposed as a way to optimize light detection in PPG. A recently published paper reported a wireless

reflection pulse oximeter with novel ring detector geometry [82]. Reflection PPG is often

subject to low AC signal amplitude and low signal to noise ratio because the components

of biological tissue are primarily forward scattering. This means that much of the light

emitted from the sources diffuses further into the tissue and does not reach the detector.

A ring detector around the light sources enhances the detection of backscattered light by

increasing the effective detector area. The LED's and photodiode were both patterned on

a silicon chip where the detector area was comprised of a ring around the two sources.

A similar detector geometry was used in the Cybro Medical IM2001 prototype, which

was tested at various locations on the body to access optimal placement [83]. This

prototype used two concentric detector rings situated around a three wavelength source

and was encased in an optically opaque probe compatible with many probing locations on

the body. This is advantageous for clinical monitoring because many times patients

undergoing surgery display poor pulse amplitude in peripheral locations like the fingers

and toes. It is also useful in the monitoring of infants because monitoring at the

extremities can be difficult due to their small size. The probe was tested at three

locations, the chest, forehead, and back. The prototype was tested during gradual

desaturation and resaturation of blood in human subjects. It showed excellent correlation,

low bias, and high precision when compared with blood gas analysis by co-oximetry.

The best performance was demonstrated on the back, but analysis showed good

performance regardless of probe location. The potential for an implantable pulse

oximeter has also been reported [84]. A probe was fabricated on a silicon ring which

could fit around a blood vessel. The device was subjected to *in vitro* testing using a mock

circulatory system and showed excellent pulse amplitude improvement when compared to finger measurement because of its proximity to the pulsatile blood in an artery. Another PPG geometry was explored in the development of a pulse oximeter glove using photonic textiles [85]. This geometry was proposed to improve the comfort of PPG measurement probes and to provide better coupling of light to the tissue resulting in diminished motion artifact. These fabrics consisted of polyester fibers either inter woven or embroidered with small diameter plastic optical fibers, which acted as both light emitters and detectors. The fibers would emit and collect light at the fingertip of the glove. Several fiber modifications such as core roughening, application of aluminum reflectors, and 90° bending were used to increase the efficiency of light delivery and detection. The glove could be worn and provided good coupling of the fibers to the skin. Signal to noise ratio was accessed using two oximetry wavelengths. The 90° bending of the fiber tips produced the best pulsatile signals with the smallest standard deviation in SpO_2 measurement.

Another approach to improving the application of PPG to pulse oximetry was to improve determination of SpO_2 by employing novel signal processing algorithms. The Masimo Corporation developed a novel algorithm designed to negate motion artifact [86]. The algorithm separated the arterial pulsation signal from the venous pulsatile signal due to motion by an iterative process of guessing values of optical density ratios between the red and infrared signals. By sweeping through these values, a reference signal could be produced. The frequencies of the infrared signal correlated with the reference signal were then subtracted via adaptive filtering. When the optical density ratio of the venous blood corresponding to motion was guessed, this would result in the

production of a reference signal that correlated with the arterial frequencies in the infrared signal. Therefore, at this value, the signal due to the arterial pulsation was subtracted, revealing the frequencies associated with the motion. The opposite was true when an optical density ratio corresponding to the arterial pulse was guessed. In this situation, the reference signal would contain the frequencies associated with the infrared motion signal and therefore it would be subtracted revealing the arterial signal. After sweeping through every optical density ratio associated with SpO_2 values between 0% and 100%, a power spectrum with respect to SpO_2, termed the discrete saturation transform (DST), was produced revealing peaks at the SpO_2 values associated with venous and arterial saturation. The venous saturation was considered the signal from motion, while the arterial signal would appear at the SpO_2 associated with the arterial pulse and was therefore deemed the true signal. A similar process was used to determine pulse rate as well. This algorithm was shown to be effective in separating motion and arterial pulsation upon the onset of motion mimicking the motion of venous blood. DST's resulting from motion would show a peak at associated SpO_2 values of 70-80%, which is close to the typical saturation value of venous blood. The spectrum would also show a peak between 95-100%, which was a typical value for arterial saturation while breathing ambient air.

The Masimo Corporation has also made advances in PPG in the production of their Rainbow SET oximeters which uses multiple wavelengths. As mentioned previously, dyshemoglobins can confound the spectral measurement of arterial blood because of their abnormal absorption spectra. These new oximeters are able to account for the presence of dyshemoglobins and report their concentrations, total hemoglobin

concentration, and SpO_2. One study investigated the accuracy of the Masimo Rainbow SET Rad-57 oximeter in determining the degree of artificially induced carboxyhemoglobinemia and metheloglobinema [87]. The device showed excellent performance as assessed by Bland- Altman analysis showing very low bias and good precision when compared to standard co-oximetry *ex vivo* analysis of arterial blood. This was a significant advance in oximeter technology since these dyshemoglobinemias can be harmful or life threatening if gone undiagnosed.

To circumvent the problem of the absence of a detectible pulse often observed in patients with conditions such as meningococcemia and diabetes mellitus, one group reported the use of a four wavelength oximeter coupled with an artificial pulse generator [88]. The pulse generator was a pneumatic cuff that could be attached to the finger and would use a peristaltic action to artificially pulse both venous and arterial blood into the vascular bed of the fingertip. PPG measurement at four wavelengths was used in conjunction with theoretical photon diffusion modeling and empirical calibration to estimate both arterial and venous oxygen saturation. *In vitro* calibration was performed using a three chamber cuvette that could pulsate with the application of pressure. In general, empirical calculations performed better than theoretical, but *in vivo* testing revealed significant bias between venous and arterial saturation and the same measurement using co-oximetry. However, the device demonstrated that it was possible to induce artificial PPG signals using a pressure cuff and showed promise in its ability to determine both arterial and venous saturation, two very significant parameters in determining tissue viability in patients with conditions affecting peripheral blood flow.

A pulse oximeter simulator capable of interfacing with any commercial pulse oximeter providing a means for standardized calibration has been reported [89-91]. Since it is difficult to develop a phantom that accurately simulates tissue optical properties, the device instead was comprised of an artificial finger that could connect to any pulse oximeter and would simulate the transmission of light in tissue. The finger contained two waveguides separated by optical shielding. One was used to collect the light emitted by the pulse oximeter and another to deliver light to the detector. The detector waveguide would collect the spectra of the light emitted by the pulse oximeter and then feed this data into a calibration module that used a spectrometer to determine the wavelengths of the LED's and time resolved spectral data from patients used to determine the intensity of the light that would result from its passing through a real finger at a given oxygen saturation. The modulation signals from the pulse oximeter LED's were then used to trigger the emission of light from the calibrator at the computed intensity. This was then delivered to the photodetector in the pulse oximeter by the second waveguide. The pulse oximeter would then determine SpO_2 and could be compared to the simulated oxygen saturation. Five commercial pulse oximeters were tested in this study each showing good correlation with the simulated oxygen saturation. The errors between measured SpO_2 and actual oxygen saturation were comparable to those encountered using *in vivo* calibration. Thus a promising new standardization technique for pulse oximeters had been demonstrated.

Modeling of blood pulsation in tissue has been performed to attempt to account for variables like pulse depth, probe placement, and source detector distance in reflectance pulse oximetry [92]. This is of particular interest because fetal SpO_2 is assessed using a reflectance probe. Also, it has been observed that measurements of

oxygen saturation can vary from site to site on the same subject. For example, when the probe is placed near a palpable artery like the femoral or carotid, an underestimation of oxygen saturation is often measured. A multi-layer Monte Carlo simulation was performed to simulate the theoretical light detection of reflectance probes under varying conditions in order to predict variations in signal collection seen *in vivo*. The layers used in the model were the appropriate perfused and non-perfused tissues ranging from the superficial epidermis to the deeper hypodermis. Each layer was modeled by its optical properties and by physiological variables like thickness and blood fraction. Pulsation was simulated by small increases in blood fraction and pulse depth was simulated by moving higher blood fractions to deeper or shallower layers of the tissue model. The model was used to predict light detection at two wavelengths often used in fetal pulse oximetry, 660 and 890 nm, in several situations. Pulse amplitude ratios at the two wavelengths from both deep and shallow pulsations at different distances between the source and detector were calculated. This revealed an optimal distance where SpO_2 errors were minimal. An exaggerated blood fraction was used to model the probe placement over an artery and predicted slight underestimation by SpO_2 measurement at high oxygen saturation, and significant overestimation at low oxygen saturation. This was confirmed in an *in vivo* site by site analysis study using piglets as infant models. Overall, utility of the model was confirmed by comparison with the *in vivo* experiments and proved that it was useful in determining optimal reflectance probe design and placement when monitoring infants.

Contactless collection of the PPG has been reported using a CMOS camera with a multi-wavelength ringlight [93]. Its application was the non-invasive measurement of

SpO_2 by development of a 2-D oxygen saturation map of the imaged tissue. By the rapid collection of images at three wavelengths, the feasibility of imaging this 2-D SpO_2 map was demonstrated. Many images of the tissue were taken over time and averaging was performed on 10 x 10 pixel regions of interest. The variation in the detected intensity at each wavelength could be determined at each location in the image. The frequencies in this variation corresponded to the respiratory rate and to the heart rate, which was confirmed by synchronous monitoring of breath rate and heart rate by pulse oximetry and EKG. The time varying signals at each pixel were filtered and then transformed to the frequency domain in order to separate the heart rate from the background signal. Each pixel was then assigned a relative spectral power at the frequency corresponding to the pulse amplitude. Superficial blood vessels could be identified in the image by increased spectral power at the frequency of the heart beat, thus validating the feasibility of the development of a SpO_2 camera by contactless multi-wavelength PPG measurement.

2.7 Application to Nanoparticle Therapy

PPG has been employed in a wide variety of biomedical applications. The spectral analysis of tissue and pulse wave analysis have been proven increasingly effective and versatile by the novel improvements of signal collection and analysis. These improvements include the incorporation of multiple wavelengths, improvement in opto-electric instrumentation and probe geometry, improved signal processing, and greater understanding of tissue optics. The *in vivo* spectral analysis if arterial blood has only recently been used in the management nanoparticle therapies [94], many of which employ the use of strongly NIR extinguishing nanoparticles that resemble optical dyes used in PDD. It has been shown that the attenuation of light do to the intravenous

injection of these nanoparticles can be detected using modern optical instrumentation [95,28]. Because of the increased use of optically active nanoparticles in the treatment of cancer, the use of PPG in monitoring nanoparticle treatments shows exciting promise. The work presented in this dissertation describes the application of multi-wavelength PPG to vascular optical nanoparticle monitoring. The development and testing of an optical pulse photometer is presented in chapters 3, 4, and 5. Three design prototypes are presented which are termed prototypes I, II, and III. Prototype I is also referred to as a photometer because the initial tests of this prototype were performed to assess its ability to detect optical density changes in the bulk tissue. Prototypes II and III are given the term pulse photometer because they were designed to examine the optical characteristics of pulsating arterial blood. Each successive prototype displays significant improvements in instrumentation and/or signal processing. These characteristics include measurement type, optoelectronics, number of data channels, ambient light correction, probe location, system output, and weather the probe can be removed and replaced on the subject. The specifications of each prototype are given in Table 1.

Table 1. Specifications of each prototype optical device

Proto type	Meas. type	Source	Photo Diode	λ	Data Channels	Amb. Light Sub.	Probe	Output	Remove
I	Total extinction change, Pulsatile extinction change	Roithner LaserTechnik LED660/940-04A or LED760/940-04A	Hamamatsu S1337-33BR	660/940 nm or 760/940 nm	2	No	Tail, Thorax, Leg	AC/DC mag (volts)	No
II	Pulsatile extinction change	Marubeni L660/735/805/940-40B42	Hamamatsu S1337-33BR (foot/tail) Hamamatsu S6931 (leg)	805/940 nm	8	Yes	Tail, Leg, Foot	R (no units)	Yes
III	Pulsatile extinction change	Marubeni L660/735/805/940-40B42	Hamamatsu S1337-33BR (foot/tail) Hamamatsu S6931 (leg)	660/805/940 nm	8	Yes	Tail, Leg, Foot	Arterial optical density (OD), Arterial SpO₂ (%)	Yes

The prototypes were each tested on murine subjects in order to verify their specified operation. Therefore, all animals were handled and cared for in accordance with the Louisiana Tech Institutional Animal Care and Use Committee (see APPENDIX F). A detailed explanation of the interaction of light with optically absorbing media, a subject applicable to the development of each prototype device, can be seen in APPENDIX A and APPENDIX B. Instrumentation diagrams and pictures of the final design iteration of the pulse photometer can be seen in APPENDIX C.

A spectrophotometric technique using small volume micro-cuvettes (100-200 µL) to analyze small volume blood samples (5 µL) drawn from injected animals will also be presented and verified. The technique is possible due to the precise optics in the spectrophotometer used to process the samples. It uses a small focused beam to interrogate samples and is capable to measuring up to approximately 3 absorption units

(AU) with a sensitivity of 0.02 AU. This makes it possible to detect the vascular optical

density of the nanoparticles in the blood samples drawn from the injected animals used in

several of the experiments. The spectrophotometric technique was verified using a

technique, instrumental nuclear activation analysis (INNA), which has been proven

effective in detecting small amounts of gold resulting from the intravenous injection of

gold nanoshells. The data from this experiment is presented in 3.5. Each set of animal

experiments with the results and conclusions will be presented in their respective

sections. Individual animal data from each formal experiment can be seen in APPENDIX

D.

CHAPTER 3

DESIGN AND DEVELOPMENT OF

PROTOTYPE PHOTOMETER I

3.1 Instrumentation

A prototype two-wavelength photometer was developed in order to establish the feasibility of detecting the addition of optically extinguishing dyes/nanoparticles to the vasculature of a murine model. The specifications of the device were as follows:

- Capable of emitting and detecting two wavelengths using one photodetector.

- Capable of detecting the change in optical extinction of the bulk vasculature (arterial and venous) upon addition of dyes/nanoparticles.

- Compatible with the murine anatomy.

- Capable of detecting the constant (DC) and pulsatile (AC) portions of transmitted light through a murine subject.

This photometer consists of the analog circuitry to control the emission of each wavelength and separate the signals from each wavelength on two channels, and the LabVIEW user interface and signal processing modules. The circuitry in the photometer is composed of inexpensive integrated circuits and opto-electronics. A timer chip (NE555P) is used to produce a series of pulses that control the emission of light at two wavelengths. The chip controls two comparators (LM324N) that supply current to a dual wavelength light emitting diode (LED) that emits at 660 nm and 940 nm (LED660/940-

04A Roithner LaserTechnik), which is enclosed in a clip designed to fit around a mouse's

tail. The clip also contains a photodiode (S1337-33BR Hamamatsu) that is configured in

photovoltaic mode. The spectra of the LED's in this clip can be seen in Figure 4.
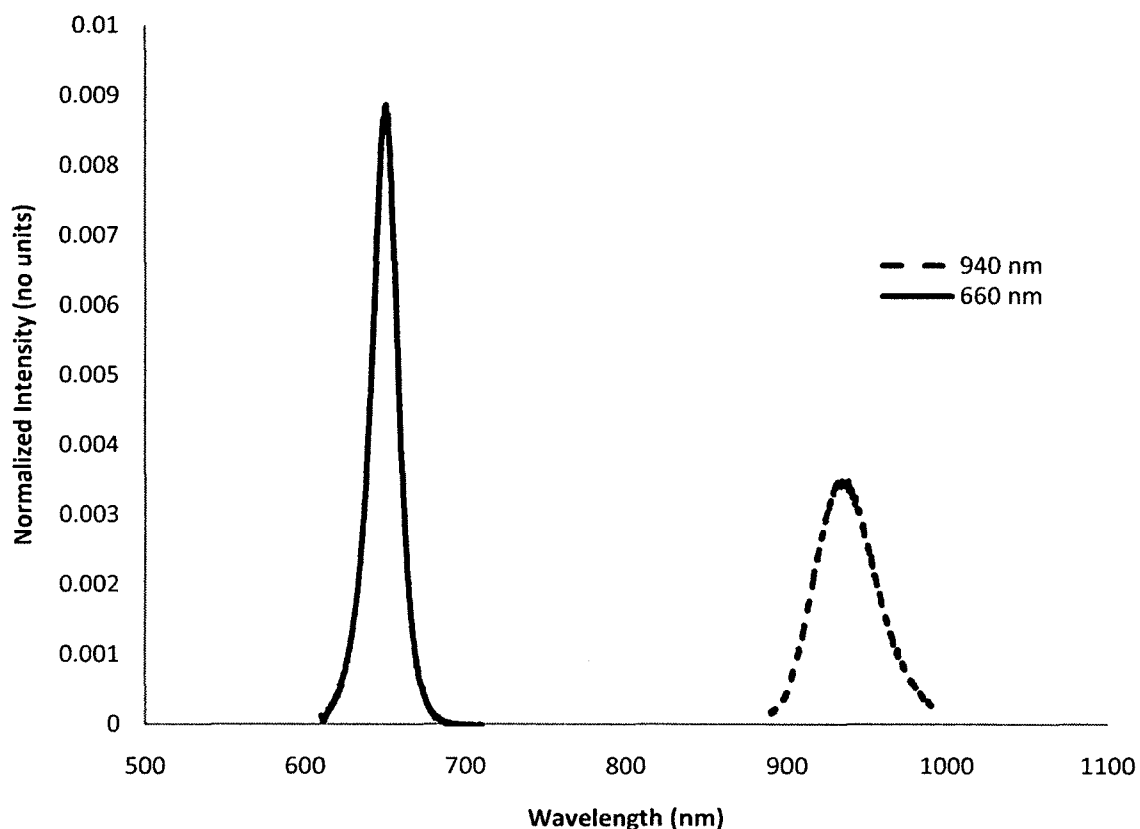
Figure 4. Spectra of the LED's used in the prototype I tail clip

The photodiode is connected to an operational amplifier configured as a current to

voltage converter (OPA37GP) with a gain of 2.7 MV/A. It is positioned so that the

device acts in transmission mode. The signals from the photodiode are sent via a

shielded coaxial cable to two sample-and-hold chips (LF398N) that are synchronized

with the alternating emission of each LED to temporally separate the signal of the two

LEDs into two channels using a single detector. A 5 V DC regulator (ML7805A

RadioShack) was attached to the positive power supply and was shorted to ground

through a 33 nF ceramic capacitor to eliminate inherent high frequency noise. This

served as the logical reference for the sample-and-hold chips. The signals from each

sample-and-hold circuit are then passed through analog low pass filters (f_c = 8.4 Hz) and

detected on two channels by a National Instruments analog to digital converter board (NI

USB 6009) operating at a sampling rate of 10kS/sec. The signals are processed in

LabVIEW in real-time. A schematic of this instrument can be seen in Figure 5.
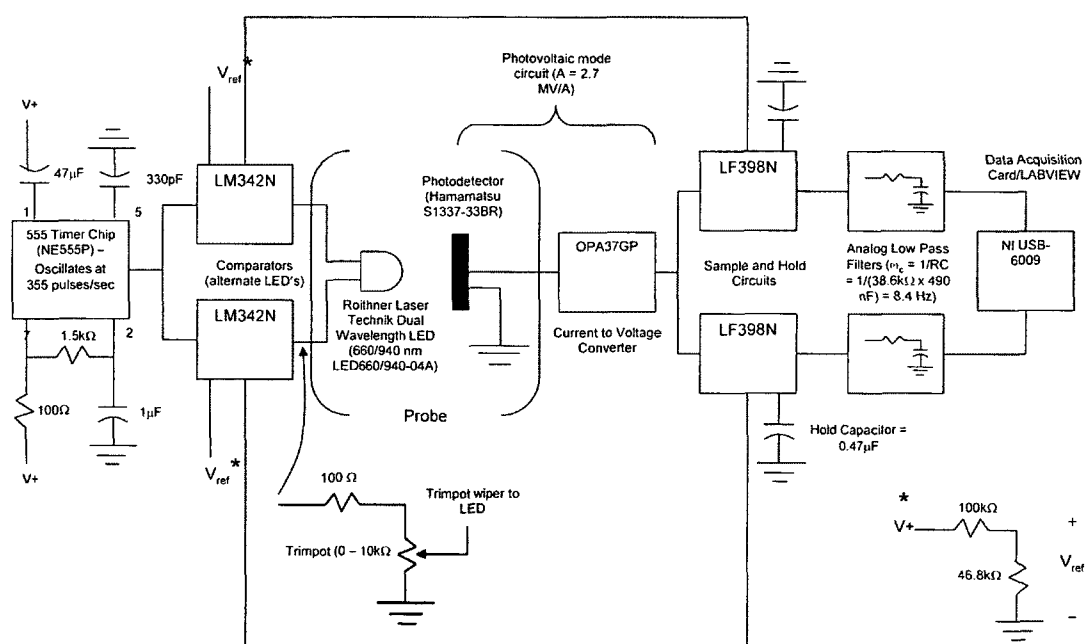
Figure 5. Block diagram of the prototype two-wavelength photometer.

3.2 Pilot Study Demonstrating Optical Tracking

For this first pilot study, the ability of the photometer to detect the increased *in*

vivo attenuation of light at 660 nm due to injection of both an optically absorbing dye and

dye loaded nanoparticle. The dye chosen was NIR 664 (Sigma Aldrich) which has an

absorption maximum at approximately 664 nm. The nanoparticles chosen were 200 nm

diameter FluoSpheres (Molecular Probes) which are polystyrene nanoparticles loaded

with another red absorbing dye with an absorption maximum at 660 nm. The dye was

prepared at 0.4 mg/ml which corresponds to 66 OD at 660 nm in 10% DMSO/90% PBS

solution. FluoSpheres were first modified with a layer of poly(allylamine) hydrochloric

acid (PAH). They were then centrifuged and washed with DI water. 5kD

Methoxypolyethylene glycol succinate N-hydroxysuccinimide (PEG) (Sigma Aldrich)

was then conjugated to the surface of the FluoSpheres via amine binding. The excess

PEG was used as the excipient for injection. Dynamic light scattering and zeta potential

analysis confirmed the stability, small size change, and charge of the particles after each

modification (Figure 6). Based on the specified percent solids, size, and the extinction

spectra of the nanoparticles, their concentration before and after injection was determined

to be 3.14×10^{12} and 2.5×10^{12} particles/ml respectively (Figure 7).
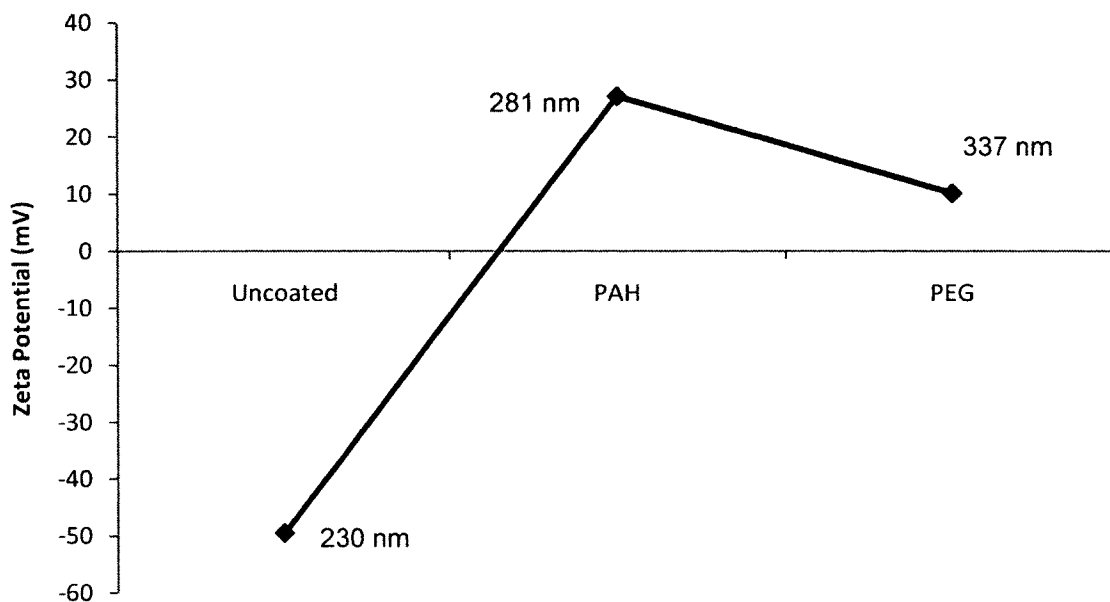
Figure 6. Zeta potential and size measured using DLS before and after FluoSphere coating. The charge inversion shows the attachment of PAH in the first coating step, and the reduction in positive charge confirms attachment of PEG.
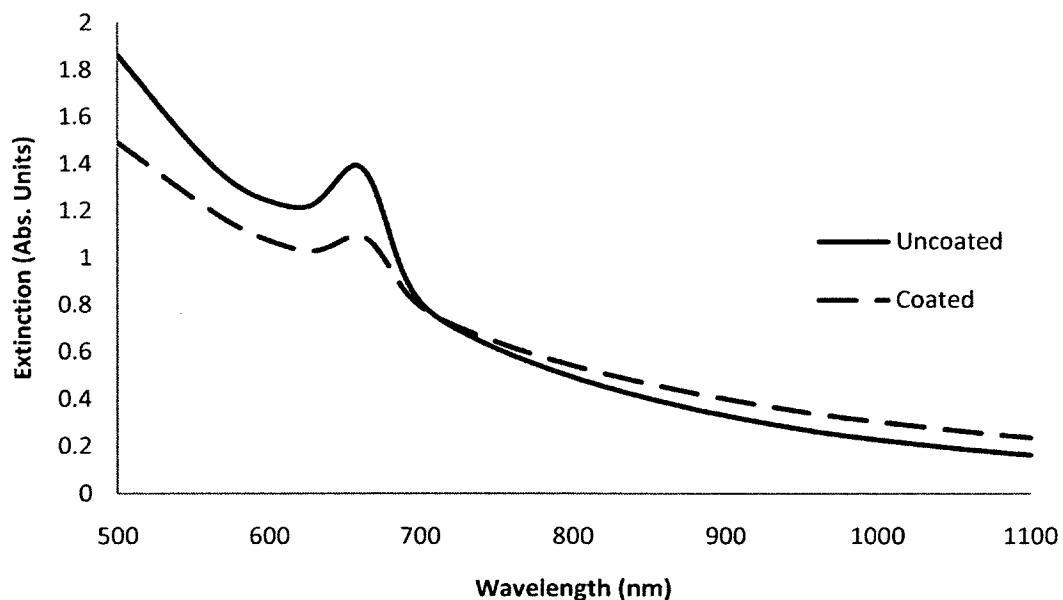
Figure 7. Extinction spectra of coated and uncoated FluoSpheres. The slight reduction in extinction at 660 nm was used to determine the concentration of nanoparticles in the final batch.

Two female BALB/c mice (18-20g) mice were used in this pilot study. The first

was anesthetized using a ketamine (10mg/ml) and xylazine (1mg/ml) mixture at a dose of

0.1ml/10g for immobilization. It was then placed on a heating pad to maintain normal

core temperature (37 °C). Catheters were prepared using 2 french polyurethane catheter

tubing (Access Technologies) and a 29 gauge needle from an insulin syringe (Becton

Dickinson). The catheter was inserted to the tail vein and secured. The photometer was

placed on the tail of the first mouse and three identical 70 μL injections of NIR 664 were

given. The dye was allowed to clear between injections and was observed by voltage

changes on the 660 nm channel read by the data acquisition card (Figure 8).
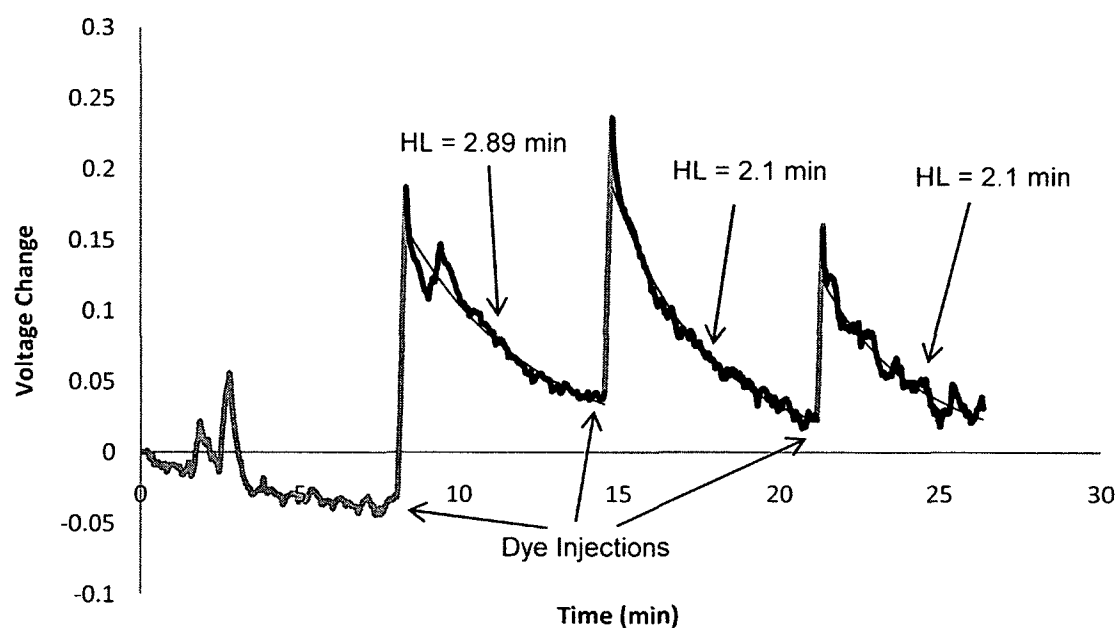
Figure 8. Dye clearance curves after repeat NIR 664 injections.

Circulation half lives were determined by fitting a single exponential model to the

data after each injection. Repeated injections of dye showed half lives consistently

between 2 and 3 minutes, which is comparable to the typical half life of ICG.

The photometer was then used on the second animal to monitor the circulation of injected FluoSpheres. The same anesthesia protocol was followed. A 100 µL injection of PEG modified FluoSpheres was delivered and the change in the voltage on the 660 nm channel was observed for approximately 60 minutes (Figure 9).
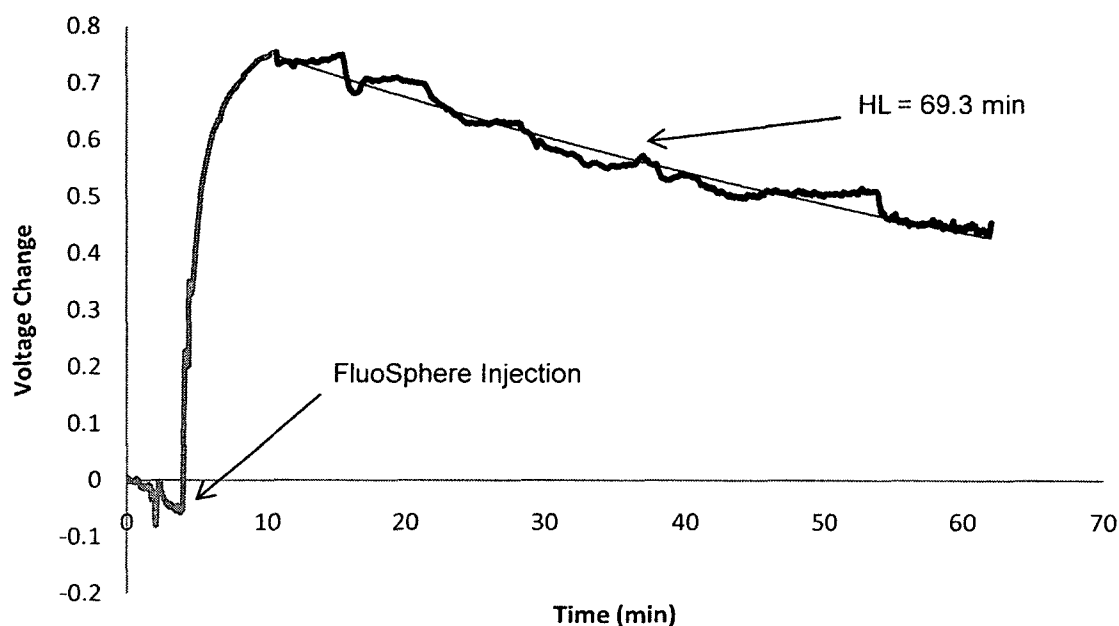
Figure 9. Voltage change measured after the injection of PEG modified FluoSpheres.

Again, a single exponential decay was used to determine the circulation half life of the particles. A dramatically increased circulation half life of 69.3 minutes was measured.

The results of this initial study were semi-quantitative, demonstrating the ability to monitor both short and long circulating optically absorbing species. Thus, the feasibility of this technique was established.

3.3 Formal Testing of the Prototype I Photometer

In the pilot experiments, the photometer was used to measure the change in the total extinction of light in murine subjects due to intravenous dye/nanoparticle injection. It was shown that changes in the transmitted intensity of light could be used to estimate the concentration of a circulating optically extinguishing species. The first formal experiment was conducted to test the feasibility of using the photometer to determine the concentration of intravenously injected gold nanoshells. No changes were necessary to the circuitry or LabVIEW interface of the photometer to conduct this study. However, two changes were made to the probe of the photometer. These were as follows:

- The probe was modified to fit around the chest of the mouse in an attempt to resolve heartbeats.

- The probe was fitted with a new dual-wavelength LED emitting wavelengths more sensitive to gold nanoshells.

Formal testing of the photometer was accomplished using four mice that were injected with gold nanoshells and monitored with the photometer. The probe still needed to be attached to the mouse throughout the duration of the experiment. Therefore, experimental gold nanoshells having a circulation half life of less than one hour were used. An algorithm was developed and used to estimate the concentration of gold nanoshells in the vasculature of the mouse and was compared to concentration estimates computed using UV/Vis spectrophotometry.

3.3.1 Gold Nanoshell
Optical Properties

Experimental PEG coated gold nanoshells, optically similar to AuroShell™

particles, with a mean diameter between 160 and 170 nm were obtained from

Nanospectra Biosciences, Inc (Houston, TX). The preparation of clinical AuroShell

particles is a proprietary process, however, it has been previously reported that uniformity

of size and surface coatings along with sterile manufacturing combines to provide

consistent *in vivo* performance of gold nanoshells [96,97]. The received experimental

batches of nanoparticles were not prepared or packaged for clinical use and were not

stored or used under sterile conditions. Under these conditions, the circulation half-life

of the particles was expected to be shorter than previously reported [8,98]. Due to the

known confounders of motion artifact and transient changes in blood perfusion when

using optical densitometry [99], nanoparticles were employed which allowed a minimum

of two half-lives in one hour to be shown, a time-constraint which was related to the

ability to maintain a motionless subject under anesthesia in this formal feasibility study.

The molar extinction coefficients of the nanoshells were estimated by using the

Beer-Lambert law including the effects of scattering. The relationship $\mu_t = \mu_a + \mu_s$,

where μ_t is the total extinction coefficient (cm^{-1}) and μ_a and μ_s are the absorption and

scattering coefficients respectively was used, with the assumption that the nanoshells

were isotropic scatters. Both μ_a and μ_s can be defined by the number of absorbing or

scattering particles per unit volume in a medium multiplied by the effective cross-

sectional area. A convention to describe the number of moles of nanoshells per unit

volume (c_{NS} mol/L) multiplied by its molar extinction coefficient (M^{-1}cm^{-1}), which is the

sum of the absorption and scattering coefficients, was used.

$$\mu_a = c_{NS}\varepsilon_a$$

$$\mu_s = c_{NS}\varepsilon_s$$

ε_a and ε_s are the molar absorption and molar scattering coefficients respectively. The molar extinction coefficient of the nanoshells, ε_{NS}, is defined as the sum of the molar absorption and scattering coefficients.

$$\mu_t = c_{NS}\varepsilon_a + c_{NS}\varepsilon_s$$

$$\varepsilon_{NS} = \varepsilon_a + \varepsilon_s = \frac{\mu_t}{c_{NS}}$$

UV/VIS spectrophotometry was used to obtain an extinction spectrum of the nanoshells prior to injection in a 1 cm path length cuvette. The extinction coefficient of the nanoshells was found using the Beer-Lambert law where A is the measured extinction at a given wavelength given in units of optical density.

$$\frac{A}{c_{NS}} = \varepsilon_{NS}$$

The nanoparticles were employed at a concentration of 2.16×10^{11} particles/ml based on the independent measurement of their extinction spectrum using a UV/Vis spectrophotometer (Beckman Coulter DU 800). The extinctions of the stock batch, accounting for dilution, were 77.72 OD at 760 nm and 54.73 OD at 940 nm yielding molar extinction coefficients of 0.217×10^{12} and 0.152×10^{12} $M^{-1}cm^{-1}$ respectively. One mole of nanoshells is described as 6.02×10^{23} nanoshells.[100] A normalized extinction spectrum of the nanoshells can be seen in Figure 10.
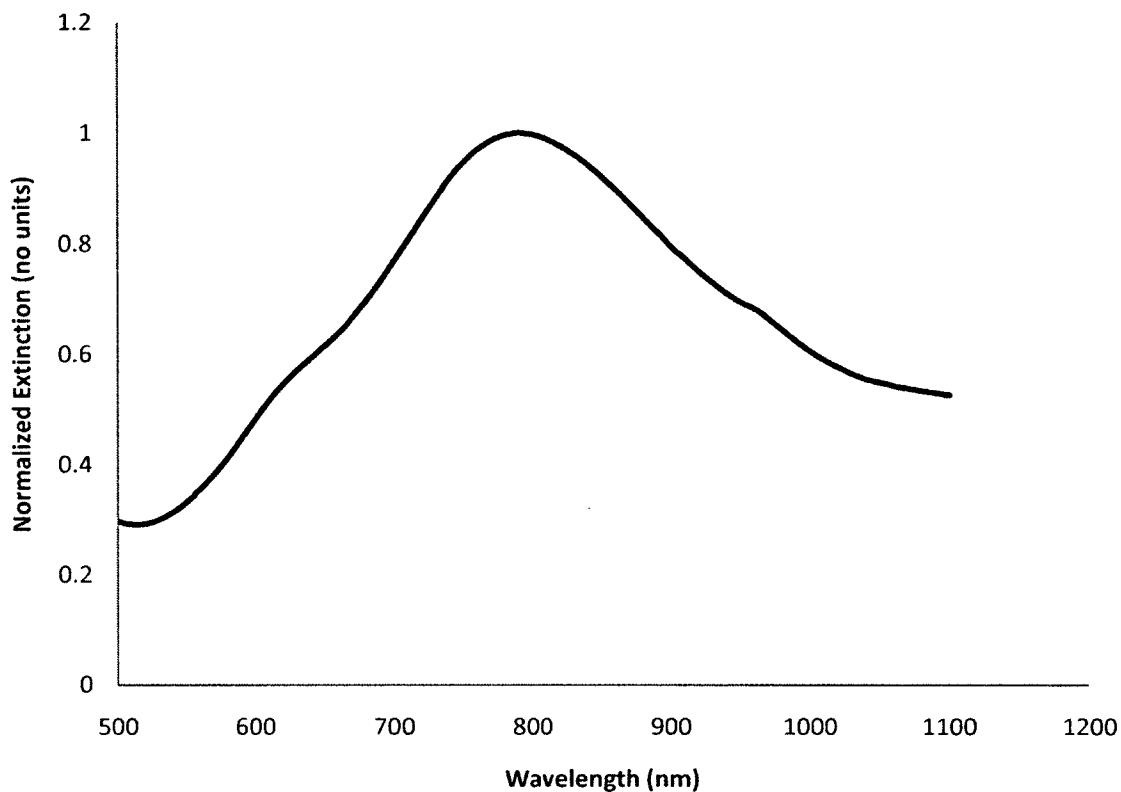
Figure 10. Normalized extinction spectrum of the experimental gold nanoshells.

3.3.2 Animal Protocol

Four female BALB/c mice (18-20g) were anesthetized (0.1ml/10g) using a ketamine (10mg/ml) and xylazine (1mg/ml) mixture during the hair removal and experimental periods. Hair on the dorsal and ventral thorax was removed at least 24 hours in advance of an experiment. During experiments, the core temperature of the subjects was set to 37 °C using a rectal thermometer coupled with a heating pad (Physitemp TCAT-2LV Controller, Clifton, New Jersey). Once the mice reached the target core temperature, their tail was submersed in 40-45 °C water for 20-30 seconds to induce vasodilation for catheterization. Catheters were prepared using 2 french

polyethylene catheter tubing and a 29 gauge needle. The catheter was inserted to the tail vein and secured. A second identical dose of the ketamine/xylazine was injected subcutaneously for slow release to maintain deep anesthesia prior to the start of the experiment. Subjects were then placed in a prone position and wrapped with the photometer around the thorax. The light source was facing the spine and the detector was facing the sternum. 100 μL injections of nanoshells were administered via catheter. The subjects were monitored with the photometer until the concentration estimate showed no circulating nanoparticles or for as long as the anesthesia prevented animal movement.

3.3.3 Blood Sample Analysis

Concurrent to monitoring with the photometer, the nanoshell concentration was estimated from an analysis of blood samples taken from the mouse. A previously validated technique, instrumental neutron activation analysis (INAA), has been used to verify and quantify the bio-distribution of gold nanoshells in dosing materials, blood, bones and other tissues [26]. However, this technique was not used in these experiments because of its high cost. A simple technique to quantify these particles in whole blood using UV/Vis spectrophotometry in low-volume cuvettes (Brandtech, Ultra-Micro Cuvettes) was developed. Prior to nanoshell injection, a 5 μL blood sample was taken from the mouse's tail using a heparinized pipettor tip. Similarly to a previously reported technique [27], the sample was then diluted and shaken in a micro-cuvette containing 95 μL of aqueous 10% Triton-X 100 (VWR) to lyse blood cells in order to reduce light scattering and to oxygenate the hemoglobin. The extinction was observed to decrease by 97% at 760 nm compared to an unlysed blood sample diluted in an isotonic PBS solution. The extinction between 500 and 1100 nm was measured. A 1:1 dilution of the blood

sample was then made with 100 μL of 10% Triton-X in order to measure the extinction at 578 nm, which is near the peak of the right q-band for hemoglobin. The concentration of hemoglobin was estimated using this peak wavelength, where nanoshells at typical concentrations in blood extinguish at least two orders of magnitude lower. Using a published value for the extinction coefficient of human oxy-hemoglobin [32] (54,728 cm^{-1}M^{-1}) the concentration of oxy-hemoglobin in the sample was calculated along with baseline extinction coefficients for oxy-hemoglobin at 760 and 940 nm. This was performed for each mouse independently since the empirical extinction coefficients varied from animal to animal.

After injection, blood samples were drawn from the animals and analyzed in the spectrophotometer concurrent to monitoring with the photometer. The dilution and measurement techniques described previously were used to process each nanoshell-laden sample. The calculated oxy-hemoglobin concentrations in each sample and the extinction coefficients for oxy-hemoglobin at 760 and 940 nm were employed as a baseline to determine the concentration of nanoshells per milliliter of blood in each sample. The extinction at 760 and 940 nm attributed to the oxy-hemoglobin baseline was subtracted from the total extinction in each sample to yield the extinction attributed to the nanoshells. After baseline subtraction and accounting for dilution, extinctions ranging from 0.24 to 7.408 OD at 760 nm were measured. From this extinction, and using the molar extinction coefficient from the nanoshell batch, the nanoshell concentration in the sample was calculated using the Beer-Lambert law.

$$A_{total} = A_{NS} + A_{HbO2}$$

$$C_{NS} = \frac{(A_{total} - \varepsilon_{HbO2} C_{HbO2})}{\varepsilon_{NS}}$$

ε_{HbO2} and ε_{NS} are the molar extinction coefficients (at either 760 or 940 nm) for oxy-hemoglobin and nanoshells respectively, and C_{HbO2} and C_{NS} are the concentrations of oxyhemoglobin and nanoshells respectively. The concentration of nanoshells is given in moles/L. This was then converted to nanoshells/ml blood.

$$\frac{C_{NS}}{ml\ blood} = C_{NS} * (0.1204 * 10^{23})$$

A study to test the accuracy of this technique was performed. 25 micro-cuvettes containing various known concentrations of nanoshells were mixed in Triton-X 100. 5 µl blood draws taken from a mouse were then added to each sample. The sample was then scanned with the spectrophotometer to obtain nanoshell concentration estimates. The measured concentrations at both 760 nm and 940 nm were compared with the known concentrations. Linear models were produced to predict the actual nanoshell concentration from the measured concentration. The models were specified to be linear regressions through the origin.

The average relative prediction of error (AREP) was found for both the 760 and 940 nm data. This describes the average percent error that can be expected between the measured and known concentrations of nanoshells for each measurement.

$$AREP = \frac{\sum_{i=1}^{n} \frac{x_i - y_i}{y_i}}{n}$$

x_i is the nanoshell concentration estimate, y_i is the known nanoshell concentration, and n is the number of samples in the data set. The AREP was 17.1% for the 760 nm measurements and 23.5% for the 940 nm measurements.

In order to assess the consistency of blood sample volume, the concentration of HbO_2 in each cuvette was determined. The average concentration of HbO_2 was 99.15

μM (1.98 mM in whole blood) with a standard deviation of 1.28 μM. This corresponds

to 1.3% of the average.

The linear models are used to predict the actual nanoshell concentrations from

measured UV-Vis spectra. The slope of the 760 nm graph indicates that the method tends

to underestimate the concentration when using the 760 nm wavelength, while the slope of

the 940 nm graph indicates that the method tends to overestimate the concentration when

using the 940 nm wavelength. The coefficient of determination, R^2, is close to 1 in both

graphs. This shows that the variability in the data is resulting from the measured quantity

of nanoshells (x-variable). The linear models can be seen in Figure 11 and Figure 12.
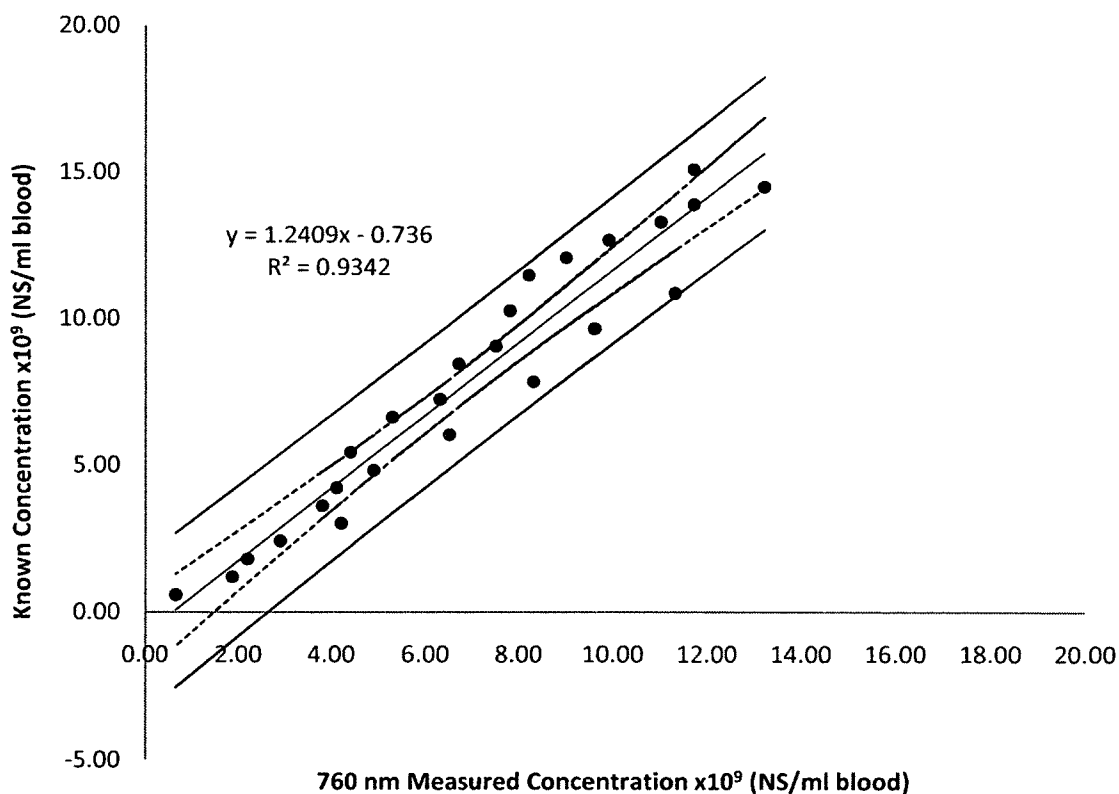
Figure 11. Linear model used to predict the actual NS concentration from the measured
concentration using extinction at 760 nm.
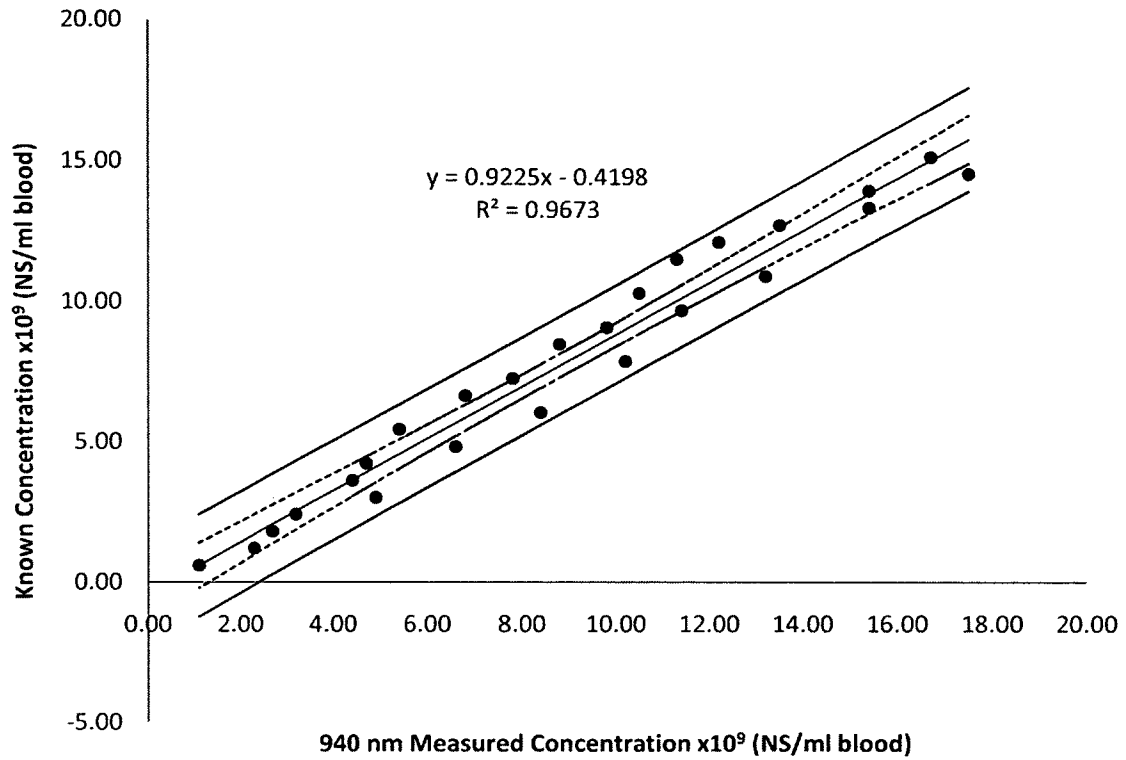
Figure 12. Linear model used to predict the actual NS concentration from the measured concentration using extinction at 940 nm.

The 90% confidence (dashed lines) and prediction (solid lines) intervals were produced for both linear models. The confidence intervals describe the confidence that the model can estimate the mean response (known concentration) at a given measured concentration.

$$\hat{\mu}_{y,x_0} - t_{\alpha/2,n-2} \sqrt{MS_{res}\left(\frac{1}{n} + \frac{(x_0 - \bar{x})^2}{S_{xx}}\right)} \leq E(y, x_0)$$

$$\leq \hat{\mu}_{y,x_0} + t_{\alpha/2,n-2} \sqrt{MS_{res}\left(\frac{1}{n} + \frac{(x_0 - \bar{x})^2}{S_{xx}}\right)}$$

$\hat{\mu}_{y,x_0}$ is the unbiased estimator of the actual concentration of nanoshells, $E(y, x_0)$, given a measured concentration, x_0. $t_{\alpha/2,n-2}$ is found from the t-distribution given a specific level of confidence, $100(1-\alpha)$, and sample size, n. MS_{res} and S_{xx} are parameters of the linear model and measured values respectively.

$$MS_{res} = \frac{\sum_{i=1}^{n}(y_i - \hat{y_i})^2}{n-2}$$

$$S_{xx} = \sum_{i=1}^{n} x_i^2 - \frac{(\sum_i^n x_i)^2}{n}$$

The prediction intervals describe how well the model can predict the actual concentration in future samples. The prediction interval at the same level of confidence is always larger.

$$\hat{\mu}_{y,x_0} - t_{\alpha/2,n-2}\sqrt{MS_{res}\left(1 + \frac{1}{n} + \frac{(x_0 - \bar{x})^2}{S_{xx}}\right)} \leq E(y, x_0)$$

$$\leq \hat{\mu}_{y,x_0} + t_{\alpha/2,n-2}\sqrt{MS_{res}\left(1 + \frac{1}{n} + \frac{(x_0 - \bar{x})^2}{S_{xx}}\right)}$$

Note that the data fall within the 90% prediction interval. Therefore, future measurements should also fall within this interval.

Each sample that was taken from an injected mouse was scanned with the spectrophotometer and then the linear model corresponding to 760 nm was used to determine the actual nanoshell concentration.

3.3.4 Instrumental Modifications

A few modifications to the photometer were made for this experiment. The clip was modified to fit around the thorax of the animal. Also, the 660/940 nm LED was

replaced by a 760/940 nm LED in order to make the photometer more sensitive to the

injection of nanoshells. All other instrumentation was the same as described previously.

Spectra of the new LED's can be seen in Figure 13.
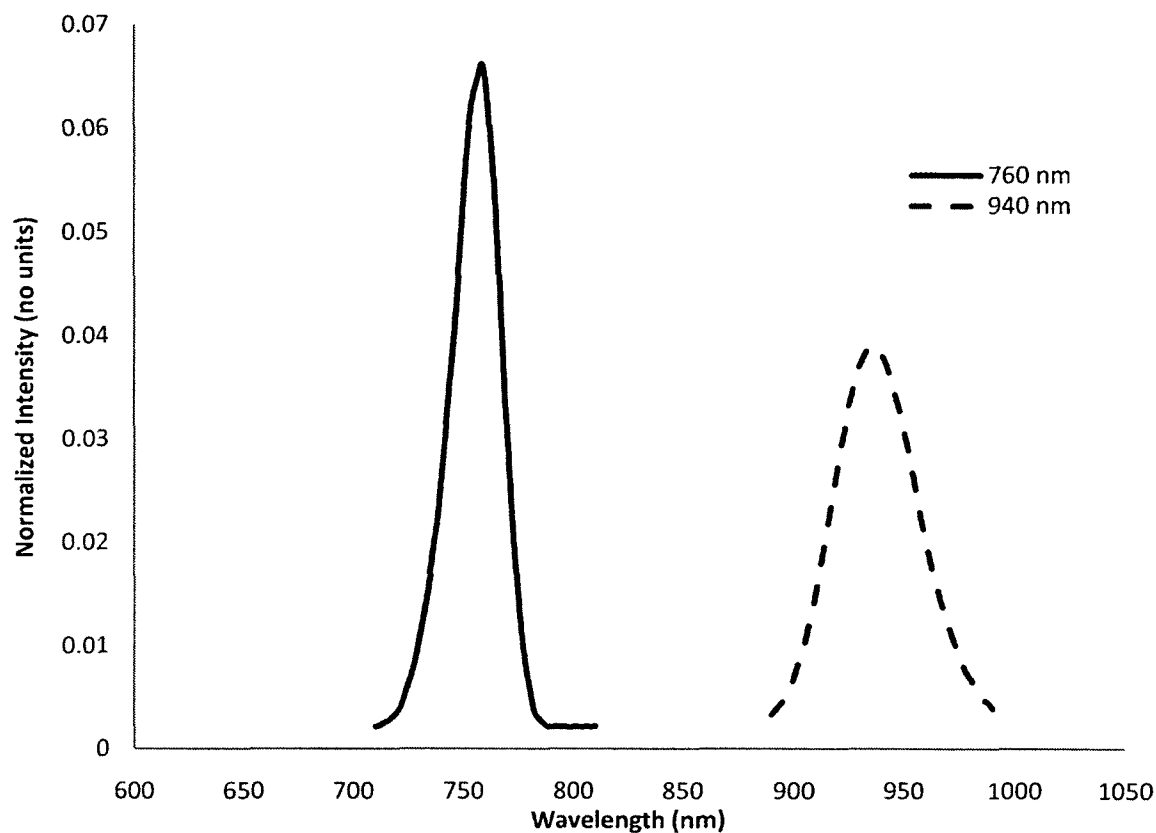
Figure 13. Spectra of the dual wavelength LED.

3.3.5 Algorithm

The photometer algorithm is implemented in a LabVIEW virtual instrument (VI)

which collects and processes the voltages at each channel. The signal from each channel

is collected in one second intervals and analyzed for export to a text file. Digital signal

processing is used to separate each channel into AC and DC components which are used

to measure nanoparticle extinction and circulation time. Separation of AC and DC

components is accomplished by using a DC magnitude detector VI and a 3rd order IIR

Butterworth digital bandpass filter (1-7 Hz passband) VI. The AC portions of each

channel are then passed through an AC magnitude detector and a pulse detector in order

to measure heart rate. The DC and AC magnitudes are displayed to the user, along with

the filtered and unfiltered signal. The elapsed time, heart rates, and DC and AC

magnitudes are saved to a file when the VI is prompted by the user. The change in

extinction and the estimated concentration of the nanoparticles is calculated in post-

experiment processing using the DC and AC magnitudes. The instrument was designed

with flexibility to employ multiple channels/wavelengths for anticipated improvements in

signal collection and algorithm development. This section describes the output of the two

channels independently, and preferentially reports the data from the channel (760nm)

closest to the peak wavelength of the nanoshells.

The photometer was attached to the mouse 15-30 minutes prior to injection in

order to minimize potential signal drift caused by animal movement and physiological

changes. The photometer collects 5 minutes of steady baseline data prior to the start of

each injection, the first point of which is used as a baseline, analogous to using a blank

sample in a spectrophotometer. After injection the DC and AC signal components are

converted into extinction changes (ΔA) caused by the injected nanoshells.

$$\Delta A = A_{post-inj} - A_{pre-inj} = \log(\frac{I_0}{I - \Delta I})_{post-inj} - \log(\frac{I_0}{I - \Delta I})_{pre-inj}$$

The voltage produced by the photodiode circuit is proportional to the intensity of

the light, and since I_0 is the same pre and post-injection, I_0 can be eliminated from the

equation. Assuming that all tissue and blood factors are constant for the duration of the

experiment, the extinction caused by the injection of nanoshells can be isolated as the difference between the pre-injection term and the post injection term.

$$\Delta A = \log(V_{DC} - V_{AC})_{pre-inj} - \log(V_{DC} - V_{AC})_{post-inj}$$

The extinction change measured in the chest is used to estimate the concentration of nanoshells that extinguish light in the circulating blood. V_{DC} is the voltage measured when the heart is in systole and represents the intensity of light penetrating the non-pulsatile blood and tissue, I. When the heart is in diastole, a small decrease in the intensity of light results from a localized increase in path length due to the transient pulse of blood , ΔI, and therefore a small decrease in voltage (V_{AC}) is observed. V_{DC} and V_{AC} change post injection. These post injection signals are processed and then subtracted from the baseline pre-injection term established before the nanoshells are injected. This subtracts the extinction caused by all tissue and blood factors and isolates the extinction caused by the nanoshells removing the requirement to know the molar extinction coefficient or concentration of the mouse tissue. This is then converted to absolute units in terms of the number of nanoshells per blood volume.

$$\frac{\Delta A}{\varepsilon_{NS} d} * (6.02 * 10^{23}) * \frac{mass_{mouse}}{density_{mouse}} * \frac{1}{1000} * \frac{1}{BV_{mouse}} = \frac{c_{NS}}{ml\ blood}$$

ε_{NS} is the molar extinction coefficient for nanoshells, d is the path length of the light propagation (cm), and BV_{mouse} is the blood volume of the mouse (ml) estimated using a ratio of 2 ml/30 g. The subject mass (g) and the path length (d) of the mouse chest were measured and the density of the mouse was estimated to be approximately the same as the density of water (1 g/ml).

3.3.6 Circulation Times

The circulation time of the nanoshells was determined in each animal using both the

photometer and blood draws measured with the UV/Vis spectrophotometer. A

spreadsheet was used to plot these data and compare them by fitting them to a decaying

exponential model. This was done for both the 760 and 940 nm wavelengths.

$$A(t) = A_0 e^{-\frac{t}{\tau}}$$

$A(t)$ is the extinction change as a function of time, A_0 is the maximum extinction change

seen immediately post injection, and τ is the time constant that describes the rate of

nanoshell clearance. Circulation half life ($t_{1/2}$) is obtained using τ.

$$t_{1/2} = \ln\left(\frac{1}{2}\right) * \tau$$

3.3.7 Results

To gain familiarity on the nature of the optical medium of a murine subject, the

transmission of light through the chest of an animal without injection of nanoshells was

measured at both 760 and 940 nm. The power of the LED's measured with a calibrated

optical power meter (Thorlabs PM100 Optical Power Meter Console/S120B Silicon

Detector), the spectral efficiency curve the photodiode, and gain of the amplifier circuit

used in the photometer were used to determine the amount if light transmission. The

extinctions of the chest at 760 and 940 nm were 3.39 OD and 3.47 OD respectively.

These values correspond to 0.04 % transmission at 760 nm and 0.03 % transmission at

940 nm.

Circulation half lives of the nanoshells were determined in each of the four mice using the extinction measured with the photometer and the UV/Vis spectrophotometer. The clearance curve taken post-injection of mouse A can be seen in Figure 14.
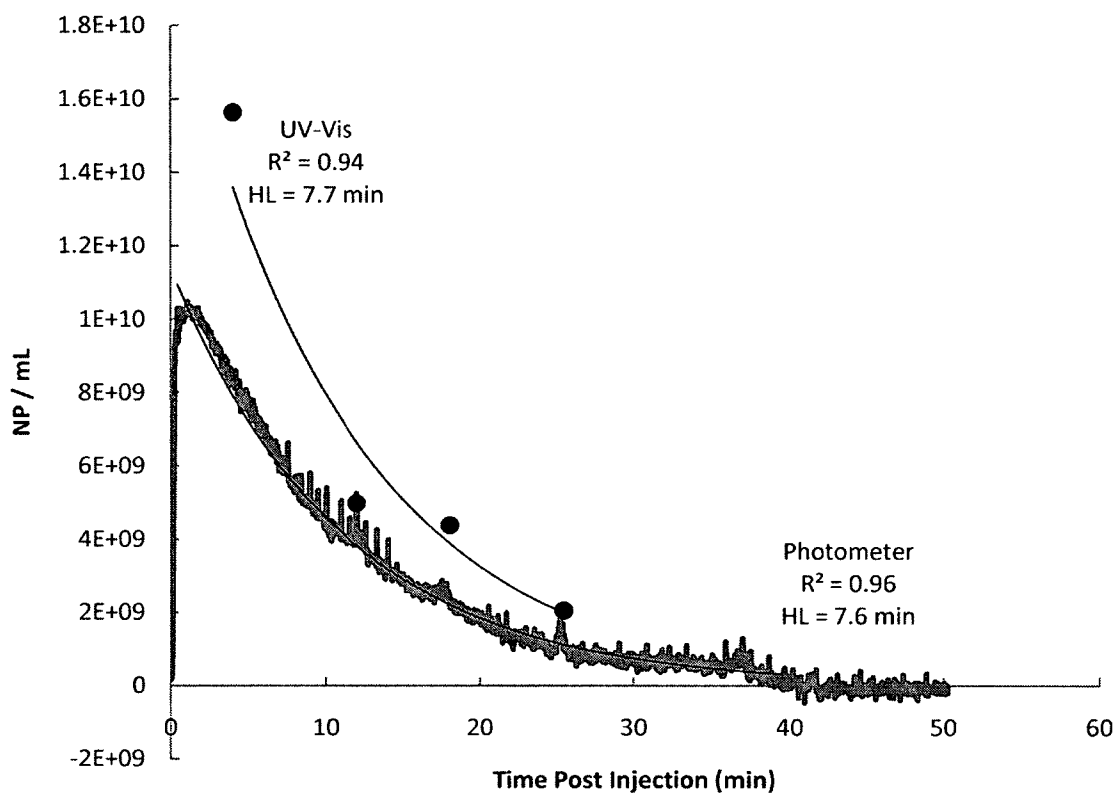
Figure 14. Exponential decay of nanoshell concentration with time measured with both the prototype photometer and UV Vis spectrophotometry.

The data for both methods tended to fit exponential decays with high average correlation coefficients ($R^2_{avg} = 0.861$ for photometer and $R^2_{avg} = 0.846$ for UV/Vis). Table 2 shows the circulation half lives for each mouse using both methods and at both wavelengths. The bioavailability curves for mice B, C, and D can be seen in APPENDIX D.

Table 2. Circulation half lives estimated using spectrophotometry (UV/Vis) and with the prototype photometer (P).

Mouse	Circulation Half-Life (min)			
	P (760)	UV/Vis (760)	P (940)	UV/Vis (940)
A	7.6	7.7	19.3	7.8
B	22.3	12.6	18.6	20.4
C	2.6	3.2	3.3	4.4
D	43.9	79.6	112.2	73.7

The average relative error of prediction between the two methods was 35.5% or 12.0 minutes. To calculate point photometer concentrations for comparison with the UV/Vis points, the average concentration was found over one minute of data using the UV/Vis time value as the midpoint. Nanoparticle aggregation was not observed from an analysis of the spectral characteristics of nanoshells in drawn blood sample.

The correlation between measurements made using both the photometer and the UV/Vis spectrophotometer was analyzed. Open-source R statistical software (www.r-project.org) was used to produce a linear model for the data. This analysis was done for both the 760 and 940 nm wavelengths.

A linear model specified as regression through the origin describing the correlation between the two measurement techniques was produced for each wavelength. The R^2 value for this model was 0.752 ($y = 0.468x$, $n = 21$, $p < 0.001$) shown in Figure 15. This suggests linear correlation between the two methods. The R^2 for the IR measurements was 0.555 ($y = 0.654x$, $n = 19$) (not shown).
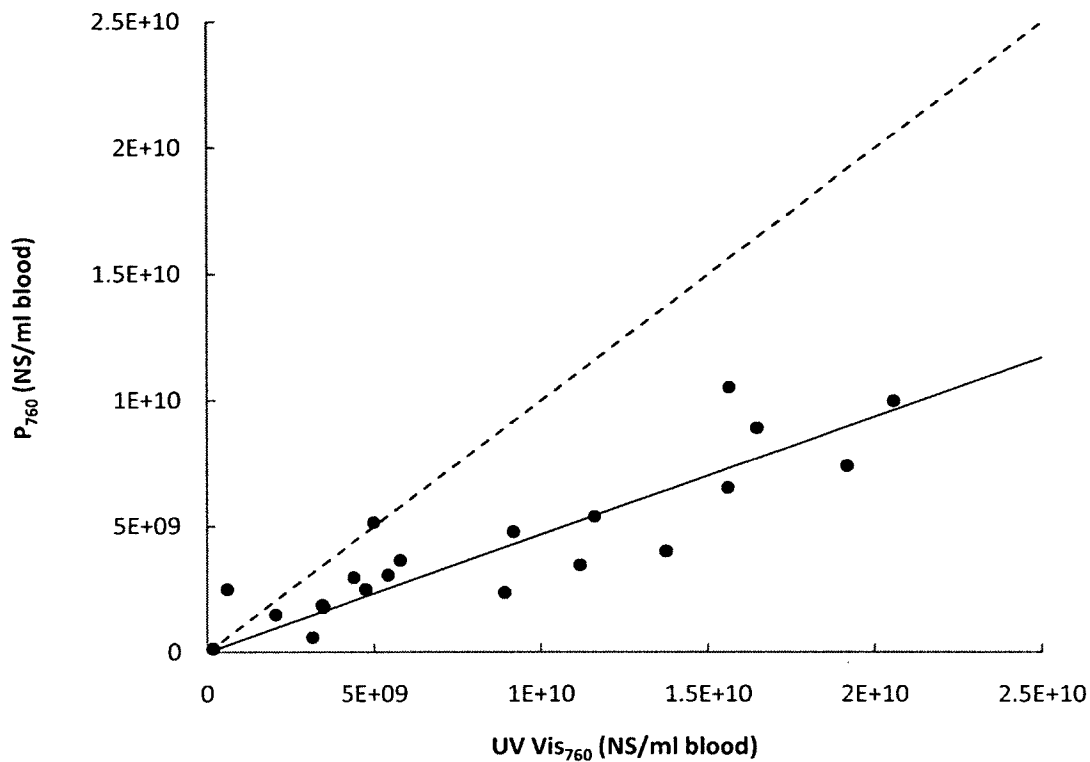
Figure 15. Linear model showing the correlation between the NS measurements made using the prototype photometer and UV Vis spectrophotometry at 760 nm. The dashed line shows a slope of unity as a reference.

A Bland-Altman analysis [101] was conducted to provide additional comparison between the two methods. The differences in estimated nanoshell concentration between the two methods were computed and plotted with respect to their means. The bias (average difference) and the precision (two standard deviations above and below the bias) were calculated (Figure 16).
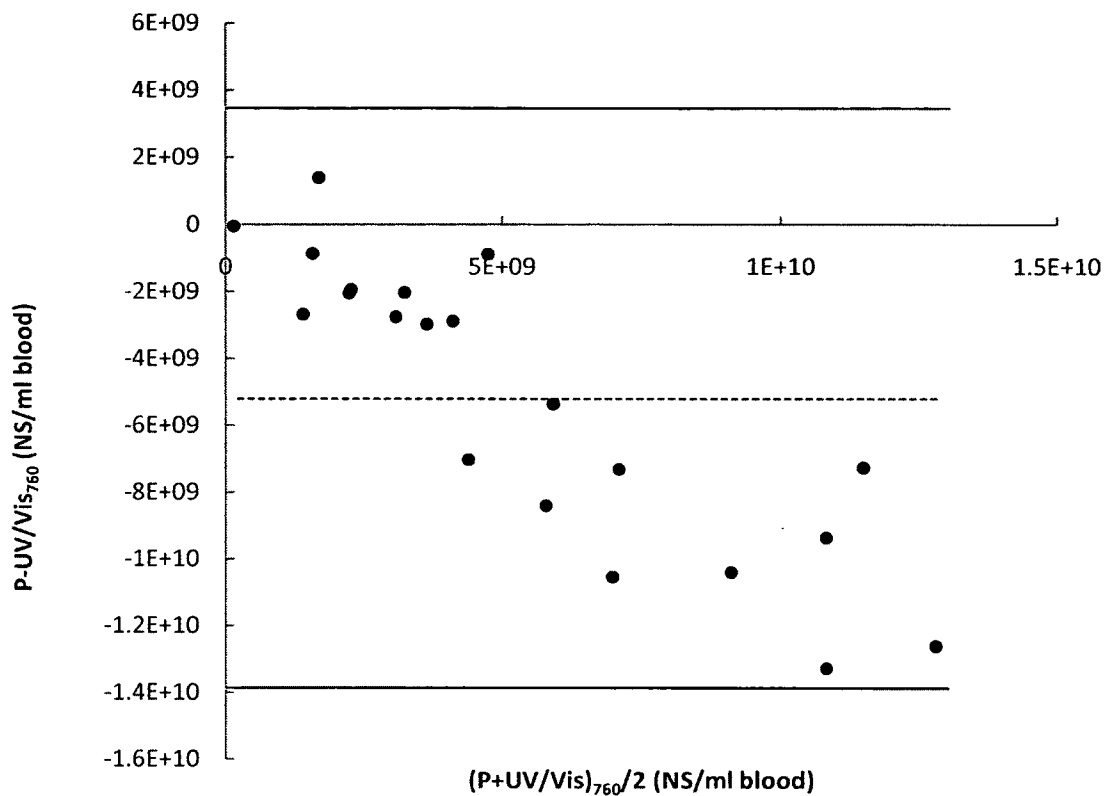
Figure 16. Bland-Altman plot showing the bias and precision between the measurements using the PP and UV/Vis.

The bias between the two methods at the 760 nm wavelength was -5.201 x 10^9 NS/ml blood, which corresponds to 1.795 OD in whole blood in the animal, and the precision was 8.666 x 10^9 NS/ml blood corresponding to 2.9909 OD in whole blood. This indicated that the photometer tended to underestimate the concentration of nanoshells. The bias at the 940 nm wavelength was -1.997 x 10^9 NS/ml blood, which corresponds to 0.499 OD in whole blood in the animal, and the precision was 5.783 x 10^9 NS/ml blood corresponding to 1.445 OD in whole blood in the animal.

3.3.8 Discussion

The choice of the interrogation wavelengths was based on both the extinction spectra of the nanoshells and endogenous absorbers found in tissue. The 760 and 940 nm wavelengths were chosen to exploit the tissue optical window between 600 and 1000 nm to produce the maximum light transmission while enhancing the transmission change upon the addition of nanoshells to the tissue. Two wavelengths were qualitatively used to verify the signal changes caused by nanoshells since they appeared on both channels, although at different characteristic intensities dependant on the difference in the extinction coefficients of the nanoparticles at these two wavelengths. The ratio of the extinction changes at 940 and 760 nm was calculated for one minute immediately after injection. According to the nanoshell extinction spectrum, this ratio should have been approximately 0.70. The average ratio for the four mice was 0.93, which was higher than expected, but suggested a more rigorous multi-wavelength analysis for future designs was needed. This discrepancy could be the result of non-identical path lengths for each wavelength and/or because of the broad spectrum of the LED's. Improvement in probe design and placement might serve to remedy this problem.

Prior to the experiments, several probe placement sites for the photometer were examined. The probe was attached to the tail, leg, and thorax of several animals to establish the probing site with the strongest pulsatile signal and the least amount of DC signal drift. The thorax produced a pulsatile signal up to one order of magnitude stronger than that seen at the tail or the leg. A large amount of DC signal drift was observed when the probe was attached to the leg, possibly because the pressure and placement of the probe caused local blood flow and peripheral temperature to reduce over time. Stable DC

signals from the tail could be obtained, but the pulsatile signal was often very weak and erratic with a low signal-to-noise ratio in this prototype. Initially it was observed that respiratory artifact could be a potential confounder in our measurements across the thorax. Proper administration of anesthesia and probe placement was used to control this confounder.

Table 1 presents several discrepancies between the circulation times estimated using the photometer and the UV/Vis technique. The UV/Vis estimates were assumed to be more reliable since they tended to agree at both wavelengths and because of the goodness of fit of the data shown in Figure 14, although restrictions on the quantity of blood removed from the animal models limited the curve fit from the blood draws to between four and six points. Large differences in circulation times were seen in the 940 nm prototype measurement in mouse A and in both measurements in mouse D. These are due to shifts of the probe during the experiments, which may artificially suggest a shorter or longer half life based on the shifting baseline extinction of the tissue. This highlights a need for better probe design and suggests analysis of the pulsatile signal in future prototypes.

Linear fit models of the data at both wavelengths revealed that there was a correlation between the values calculated using UV/Vis spectrophotometry and the photometer. However, a Bland-Altman analysis revealed a negative bias when comparing photometer estimates to direct UV/Vis spectral analysis from blood samples. This is observed in the bias estimates of each channel independently and implies that the photometer tends to underestimate nanoshell concentration.

The Bland-Altman analysis implies that the absolute difference between measurements appears to be proportional to the average measurement of nanoshells. This may have resulted mainly from the simplified approximations employed in both algorithms, heterogeneous distribution of nanoshells in the thoracic and peripheral blood volume, the transient dilution of the blood from the injection, errors in our estimates of the density, mass, and path length of the mouse, and from instrumental/physiological issues causing erratic measurements. For example, the optical path length through the mouse is estimated by measuring the thorax with a digital caliper and a homogenous distribution of nanoshells in the tissues is assumed. This approximation may have yielded significant inaccuracy in calculations of nanoshell concentration, but does not affect the estimates of circulation time.

Commercial pulse dye-densitometer systems isolate the pulsatile transmission from the DC transmission at multiple wavelengths in order to obtain the concentration of dye in the pulsing blood and to eliminate the need for measurements such as density, mass, and path length. This is done by exclusion of the DC extinction and calculation of dye concentration using only the change in extinction, ΔA, which can be approximated by $\frac{V_{AC}}{V_{DC}}$ for a given wavelength. Upon addition of an optical absorber, ΔA should increase at each wavelength and is used in ratiometric calculations to yield a corresponding dye concentration. The ratio of ΔA at two wavelengths (760nm and 940nm) did not behave in the predicted fashion and therefore was not used to calculate nanoshell concentration. This may have been a result of issues related to using small animals such as unstable blood oxygen saturation, erratic tissue perfusion, low AC signal strength resulting in inability to accurately detect pulsatile data corresponding to the heart beat, and the small

size of murine anatomy relative to the probe. This initial empirical study thus employed *both* the DC and AC extinction caused by the addition of the nanoshells.

Feasibility of using photometry to noninvasively quantify circulating nanoshell concentration *in vivo* was demonstrated, and though the prototype was susceptible to variable optical interference and motion artifact, future designs would incorporate standard electronic techniques to deal with these confounders. Photometer modifications would be made with the addition of more sophisticated optical/electrical instrumentation and algorithms using multiple wavelengths concentrating on the AC signal in appendages. Improved modeling of the contribution of absorption and scatter due to background tissue and blood as well as nanoparticles would yield improvements to accuracy.

3.4 Examining Pulsatile Signals Using the Prototype I Photometer

Several improvements in the photometer were made since the first formal experiment. It was clear that the technique was feasible, but in order to employ examination of only arterial blood, an analysis of only the pulsatile signal was necessary. This would be done by accurately measuring the magnitude of the arterial pulse at two wavelengths to determine the ratiometric parameter, R, similar to that used in pulse oximetry. The difference would be in using the wavelengths of light used in 3.2. A detailed explanation of this can be seen in Appendix A and a detailed schematic can be seen in Appendix B.

Measurement of the change in R (ΔR) was demonstrated in a preliminary experiment. A probe was built that could be attached to the leg of a mouse and contained the same dual wavelength LED and photodiode as used in the first prototype. The leg

was chosen as the probing site in order to eliminate respiratory artifact and to examine an anatomical location where more light penetration was possible. The purpose of this experiment was to obtain a change in R resulting from the injection of nanoshells that would return to baseline as the nanoshells were eliminated from the circulation.

The same experimental protocol as used in the first formal experiment was followed with the omission of the blood draws. A female BALB/c mouse was anesthetized with the ketamine/xylazine cocktail and the tail vein was catheterized. The probe was then attached to the leg and a baseline measurement of R was obtained. Signal stability was assessed qualitatively by examining a steady pulse rate for both wavelengths.

A baseline measurement of 0.8298 was obtained having a standard deviation of 0.0161 over a thirty second interval. A 100 µL injection of the nanoshells used in the previous experiment was delivered via the catheter and the change in R was recorder by the photometer. The data was collected for approximately 80 minutes after the injection and was then analyzed in Excel. A 15 second moving average was calculated in order to smooth the signal which can be seen in Figure 17.
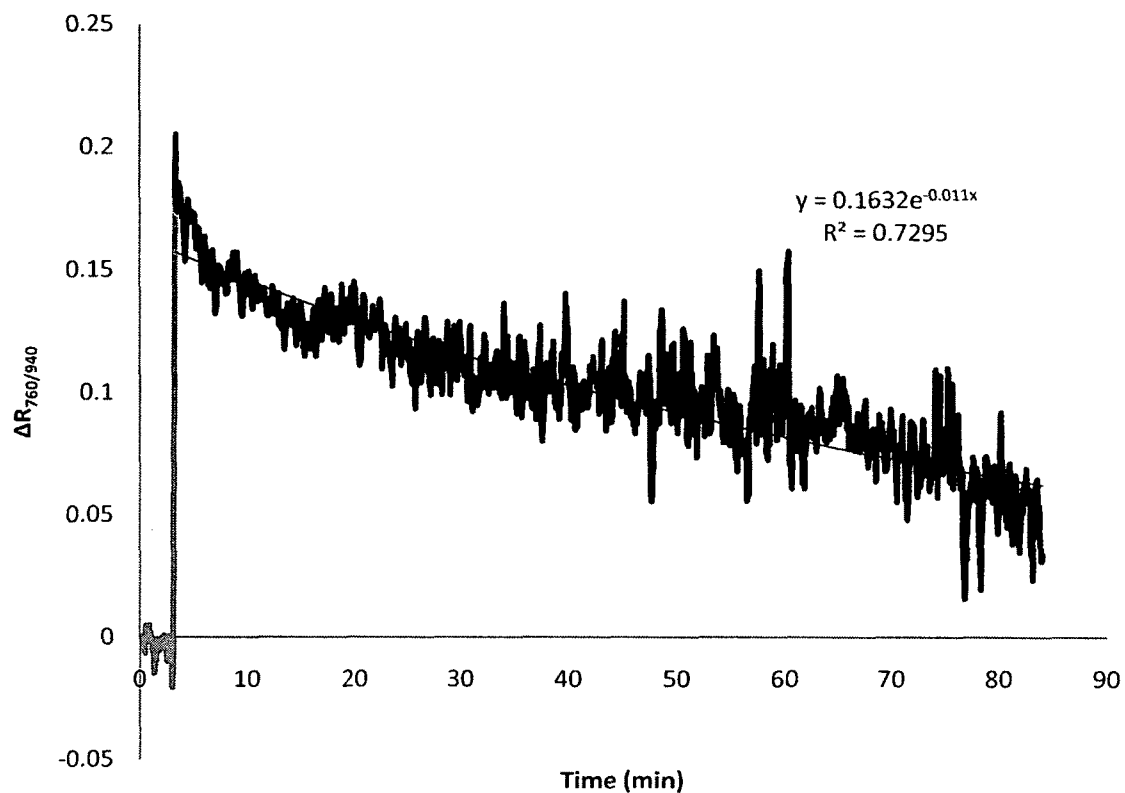
Figure 17. $\Delta R_{760/940}$ measured after the injection of nanoshells.

Several pieces of information were obtained from this preliminary experiment. A positive change in R was noted after the injection, which was expected based on the spectra of oxyhemoglobin and nanoshells. R returned to baseline following a fitted exponential decay curve having a half life of approximately 60 minutes and an R^2 of 0.7295. The signal that was obtained showed the appropriate trend, but tended to be noisy. This was also apparent in the erratic measurement of the pulse rate as qualitatively assessed. The LabVIEW pulse detection VI automatically produces a pulse rate measurement for every second of data analyzed. Therefore, if an erratic signal is collected, it was likely that an erroneous estimate of pulse rate was reported. This

prompted the need for better signal collection which would be accomplished by better probe design. Also, since this experiment was only performed on one animal, it reproducibility had not been established. Therefore, it was not known if the baseline measurement of R was reproducible. Since R is highly dependent on the blood oxygenation, it was clear that this may have been variable during this experiment and would need to be controlled in the future. Lastly, this experiment did not address the issue of probe removal and reattachment for monitoring long circulating particles. It was clear that if the animal remained motionless, ΔR could be measured over time and therefore short circulating particles could be monitored. However, the next set of experiments would need to address probe removal and reattachment since therapeutically administered nanoshells would show a much longer circulation.

CHAPTER 4

DEVELOPMENT AND TESTING OF THE
PROTOTYPE II PULSE PHOTOMETER

The fact that the photometer could only monitor an animal for the duration of injected anesthesia was a very significant limitation. This meant that only particles with short circulation half lives could be monitored and that the animals must remain motionless during the experiments. A prototype II pulse photometer was developed which addressed several of the limitations of the first prototype. The improvements to the instrumentation were as follows:

- CMOS logic circuitry was implemented in order to increase the number of data collection channels from two to eight.

- A channel was designated which would collect data while no LED's were emitting, allowing for subtraction of signals due to ambient light.

- New probes were purchased from Starr Life Sciences, which are currently used in a commercially available murine pulse oximetry system, MouseOx™.

- The probes were fitted with a new four wavelength LED allowing for future multi-wavelength analysis.

- The gain of the current to voltage amplifier connected to the photodiode was changed to 1 MV/A in order to reduce some of the inherent noise

- The circuit was soldered on a specially printed circuit board and was mounted in a protective case.

- The probes and case were fitted with standard connectors to allow easy probe, power, and data channel connection and disconnection.

- A ratiometric parameter, R (mathematical definition given in 2.2 Pulse Oximetry), which is a ratio of optical densities at two-wavelengths, one more sensitive to gold nanoshells than the other, was now used to empirically determine the vascular concentration of gold nanoshells.

A modified experimental protocol was also needed since this next set of experiments was designed to monitor long circulating clinically relevant gold nanoshells. Improvements to the experimental protocol were as follows:

- Rapid delivery of light anesthesia was achieved with the use of an oxygen concentrator connected to an isoflurane vaporizer donated to by Dr. Elysse Orchard, a consulting veterinarian from LSUHSC. This allowed the mice to be immobilized and measured at several time points over 10 hours with full and quick recovery.

- The use of oxygen also ensured that arterial oxygen saturation remained constant during the measurements.

- Mild hyperthermia was induced using the temperature controlled heating pad in order to cause vasodilation making pulsatile signals easier to detect.

- The probe was moved to the foot of the animal, which eliminates the need for hair removal and is an optically accessible location with high perfusion.

The term pulse photometer (PP) is used to refer to prototype II since it is measuring the change in the extinction of light due to pulsatile arterial blood. In this next experiment, this new prototype was subjected to formal murine testing in order to verify its utility for *in vivo* vascular long circulating gold nanoshell monitoring.

4.1 Monitoring of Long Circulating Gold Nanoshells

4.1.1 Gold Nanoshell
Optical Properties

Gold-coated silica-core nanoshells conjugated with a monolayer of PEG were obtained from Nanospectra Biosciences. The optical densities of the batch were 119.82 and 95.53 cm^{-1} at 805 and 940 nm respectively as determined by UV/Vis spectrophotometry. A normalized spectrum of these nanoshells can be seen in Figure 18.
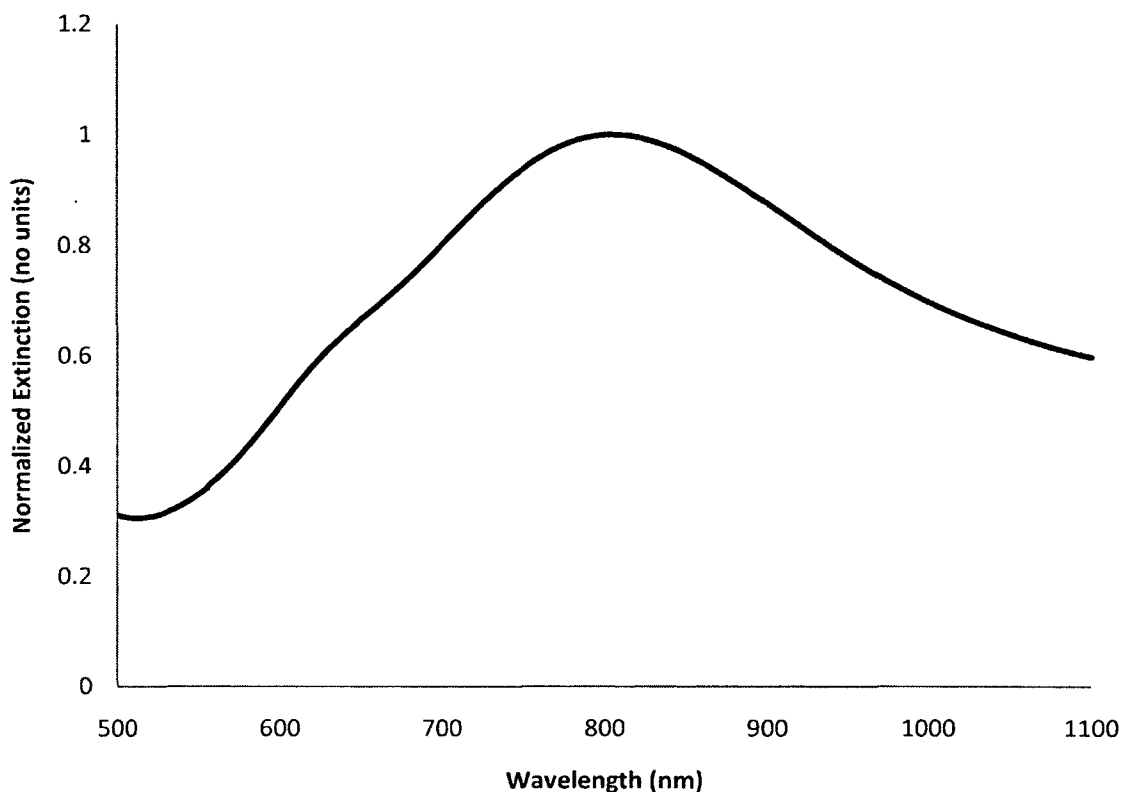
Figure 18. Normalized extinction spectrum of the long circulating gold nanoshells.

4.1.2 Blood Collection and Analysis

Five female BALB/c "retired breeder" mice, weighing between 26 and 32g, were

used in this study. Concurrent to measurements taken with the pulse photometer, blood

was sampled from each subject at each time point and analyzed with spectrophotometry.

A 5 μL blood draw was taken from the tail and diluted into a micro-cuvette containing 95

μL of 10% Triton X-100 to eliminate scattering blood cells from the sample. The

extinction at 805 was then measured. Then, an additional 100 μL of Triton X was added

to the sample in order to resolve the strong extinction of oxy-hemoglobin at 560 nm. The

sample was scanned again and the extinction at 560 nm was used to establish the

hemoglobin concentration using the extinction spectrum of oxy-hemoglobin [31]. This value was used to subtract the contribution of oxy-hemoglobin from the extinction at 805 nm in the original sample and calculate the extinction caused by the nanoshells. This value was then scaled by the dilution factor to derive the extinction by nanoshells in the whole blood.

The *ex vivo* spectrophotometric technique was validated by comparison to instrumental nuclear activation analysis (INAA). After analysis with spectrophotometry, the blood samples were then transferred to INAA vials, dried, and delivered to the Texas A&M Elemental Analysis Laboratory for analysis similar to what has been previously reported [102]. The gold content (μg) in each vial was determined and compared to the measurements taken using spectrophotometry. This data is presented in Section 4.2.

4.1.3 Instrumentation

Several improvements were made to the photometer to produce the second prototype PP capable of multi-channel data collection. Probe modifications and circuit redesign were implemented to produce this new prototype.

The animal/probe interface of the pulse photometer was modified. In the first prototype, the probe was placed around the chest of the animal. Previous measurements of pulsatile signals indicated that this probe placement yielded signals often confounded by respiratory artifact. The chest is also a very non-homogenous probing volume, therefore slight shifts in the probe would result in potentially drastic changes in probing volume. Specially designed clips compatible with mouse anatomy were purchased from Starr Life Sciences. These clips can attach comfortably to a mouse's tail, foot, or leg without applying excessive pressure. Several clips containing no opto-electronics were

purchased and modified by the addition of a photodiode (Hamamatsu S1337-33BR) and four-wavelength LED (Marubeni L660/735/805/940-40B42). These new LED's are off the shelf opto-electronic components that contain wavelengths of 660 nm, 735 nm, 805 nm, and 940 nm. For this experiment, 805 nm and 940 nm were chosen as the interrogation wavelengths. The 805 nm wavelength was chosen to more closely match the maximum extinction peak of the batch of nanoshells used. This is near the wavelength of maximum optical density for typical nanoshell batches. Spectra for each LED can be seen in Figure 19.
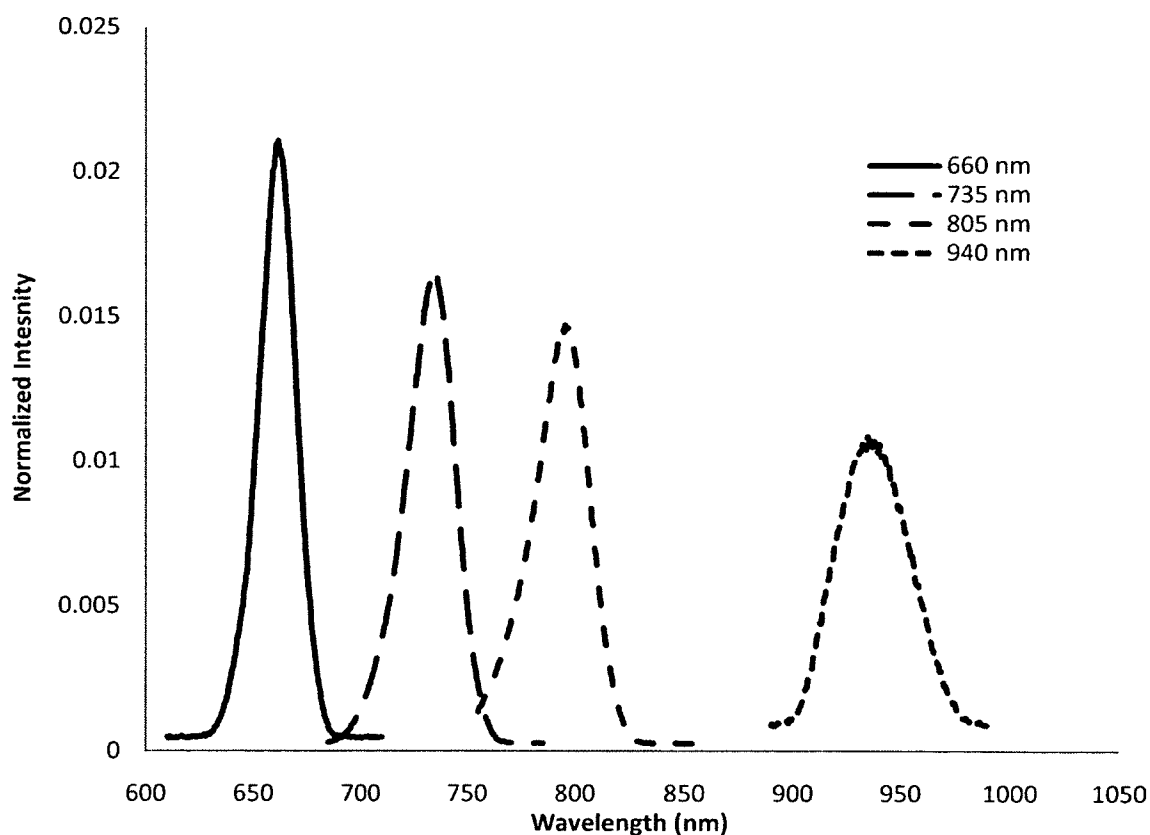
Figure 19. Spectra of the four-wavelength LED.

The circuitry of the pulse photometer was modified to allow the use of eight channels as compared to the two channel instrument described previously. This was done by using logic circuitry to count through eight channels and synchronize the sample and hold chips with the LED emission at each wavelength. The timer chip was replaced with a multivibrator chip (CD4047BCN) configured in astable free running mode producing pulses at a rate of 1.19 kHz and driving a 3-bit counter (MM74HC393N). This is fed to a 3-to-8 decoder (MM74HC138N) separating pulses amongst eight different channels, each having pulse repetition rates of approximately 150 Hz with an approximately 15% duty cycle. This is adequate to collect the PPG of a mouse (typically less than 500 beats/min). These pulses are inverted (MM74HC04N) and used to control the sample and hold circuits from the first prototype. This permitted the addition of a channel specifically used to detect ambient light and subtract it from the signals collected during the emission of each wavelength. The signals from the sample and hold chips are then fed through a first order analog filter ($F_c \approx 28$ Hz) for smoothing and attenuation of power line interference and then collected with an ADInstruments DAQ card set to 10,000 samples/sec. The pulses from the decoder are sent to buffers (LM324N) to supply power to the LED's. The LED package is configured having a common anode and separate cathodes for each wavelength. The anode is biased with the 5 volt supply used to drive the logic circuitry. The signals from the counter are therefore inverted in order to synchronize the sampling of one channel with the emission of its corresponding wavelength. A schematic of the modified circuitry can be seen in Figure 20.
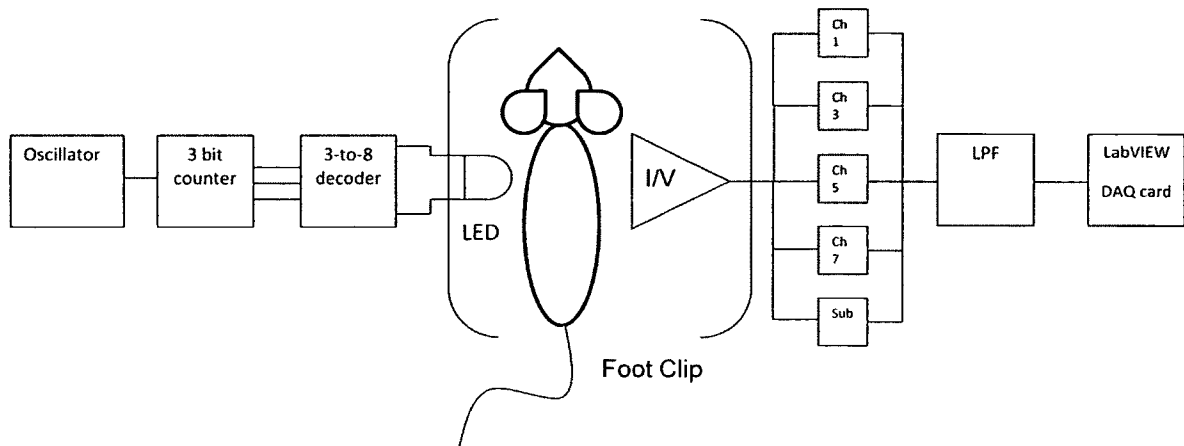
Figure 20. Block diagram of the pulse photometer circuitry.

The circuitry was also transferred from a prototyping board to a printed circuit board. The circuit board was designed using computer aided design software and sent off to ExpressPCB for patterning. Integrated circuit mounts were soldered to the board to provide easy insertion and removal of the IC chips without destroying the board. The board was then mounted inside of a 6" x 4" x 2" encasing (RadioShack) to help protect the circuitry. Connectors were mounted in the casing for the power, probe, and data output connections. This allowed for easy swapping of probes and connection and disconnection of the power and data lines. A picture of the device can be seen in APPENDIX C.

The data acquisition card collects the data from the circuitry and imports it into LabVIEW in 1 second waveforms on separate channels for analysis. The LabVIEW software first subtracts the signal from the ambient light channel from both the 805 nm and 940 nm signals. These are then separated into their AC and DC portions by available LabVIEW modules. A third order Butterworth bandpass filter (4-10 Hz passband corresponding to heart rates between 240 and 600 bpm) is used to condition the AC

signals and remove unwanted frequencies. The parameter, R, is then computed from the AC and DC components of both signals (λ_1 = 805 nm and λ_2 = 940 nm) and is displayed in real time. An averaging algorithm is used to produce average values of R and the standard deviation of R over a time interval specified by the user.

4.1.4 Data Collection

Prior to injection of nanoshells, the animal was anesthetized with isoflurane vaporized (Dentry Biomedical, Inc. Isoflurane Vaporizer) with 95% oxygen delivered with an oxygen concentrator (Invacare 5). A schematic of the anesthesia setup can be seen in APPENDIX C. Isoflurane/oxygen flow is controlled by a three-way valve that supplies flow to either a small gas chamber or a cone that fits around the mouse's snout. The oxygen is supplied by an oxygen concentrator set to 1 L/min flow rate. The concentrator was allowed to reach nominal oxygen output as indicated by the device before gas was delivered. The mouse was then placed inside the gas chamber and isoflurane was delivered with a vaporizer set to full output. Once the mouse was motionless, she was then removed from the chamber and her snout was placed in the cone. The vaporizer was then set to 20% isoflurane output and the valve was switched to deliver gas to the cone to maintain anesthesia. This anesthesia apparatus was contained in a surgical suite with a downdraft and a scrubber to eliminate any isoflurane exposure. The tail vein was catheterized with a 29 gauge needle connected to polyurethane tubing. The concentrator delivered anesthesia as well as maintained stable blood oxygen saturation during the measurement. Once the vein was catheterized, the animal was placed on a feedback controlled heating pad (Physitemp TCAT-2LV Controller) set to 40° C to stabilize the core temperature and induce vasodilation. Vasodilation enhanced

the peripheral circulation, and thus the detected AC signal strength. Once temperature

stabilization was achieved, the probe was placed on the animal's foot and the PP was

allowed to collect data. Thirty second averages of the values of R were computed to

assess signal stability. Anticipating potential transient problems such as motion artifact

or low perfusion, the signal was deemed acceptable once the AC magnitude was above 5

mV peak-to-peak and the standard deviation of R was less than 0.03. This R, assessed at

near blood oxygen saturation, was used as a baseline for all subsequent measurements in

that subject. A bolus injection of nanoshells at 4.5 μL/g was then given via the tail vein

and ΔR was calculated. To find the ΔR for each time point, the baseline reading from

that particular animal was subtracted from the current R measurement. An example of

ΔR measured after injection can be seen in Figure 21.
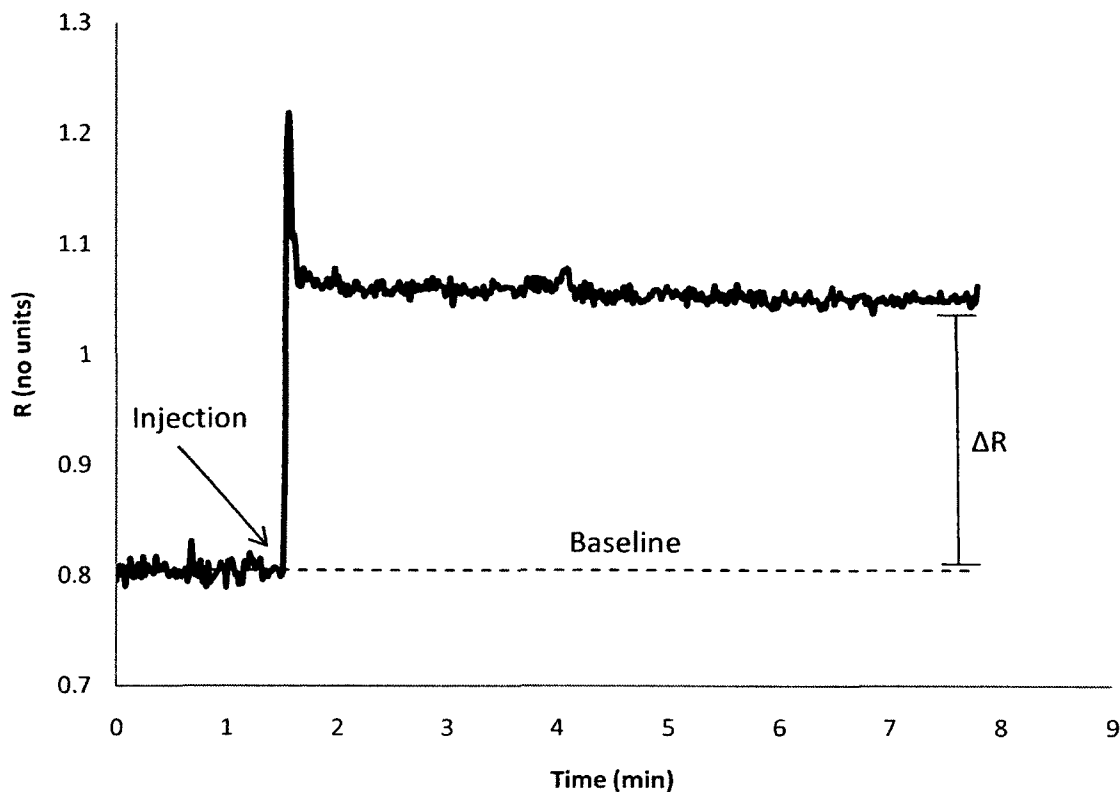
Figure 21. ΔR measured after the injection of nanoshells.

Nanoshells are more optically dense at 805 nm compared to 940 nm, and thus R will be seen to increase upon injection and decrease to the baseline as the particles are cleared from circulation.

After approximately 5 minutes of data collection, the last 30 second average meeting the previous stated criteria was used as R for the first time point. The probe was then removed and a 5 µL blood draw was then taken, analyzed with the spectrophotometer, and stored for later INAA analysis. Subsequent measurements via probe re-attachment and *ex vivo* blood analysis were taken from each animal at 2, 4, 6, 8, and 10 hours post injection.

4.1.5 Results

The baseline measurements of R taken before injection of nanoshells were examined and showed very little deviation from the average (0.7962 ± 0.0102). This indicated that blood oxygenation was stable for each animal under anesthesia and that minor changes in probe coupling to the animal's foot did not significantly influence the baseline measurement of R. Nanoshell OD measured by spectrophotometry, ΔR, standard deviation over the thirty second measurement, and AC magnitudes at both wavelengths were recorded for each measurement and can be seen in Table 3.

Table 3. Pulsatile data taken from five mice injected with nanoshells. Note that the gold content is given as μg as determined by INAA (described in section 4.2).

#	Mouse	BL R	NS Optical Density	R	ΔR	Gold (μg)	AC mag 805 (mV)	AC mag 940 (mV)	Std. Dev. (no units)	SNR 805 (dB)	SNR 940 (dB)
1	1	0.7864	6.4790	1.0247	0.2383	1.2950	14.2037	14.6989	0.0094	29.0686	29.3663
2	1	0.7864	4.6576	0.9687	0.1823	0.8837	13.1271	14.7802	0.0091	28.3840	29.4142
3	1	0.7864	3.3452	0.9397	0.1533	0.6761	23.3707	27.7407	0.0052	33.3940	34.8830
4	1	0.7864	2.3864	0.9344	0.1480	0.5143	15.9829	19.1766	0.0058	30.0937	31.6760
5	1	0.7864	2.0059	0.9048	0.1184	0.3545	14.3187	15.9537	0.0075	29.1387	30.0778
6	1	0.7864	1.3184	0.8708	0.0844	0.2383	10.8748	12.1744	0.0068	26.7490	27.7295
7	2	0.8051	6.5906	1.0499	0.2448	1.2765	21.0162	21.1664	0.0029	32.4717	32.5335
8	2	0.8051	4.8123	0.9788	0.1737	1.0404	13.5088	14.4816	0.0100	28.6329	29.2369
9	2	0.8051	3.5856	0.9648	0.1597	0.8031	12.3327	13.7555	0.0096	27.8418	28.7902
10	2	0.8051	2.6162	0.9342	0.1291	0.6111	14.5288	16.4509	0.0099	29.2652	30.3444
11	2	0.8051	1.8141	0.8709	0.0658	0.4278	18.3551	21.8225	0.0063	31.2957	32.7987
12	2	0.8051	1.0513	0.8704	0.0652	0.3067	15.5866	18.6132	0.0059	29.8757	31.4170
13	3	0.8047	7.0393	1.0552	0.2505	1.4633	12.8449	13.1730	0.0066	28.1952	28.4143
14	3	0.8047	5.3047	0.9783	0.1736	1.0930	25.6026	28.2136	0.0089	34.1863	35.0298
15	3	0.8047	3.6143	0.9521	0.1474	0.7765	24.7884	27.4974	0.0045	33.9056	34.8064
16	3	0.8047	3.2114	0.9213	0.1166	0.7022	27.3295	30.9729	0.0053	34.7532	35.8402
17	3	0.8047	2.5789	0.9156	0.1109	0.5402	23.0047	25.8163	0.0042	33.2569	34.2585
18	3	0.8047	2.0704	0.8967	0.0920	0.4533	21.2028	24.0598	0.0042	32.5485	33.6464
19	4	0.7841	5.3971	0.9954	0.2094	1.1226	7.2693	7.9928	0.0217	23.2504	24.0746
20	4	0.7841	4.4954	0.9605	0.1764	0.8916	7.8345	9.0031	0.0129	23.9008	25.1085
21	4	0.7841	3.9186	0.9268	0.1427	0.7551	26.3983	30.5952	0.0040	34.4521	35.7337
22	4	0.7841	2.7951	0.8975	0.1134	0.5709	11.3834	13.6458	0.0068	27.1461	28.7206
23	4	0.7841	1.9127	0.8478	0.0637	0.4416	14.8667	18.4704	0.0097	29.4649	31.3501
24	4	0.7841	1.4367	0.8372	0.0531	0.3401	13.0542	16.4422	0.0084	28.3356	30.3398
25	5	0.8005	5.6257	1.0659	0.2654	1.1244	13.2385	13.4806	0.0110	28.4574	28.6148
26	5	0.8005	3.8179	1.0008	0.2003	0.8052	9.7460	10.5955	0.0111	25.7971	26.5230
27	5	0.8005	2.9087	0.9519	0.1514	0.6347	9.6203	10.8233	0.0118	25.6844	26.7078
28	5	0.8005	2.6286	0.8458	0.0566	0.4889	16.3522	20.4360	0.0087	30.2921	32.2285
29	5	0.8005	1.7831	0.8703	0.0698	0.4126	14.4086	17.6588	0.0062	29.1930	30.9598
30	5	0.8005	1.6768	0.8467	0.0462	0.3231	13.1765	15.8136	0.0093	28.4166	30.0012

The signal to noise ratio (SNR) of the pulsatile signal at both wavelengths for

each measurement given in decibels (dB) was determined using the AC magnitude and

the inherent AC noise of the PP when the probe was attached to a non-pulsatile object

($500 \mu V_{p-p}$). The SNR corresponding to the minimum acceptable signal strength was 20

dB. This value was exceeded in all measurements.

$$SNR = 20 * \log\left(\frac{V_{AC_{p-p}}}{V_{noise_{p-p}}}\right)$$

A linear model of the optical density of the nanoshells in whole blood with

respect to ΔR was produced from the measurements taken from all animals. R statistical

software was used for all data analyses. The data showed a good linear fit with a non-

significant y-intercept ($y = 24.54x - 0.0085$, $R^2 = 0.8552$, $p = 2.875 \times 10^{-13}$). Confidence

(dashed lines) and prediction (dotted lines) intervals ($\alpha = 0.05$) were produced for the

model. The data lie within the prediction interval for all measured values of ΔR

indicating that the model could predict the range of future values of the nanoshells optical

density with 95% confidence (Figure 22).
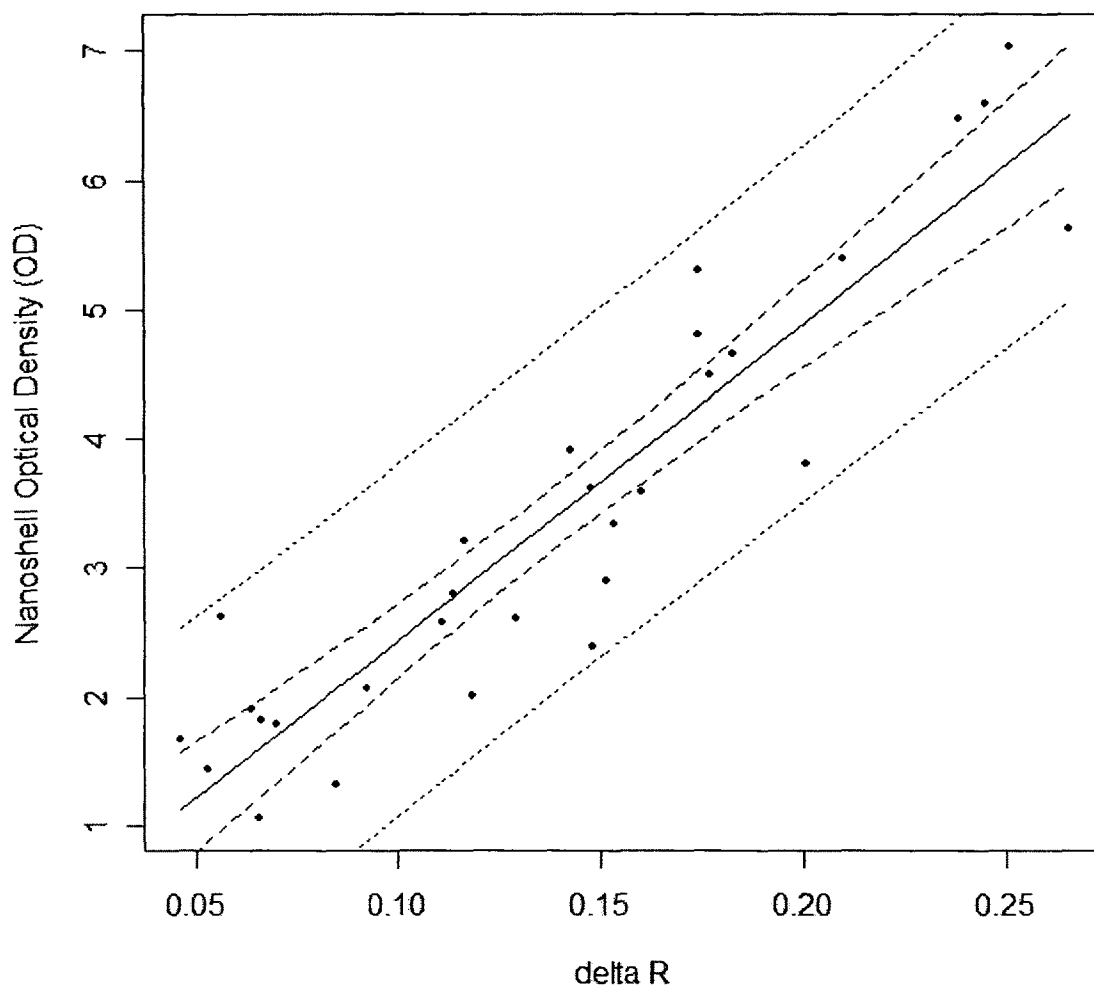
Figure 22. Linear model using ΔR to determine nanoshell concentration.

Leverage and influence point analysis was performed on the data set in order to detect potential outliers. A leverage point is a data point that is remote in the measured parameter (ΔR in this case). An influential data point is one that has noticeable impact on the parameters of the linear model. The data points showing evidence of high leverage and/or influence were then examined to see if they could be characterized by low signal magnitude or high standard deviation. The diagnostic statistics were performed using R statistical software with the help of a statistics text [103].

Leverage point analysis was performed by examination of the hat matrix computed from the single linear regression model. Bolded symbols are used to represent matrices. The hat matrix is defined as:

$$H = X(X'X)^{-1}X'$$

Where

$$X = \begin{pmatrix} 1 & x_{i,1} \\ \vdots & \vdots \\ 1 & x_{n,1} \end{pmatrix}$$

X is the matrix containing the values of ΔR for each measurement. The diagonal elements of H are the standardized distances of each observation from the center of the x space. Therefore, large values of H_{ii} (diagonal indices of the hat matrix) reveal observations that are possible outliers because of their remote location in the x space. The typical threshold for determining a possible leverage point is twice the average size of the values in the hat diagonal, 2p/n. The value of p is the rank of H and n is the number of observations. Possible outliers were identified as data points that had large H_{ii}'s and large residuals. These were identified using a standardized residuals versus fitted values plot as seen in Figure 23.
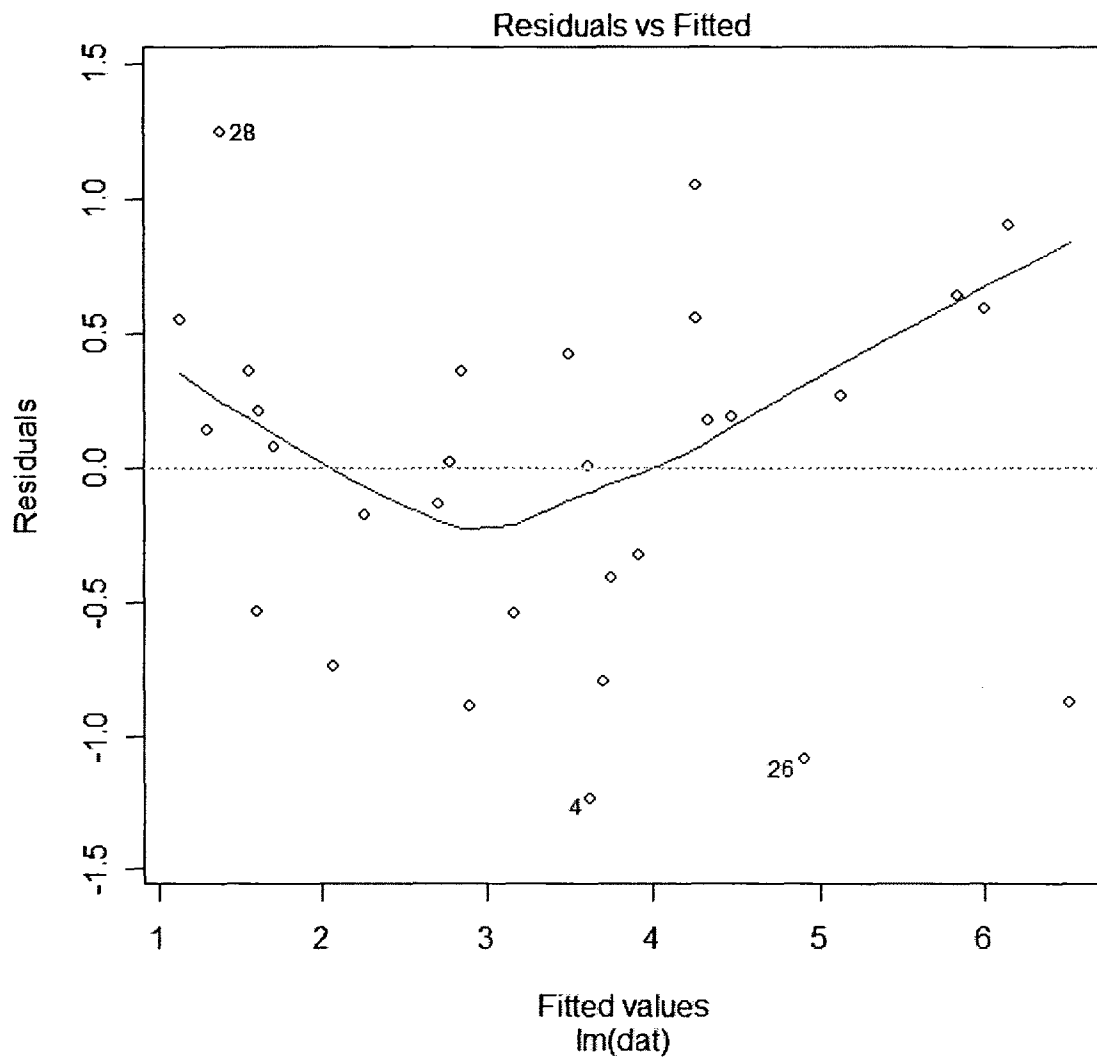
Figure 23. Standardized residuals versus the fitted values calculated using the linear model.

Points with high standardized residuals and leverage were considered possible outliers and their AC magnitude and standard deviation were examined for abnormalities. Influence analysis was performed by using three diagnostic statistics. These were the Cook's distance, DFFITS, and DFBETAS. All three parameters are deletion diagnostics, meaning that they measure the influence of the deletion of each data point on the sample

data set. Cook's distance describes not only how far each point is from the rest of the data set, but also how well the model fits each observation. Cook's distance is defined as

$$D_i = \frac{(\hat{y}_{(i)} - \hat{y})'(\hat{y}_{(i)} - \hat{y})}{pMS_{res}}$$

where $\hat{y}$ is the vector of fitted values (nanoshell optical density in this case) and $\hat{y}_{(i)}$ is the vector of fitted values after the omission of the ith observation. Therefore each measurement has an associated D_i. The rule of thumb for identifying influential data points is to compare each D_i to the F-statistic, $F_{(\alpha,p,n-p)}$, which is $F_{(0.5,2,28)} \cong 1$ in this analysis. Therefore, measurements having a large Cook's distance (>1) are considered influential data points. Cook's distance was determined for each data point in this set. No influential data points were identified using this regression diagnostic.

DFBETAS and DFFITS are two more deletion diagnostics used to measure the influence of single data points. DFBETAS is a measure of how the regression coefficients change, in units of standard deviation, when the ith measurement is deleted. DFBETAS is defined as

$$DFBETAS_{j,i} = \frac{\hat{\beta}_j - \hat{\beta}_{j(i)}}{\sqrt{S_{(i)}^2 C_{jj}}}$$

where $\hat{\beta}_j$ is the jth regression coefficient, $\hat{\beta}_{j(i)}$ is the jth regression coefficient computed after deletion of the ith data point, $S_{(i)}^2$ is the residual mean square after deletion of the ith data point, and C_{jj} is the jth diagonal element of $(X'X)^{-1}$. In this experiment, there are only two regression coefficients, the intercept and slope. The intercept was shown to be not significant, therefore only the DFBETA for the slope was analyzed. The suggested threshold for considering a data point as influential is $2/\sqrt{n}$, which is 0.3651 for a sample

size of thirty. |DFBETA| for the slope of the regression model was examined. Points 13, 25, and 28 in the data set were suspected influential points because their |DFBETA|'s exceeded the threshold.

DFFITS is used to assess the impact of the ith measurement on the fitted model, not just the regression coefficients. It is defined as

$$DFFITS_i = \frac{\hat{y}_i - \hat{y}_{(i)}}{\sqrt{S^2_{(i)} h_{ii}}}$$

where h_{ii} is the ith diagonal element of the hat matrix. This is a measurement of the amount that $\hat{y}_i$ changes if the ith data point is deleted and is given in units of standard deviation. The suggested threshold for detection of influential data points using |DFFITS| is $2\sqrt{p/n}$ or 0.5164. Again, points 13, 25, and 28 exceeded this threshold and were identified as potential influential data points.

Estimation of the effects of each data point on the precision of the model was performed by computing another diagnostic statistic called COVRATIO. This statistic helps to identify outliers by determining if each data point improves or degrades the precision of the model by its inclusion. It is therefore another deletion diagnostic. The statistic is defined as

$$COVRATIO_i = \frac{(S^2_{(i)})^p}{MS^p_{res}} \left(\frac{1}{1 - h_{ii}} \right)$$

Very low values of this statistic indicate that the data point in question may be an outlier. Very high values of this statistic indicate that the data point in question may be a leverage point unless it is an outlier in the y space (abnormal measurement of nanoshell optical density). The suggested upper and lower limits of this statistic are $1 + 3p/n$ and

$1 - 3p/n$. For this experiment, the upper and lower bounds can be described by

$1.2 > COVRATIO_i > 0.8$. The lower bound is only applicable in the case where $n > 3p$

(large sample size) which is true in this case. COVRATIO was calculated for each data

point. All of the data fall within the specified interval and therefore there was no

evidence that any of the data were outliers or influential points.

Data points 13, 25, and 28 were identified as potential influential measurements

by two of the four diagnostic statistics, but were not identified as leverage points by

examination the diagonal elements of the hat matrix. The AC magnitude and standard

deviation in the 30 second measurement of ΔR was examined for these three data points

to attempt to reveal abnormalities. All three points had AC magnitudes that exceeded the

set level for AC magnitude strength (5 mV). None of the three measurements had

excessive standard deviations above 0.03. Although these data points may have shown

signs of having a large effect on the linear model and were therefore potential outliers,

none their signal collection parameters were abnormal. It was concluded that there was

not enough evidence to identify these data points as outliers and were left in the data set.

Circulation half lives for each injected animal were produced by plotting the nanoshell

optical density and ΔR at each time point and using a single exponential decay function

as the model. This was done using both the nanoshell optical density as measured by

spectrophotometry and ΔR. These individual bioavailability curves can be seen in

APPENDIX D.

3.1.6 Discussion

The use of photoplethysmography in monitoring vascular nanoshell concentration in murine models was demonstrated. Analysis of the data reveals that the PP is capable of accurately measuring ΔR both immediately after injection of nanoshells and in subsequent measurements taken after probe reattachment. The lack of evidence of outliers or influential data points indicates that erroneous measurements of R made by the PP are not likely given that the probe is attached securely, vasodilation is induced, and core temperature are stabilized.

Errors in the estimates of R could be attributed to several factors. The measurement of arterial pulse is a difficult signal to extract from a small animal like a mouse. The distension of the blood vessels in the extremities is often quite small. This is an issue if significant motion artifact is present or if there is inherent noise in the circuitry. Also, under anesthesia, small animals often have difficulty maintaining their core temperature which will cause vasoconstriction and a reduction in peripheral blood flow. This will also deteriorate signal quality. These issues were dealt with by the immobilization of the animal and by the induction of slight hyperthermia. Secondly, although the foot of the animal is small and therefore it is possible to place the probe very close to the same anatomical location for each measurement, variables like optical coupling and probing volume cannot be perfectly controlled. It is possible that variation in the measurement of R could have been due to inconsistent optical coupling or optical shunting of light. Also, if there were slight changes in optical probing volume, the contribution of pulsatile tissue and venous blood may not have been negligible in each measurement. This could also have lead to variable measurements of R.

It is clearly evident that nanoshell concentration is directly related to ΔR. This experiment yielded an empirical linear model relating ΔR to nanoshell optical density which is proportional to concentration. The PP can therefore be calibrated to determine nanoshell optical density directly from ΔR. It was shown that signals with acceptable magnitude and stability, given by the high AC magnitude and low standard deviation for the 30 second data collection interval, could be obtained consistently.

4.2 Validation of Spectrophotometric Method with Instrumental Nuclear Activation Analysis (INAA)

Formal validation of the spectrophotometric method for determining nanoshell concentration in blood samples was performed. The processed blood samples from the previous experiment were transferred to INAA vials and labeled with the mouse number and time post injection. The vials were placed in a fume hood for drying. Standard samples prepared using nanoshell concentrations corresponding to whole blood nanoshell optical densities of 8, 4, and 0.8 OD were also prepared and dried as requested by the Texas A&M University Elemental Analysis Laboratory (TAMU-EAL). The samples were sent off for elemental analysis. The TAMU-EAL processed the samples and reported the gold content (μg) in each vial. This data was compared to the OD estimates using the spectrophotometric method. A linear model was produced to assess the correlation between the measurements (Figure 24).
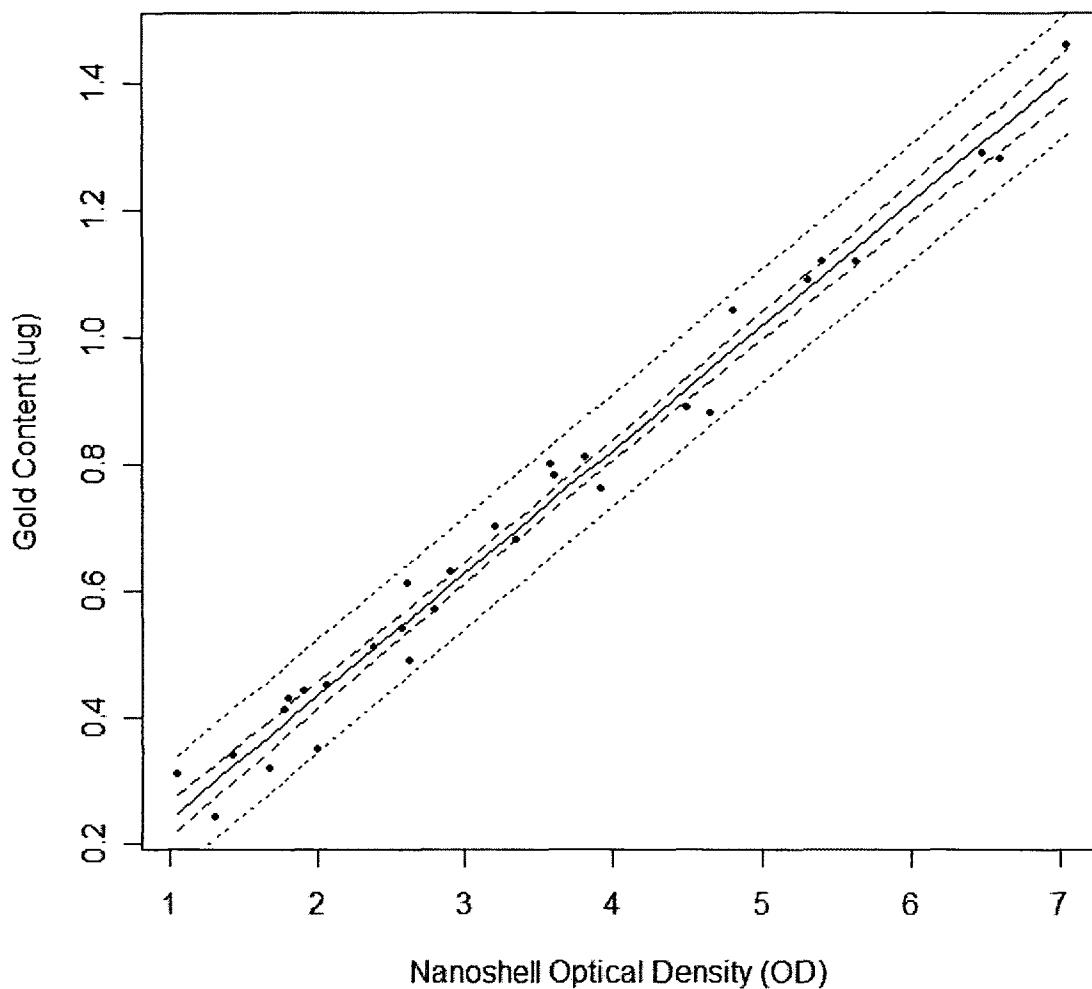
Figure 24. Linear model showing the correlation between nanoshell concentration using UV/Vis spectrophotometry and INAA (y = 0.0434x − 0.1948, R^2 = 0.9839 p = 2.2 x 10^{-16}).

The data shows excellent correlation between the two methods with a high value of R^2. The y-intercept produced by the linear fit was small and did not have significance comparable to that of the slope (p < 0.0223). The dashed and dotted lines show the confidence and prediction intervals for the model respectively using 95 % confidence. The confidence interval is very narrow indicating that the mean square of the residuals is very small suggesting that the model can be used to calculate the gold content in each sample with high accuracy. The data all lye within the 95 % predication interval

indicating that the model can be used to predict future values of gold content using the

measured value of nanoshell OD. Thus, the spectrophotometric method of nanoshell

concentration estimation was validated. The low-volume cuvettes (100 μL) used in

conjunction with a UV/VIS spectrophotometer employing a focused micro-beam design

made this possible. The data taken using the pulse photometer were compared to the

INAA estimates as well in order to confirm the correlation shown in Figure 22. This

correlation can be seen in Figure 25.
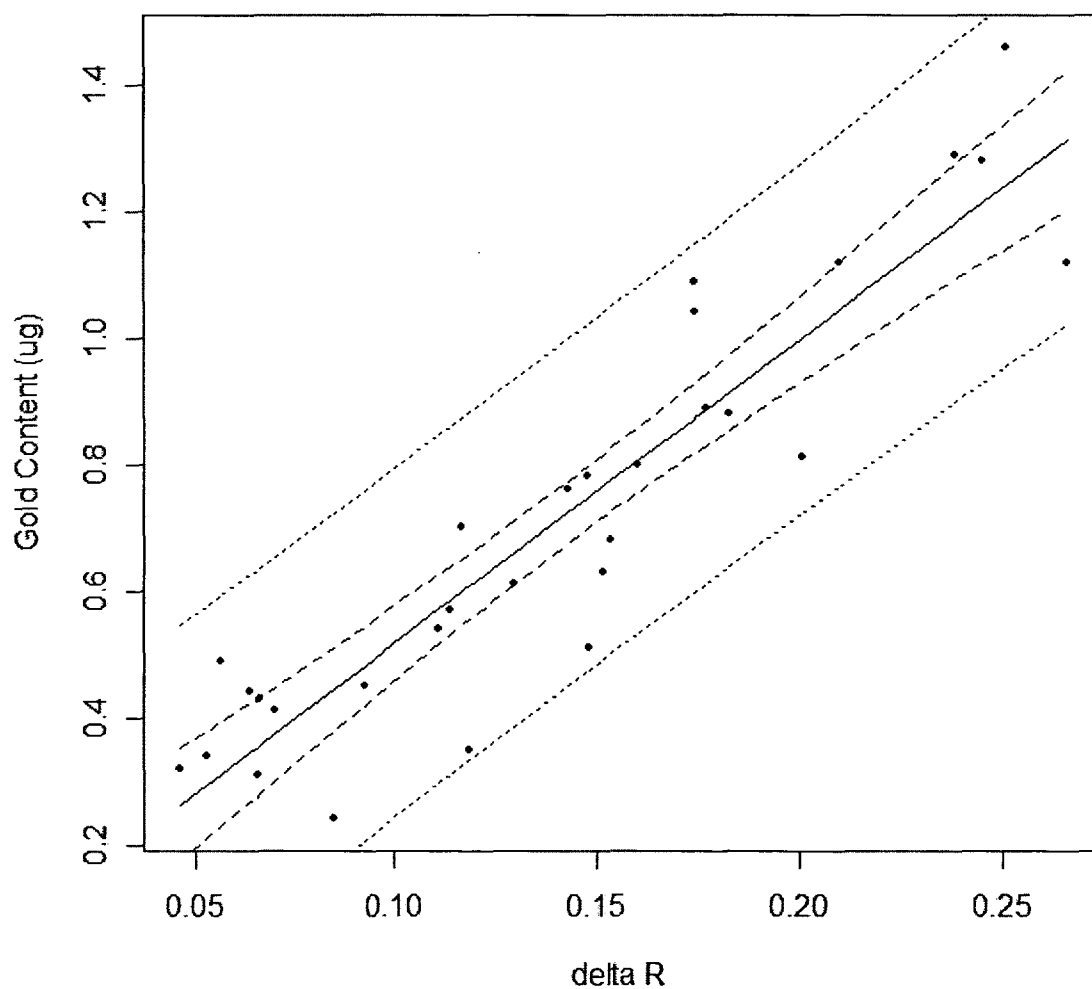
Figure 25. Linear correlation between ΔR measured using the pulse photometer and gold content measured using NAA (y = 4.7951x + 0.0396, R^2 = 0.8467, p = 6.38 x 10^{-13})

The model showed correlation approximately the same as that when comparing the INNA data with the UV/Vis data (R^2 of 0.8467) indicating a linear relationship. Regression diagnostics showed no evidence of outliers or influential data points. Thus confirmation of the pulse photometer measurements was achieved with INAA.

CHAPTER 5

DEVELOPMENT AND TESTING OF THE

PROTOTYPE III PULSE PHOTOMETER

The previous experiment demonstrated the feasibility of using pulse photometry to determine the concentration of gold nanoshells by empirical calibration. As effective as this was, prototype II could not determine absolute nanoshell optical density from R. This would be a major confounder in a clinical setting, since R is susceptible to changes in oxygen saturation. The improvements made to prototype II in order to achieve this were as follows.

- Addition of a third wavelength, 660 nm, which is a commonly used oximeter wavelength, enabling the pulse photometer to gain more information about the arterial blood oxygen saturation.

- Addition of equations using Beer's law in LabVIEW to determine nanoparticle optical density and arterial oxygen saturation simultaneously.

In order to demonstrate the effectiveness of this new prototype, termed prototype III, a nanoparticle with a sharper extinction band in the NIR was used. The nanoparticles chosen were NIR extinguishing gold nanorods, which have similar characteristics as gold nanoshells and are used in many of the same applications. Gold nanorods have a strong extinction band in the NIR like gold nanoshells. However, their geometry causes them to extinguish light at 805 nm much more so than 940 nm or 660 nm. This is advantageous

because the change in R is dependent on the preferential extinction of light at one wavelength over another.

In order to estimate the nanorod optical density and SpO_2 in whole blood, optical properties of the oxygenated and reduced whole blood and nanorods must be known. These were estimated using the extinction spectrum of the nanorods, and calibration of the pulse photometer using blood draws from animals injected with nanorods and an empirical calibration curve. The procedure for determining the optical properties of blood and nanorods is described in the materials and methods section.

The capability of the pulse photometer as a pulse oximeter is also demonstrated in a single mouse after the device had been calibrated. A leg probe was constructed using a clip purchased from Starr Life Sciences and was fitted with the same four-wavelength LED as the foot/tail probe and another low cost photodiode with comparable performance parameters to that used in the foot/tail probe. A site-by-site analysis was performed to determine the best probing site on a mouse determined by pulsatile signal strength and stability. The foot, tail, and leg were each examined using their respective probes on a mouse in consecutive measurements where the probes were attached, removed, and re-attached. Example PPG's from each probe location can be seen in APPENDIX E. Simultaneous estimation of SpO_2 and nanorod optical density after injection is demonstrated in five mice after the site-by-site analysis.

5.1 Materials and Methods

5.1.1 Optical Properties of
Gold Nanorods

PEG modified gold nanorods with a longitudinal dimension of approximately 45

nm and a transverse dimension of approximately 15 nm were obtained from Nanospectra

Biosciences. The extinction spectrum of the nanorods was determined by

spectrophotometry. A 1% nanorod solution diluted in 10% Triton X having a volume of

100 μL was prepared and scanned in a micro cuvette to simulate the measurement of the

diluted blood draws. The optical densities of the nanorods were 0.2517, 0.7144, and

0.1442 at 660, 805, and 940 nm respectively. These corresponded to 25.17, 71.44, and

14.42 optical density in the stock solution. The optical densities of the nanorods were

59.62 % at 805 nm and 15.09 % at 940 nm of the optical density of the nanoshells used in

the experiments described in Chapter 4. This illustrates a nanoparticle batch that was

significantly less optically dense could still be monitored in this experiment. A

normalized extinction spectrum of these nanorods in comparison to the gold nanoshells

can be seen in Figure 26.
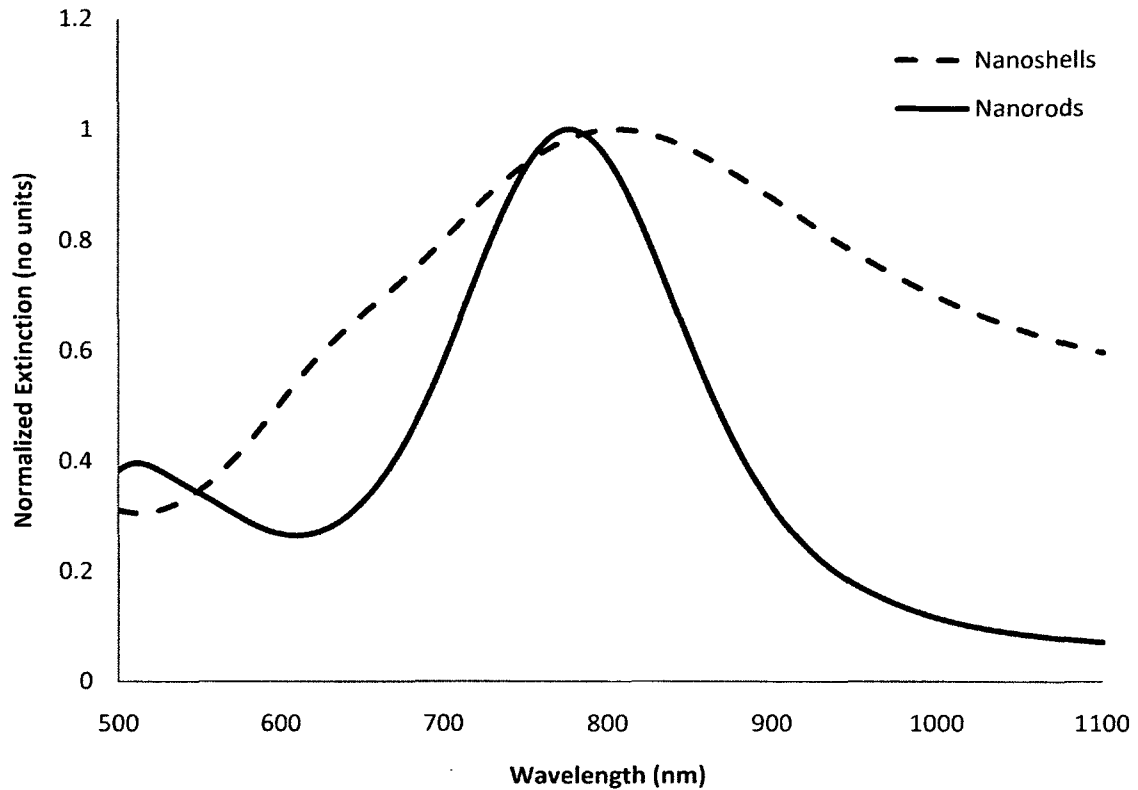
Figure 26. Overlay of the normalized extinction spectra of the long circulating gold nanoshells from 3.4 and the gold nanorods monitored with the prototype III pulse photometer. Note the sharper extinction band with a peak near 780 nm.

5.1.2 Estimation of the Attenuation Properties of Whole Blood

The optical density changes caused by the pulsation of blood are different depending on the interrogation wavelength. These changes are due to the characteristic optical attenuation coefficients of individual components of whole blood. In a simplified model, these are oxygenated and reduced whole blood. In the case when optically active nanoparticles are introduced to the circulating blood, there will also be the contribution of their optical attenuation. As mentioned previously, the optical properties of whole blood have been measured at several wavelengths in previous experiments. Nonetheless, many

of these experiments were done *ex vivo* and may not be accurate for *in vivo* measurements.

The first step to obtain information on the attenuation properties of whole blood in the mouse model was to control the blood oxygenation in order to measure the attenuation coefficients of fully oxygenated blood. This was done using five BALB/c mice. The mice were anesthetized with the isoflurane setup described previously and a catheter was inserted into the tail vein. This set their blood oxygenation to approximately 100% and allowed for controlled infusion of nanoparticles into the tail vein. Their core temperature was also maintained at approximately 40 °C in order to induce vasodilation. The pulse photometer was then attached to the foot and signal quality was assessed using the pulse amplitude and standard deviation over thirty second periods as previously described. Once signal stability was achieved, injections of nanorods were then delivered at the same dose as typical nanoshell injections (4.5μl/g). The ΔR using the ratio of ΔA's at 805 and 940 nm was measured and recorded. Once this value had stabilized, again assessed by pulse amplitude and standard deviation, this value was recorded and a 5 μL blood draw was then taken and processed and analyzed with UV/Vis spectrophotometry as described previously to determine the optical density of the nanorods in the circulating blood at 805 nm.

Beer's law was used to determine the attenuation coefficients of oxygenated whole blood at the three wavelengths by using the measured nanorod optical density.

$$R_{805/940} = \frac{0.8\mu_{HbO_2}^{940} + \mu_{NR}^{805}}{\mu_{HbO_2}^{940} + 0.2018\mu_{NR}^{805}}$$

$$\mu_{HbO_2}^{805} = 0.8\mu_{HbO_2}^{940}$$

$$\mu_{HbO_2}^{660} = 0.5\mu_{HbO_2}^{940}$$

$$\mu_{NR}^{940} = 0.2018\mu_{NR}^{805}$$

In these equations, $\mu_{HbO_2}^{660}$, $\mu_{HbO_2}^{805}$, and $\mu_{HbO_2}^{940}$ are the effective attenuation coefficients of oxygenated whole blood at 660, 805, and 940 nm respectively. The term attenuation is used because these terms include the effects of absorption, scattering, and typical hematocrit, which is assumed to be constant for each measurement. μ_{NR}^{805} is the optical density of the nanorods at 805 nm as measured by spectrophotometry. The bottom half of the first equation contains the term $0.2018\mu_{NR}^{805}$ since the measured extinction spectrum of nanorods revealed that the ratio of the optical densities at 940 nm and 805 nm was 0.2018. Therefore, it was assumed that this ratio also was maintained when the nanorods were detected with the pulse photometer. The effective attenuation coefficient of oxygenated whole blood at 805 nm was approximated by $\mu_{HbO_2}^{805} = 0.8\mu_{HbO_2}^{940}$ since $R_{805/940}$ had a typical value of approximately 0.8, as shown previously using pulse photometry during oxygen delivery. The effective attenuation coefficient of oxygenated whole blood at 660 nm was approximated as $\mu_{HbO_2}^{660} = 0.5\mu_{HbO_2}^{940}$ by using an empirical calibration curve given by Webster.[33] This calibration curve reported that the ratio of ΔA's at 660 and 940 nm, $R_{660/940}$, was approximately 0.5 when SpO_2 was equal to 100%.

Five BALB/c mice were anesthetized with the isoflurane/oxygen delivery system and injected with the typical volume of nanorods (4.5 µL/g) while being monitored with the pulse photometer. A blood draw was taken approximately 5 minutes after the injection and analyzed using spectrophotometry. The nanorod optical density in whole blood in each mouse was determined. This value was then inserted into the equation for

$R_{805/940}$ at 100% oxygen saturation and values of $\mu_{HbO_2}^{660}$, $\mu_{HbO_2}^{805}$, and $\mu_{HbO_2}^{940}$ were obtained. The five estimates of the effective attenuation coefficients for each wavelength were then averaged and used in subsequent measurements. These estimates of the attenuation coefficient of oxygenated whole blood can be seen in Table 4.

Table 4. Semi-empirically derived effective attenuation coefficients of oxygenated whole blood determined with nanorod injections

Mouse	$\mu_{HbO_2}^{660}$ (cm^{-1})	$\mu_{HbO_2}^{805}$ (cm^{-1})	$\mu_{HbO_2}^{940}$ (cm^{-1})
1	2.0519	3.2830	4.1038
2	1.5935	2.5496	3.1871
3	1.2356	1.977	2.4712
4	2.0382	3.2611	4.0764
5	2.3056	3.6889	4.6112
Average	1.8450	2.9519	3.6899
Standard Deviation	0.4263	0.6820	0.8526

Next, in order to be able to determine SpO_2 as well as nanoparticle concentration, the attenuation coefficients of reduced whole blood needed to be approximated. Since measuring fully reduced whole blood *in vivo* was not possible, approximations of the optical properties of reduced whole blood were obtained from the literature. Since reduced whole blood also contains both absorbing and scattering components, values for the absorption and scattering coefficients were obtained and used to determine the attenuation coefficients at the three wavelengths used in the pulse photometer measurements.

The molar absorption coefficients of reduced hemoglobin were first obtained from

Prahl [31]. A typical hemoglobin concentration value of 2.303 mM was used to then

determine the absorption coefficient of reduced whole blood. Next, the scattering

coefficients and anisotropy of reduced whole blood were estimated using spectral data

from a previous report [59]. The effective attenuation coefficients, μ_{eff}^{λ}'s, at 660, 805,

and 940 nm were then calculated using an equation for the effective attenuation

coefficient in dense scattering biological media obtained from Welch and van Gemert

[104].

$$\mu_{eff}^{\lambda} = \sqrt{3(\mu_{a_{Hb_r}}^{\lambda})(\mu_{a_{Hb_r}}^{\lambda} + (1 - g)\mu_{s_{Hb_r}}^{\lambda})}$$

$\mu_{a_{Hb_r}}^{\lambda}$ and $\mu_{s_{Hb_r}}^{\lambda}$ are the absorption and scattering coefficients of reduced whole

blood and g is the anisotropy at the wavelengths used in the pulse photometer. The

anisotropy is a parameter that describes the degree of forward scattering that occurs when

light passes through that particular medium. It can be defined as the cosine of the mean

scattering angle which will approach 1 if a medium is entirely forward scattering. Blood

is a primarily forward scattering medium and therefore has rather high anisotropy (> 0.99

at the wavelengths of interest). $(1 - g)$ is multiplied by the scattering coefficient in

order to account for the effects of forward scattering. This makes the reduced scattering

coefficient, $\mu_{s_{Hb_r}}'$, which is defined as $(1 - g)\mu_{s_{Hb_r}}^{\lambda}$ and determines the attenuation of

light due to scattering, much smaller since forward scattered photons can still be detected.

These calculated values were then adjusted by referring to the calibration curve for SpO_2

with respect to R given in Webster [33]. This calibration curve can be seen in Figure 27.
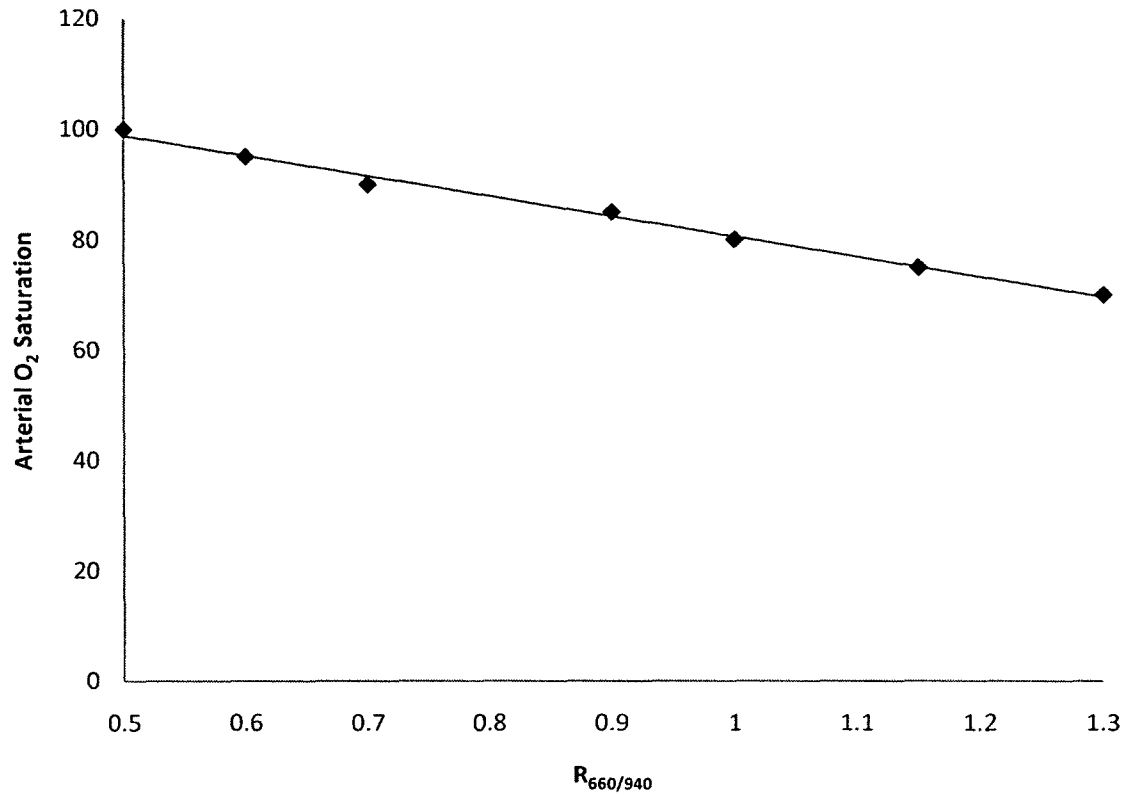
Figure 27. Empirical calibration curve developed using a linear model (SpO$_2$ = -36.589R + 117.15, R^2 = 0.9931) derived from point measurements in a calibration curve found in Webster [33].

Beer's law was used to determine the empirical attenuation coefficients of

reduced blood by using R at six different oxygen saturation percentages.

$$R_{660/940} = \frac{S\left(\mu_{HbO_2}^{660}\right) + (1 - S)\left(\mu_{Hb_r}^{660}\right)}{S\left(\mu_{HbO_2}^{940}\right) + (1 - S)\left(0.2404\mu_{Hb_r}^{660}\right)}$$

$$\mu_{Hb_r}^{940} = 0.2404\mu_{Hb_r}^{660}$$

$$\mu_{Hb_r}^{805} = 0.2540\mu_{Hb_r}^{660}$$

$\mu_{HbO_2}^{660}$ is the attenuation coefficient of oxygenated whole blood found previously

and S is the oxygen saturation at a particular value of R given by the calibration curve.

$\mu_{Hb_r}^{660}$, $\mu_{Hb_r}^{805}$, and $\mu_{Hb_r}^{940}$ are the effective attenuation coefficients of reduced whole blood. $0.2404\mu_{Hb_r}^{660}$ and $0.2540\mu_{Hb_r}^{660}$ were used as $\mu_{Hb_r}^{940}$ and $\mu_{Hb_r}^{805}$ respectively in order to keep the ratios of the attenuation coefficients the same as those calculated using the literature. The six calculated values for $\mu_{Hb_r}^{660}$, $\mu_{Hb_r}^{805}$, and $\mu_{Hb_r}^{940}$ were then averaged to obtain the attenuation coefficients used to estimate the nanorod optical density and SpO$_2$ in subsequent experiments. The optical properties of reduced whole blood from both the literature and after adjustment can be seen in Table 5 and Table 6.

Table 5. Optical properties of reduced whole blood obtained from the literature.

Wavelength	$\mu_{a_{Hbr}}$ (cm^{-1})	$\mu_{s_{Hbr}}$ (cm^{-1})	g	$\mu'_{s_{Hbr}}$ (cm^{-1})	$\mu_{eff_{Hbr}}$ (cm^{-1})
660	17.2809	318	0.9950	1.5900	31.2781
805	3.9295	235	0.9939	1.4241	7.9442
940	3.7139	183	0.9926	1.3615	7.5199

Table 6. Effective attenuation coefficients of reduced whole blood using the literature derived values and the calibration curve in Figure 27.

SpO$_2$ (%)	R$_{660/940}$	$\mu_{Hb_r}^{660}$ (cm^{-1})	$\mu_{Hb_r}^{805}$ (cm^{-1})	$\mu_{Hb_r}^{940}$ (cm^{-1})
95	0.6	8.1869	2.0795	1.9681
90	0.7	7.9820	2.0274	1.9189
85	0.9	10.6766	2.7119	2.5667
80	1	9.7163	2.4679	2.3358
75	1.15	10.0209	2.5453	2.4090
70	1.3	9.9436	2.5257	2.3904
Average	-	9.4210	2.3930	2.2648
S. D.	-	1.0854	0.2757	0.2609

The average values for the effective attenuation coefficients were used to solve

for the nanorod optical density and SpO$_2$ in the following set of simultaneous equations:

$$R_{805/940} = \frac{S\left(\mu_{HbO_2}^{805}\right) + (1 - S)\left(\mu_{Hb_r}^{805}\right) + \mu_{NR}}{S\left(\mu_{HbO_2}^{940}\right) + (1 - S)\left(\mu_{Hb_r}^{940}\right) + 0.2018 OD_{NR}}$$

$$R_{660/940} = \frac{S\left(\mu_{HbO_2}^{660}\right) + (1 - S)\left(\mu_{Hb_r}^{660}\right) + 0.3523\mu_{NR}}{S\left(\mu_{HbO_2}^{940}\right) + (1 - S)\left(\mu_{Hb_r}^{940}\right) + 0.2018\mu_{NR}}$$

A simultaneous equation solver was added to the pulse photometer LabVIEW

software which calculates the SpO$_2$ and nanorod optical density using average values of

R as specified by the user.

5.1.3 Demonstrating Pulse
Oximetry with the Prototype
III Pulse Photometer

To assess the ability of the prototype III pulse photometer to measure SpO_2, a

pilot study was conducted using a mouse undergoing cycles of hypoxemia. This was

achieved by using the ketamine/xylazine cocktail described previously. In prior use of

the cocktail with mice, it was observed that severe hypoxemia, as measured using

standard pulse oximetry (ADInstruments PowerLab) and observed by visual inspection of

the color of the tail arteries, is induced if the animal is breathing ambient air. It was

suspected that this is an undesirable side effect of the xylazine, which is a very potent

analgesic and sedative according to Dr. Orchard. Rapid re-oxygenation of the blood

could be achieved using the oxygen concentrator used in the isoflurane delivery setup.

This was exploited in order to modulate the oxygen saturation in the mouse.

A BALB/c mouse was anesthetized using the cocktail given at the same dose as

previously described. The heating pad was again used to maintain slight hyperthermia to

increase pulse amplitude. The pulse photometer was attached to the foot of the animal

and probe placement was confirmed by satisfactory pulse amplitude and standard

deviation of $R_{660/940}$ over 30 seconds. Oxygen was delivered to the animal at a flow rate

of 1 L/min using the oxygen concentrator. Three periods of hypoxemia lasting

approximately two minutes were induced by removing the oxygen source from the

animal. The pulse photometer collected the $R_{805/940}$ data during both oxygen delivery

and removal, which was used to determine oxygen saturation. Oxygen saturation was

estimated using the theoretical model omitting the contribution of nanorods and with the

calibration curve given in Figure 27. The calibration curve was estimated as a linear

model using six values of oxygen saturation and their corresponding oxygen saturations between 70 % and 100 %. Figure 28 and Figure 29 show the SpO$_2$ calculations using the theoretical and empirical methods.
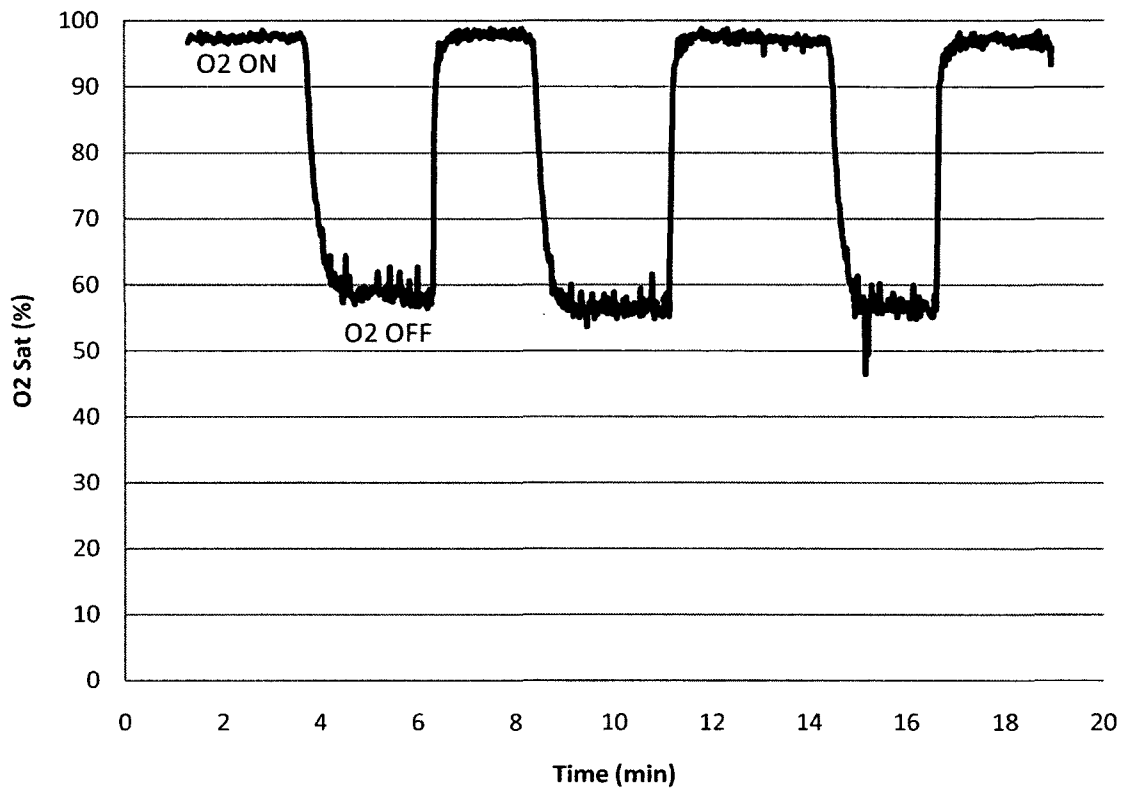
Figure 28. Oxygen saturation calculated using theoretical model. Periods of normoxia were achieved with the delivery of oxygen and periods of hypoxemia were achieved with the removal of the oxygen.
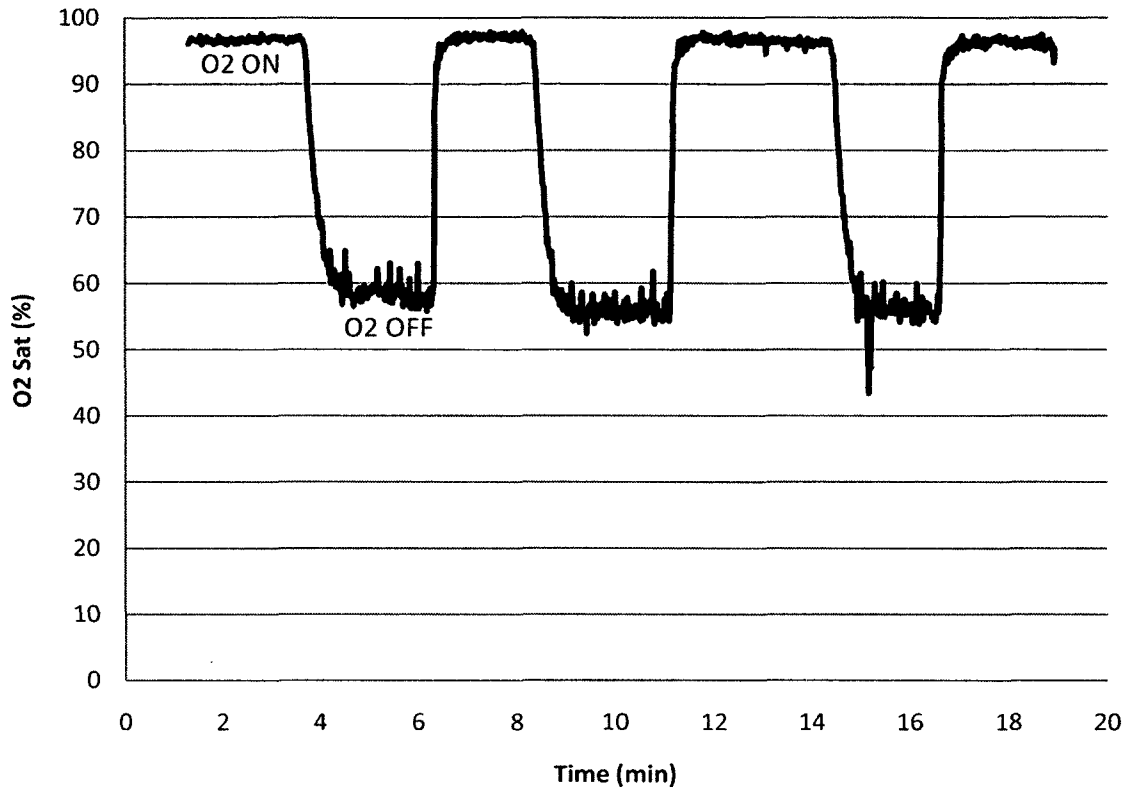
Figure 29. Oxygen saturation calculated using empirical calibration. Note the agreement with the theoretical model.

The data from both methods were compared and the average difference between SpO$_2$ measurements was 0.5825 % ± 0.2472 during the entire experiment. The average SpO$_2$ during four one minute segments of oxygenation was 97.4086 % ± 0.3052 for the theoretical calculation and 96.7126 % ± 0.2559 for the empirical calculation. During hypoxemia, three one minute segments were averaged yielding SpO$_2$ estimates of 57.4381 % ± 1.3761 and 56.9912 % ± 1.6147 for the theoretical and empirical methods. The measurements using both algorithms showed good agreement with low bias during both normoxia and hypoxemia. Although the calibration curve was constructed using values between 70 % and 100 % oxygenation and therefore SpO$_2$ measurements below

70 % are extrapolated, both algorithms determined similar estimates during hypoxemia.

It was therefore determined that the pulse photometer was sensitive to oxygen saturation

and could be used as an oximeter in the murine model.

5.1.4 Site-by-Site Analysis to Determine Optimal Probe Placement

Several anatomical locations were investigated as optimal transmission probe

placement sites. This was assessed in a study where three probe locations were examined

using two probes designed to interface with the murine anatomy. One of the probes was

the foot/tail probe previously described and the other was a leg probe that could be

clamped to the thigh of the mouse after hair removal. A BALB/c mouse with a mass of

32 g was anesthetized using the isoflurane delivery system and mild hyperthermia was

induced with the heating pad. The left leg of the animal was shaved using a set of

clippers. The three probing locations chosen were the foot, leg, and tail. For each site,

the probe was attached and removed five times to assess measurement reproducibility and

pulse quality. The reproducibility was determined by the mean and standard deviation of

the SpO_2 (95-100 %) and nanorod optical density (~0) measured during five 30 second

intervals. Pulse quality was determined by the SNR of the pulsatile signal. These data

can be seen in Table 7.

Table 7. Tabulated signal parameters using data from each probe site.

Location	SpO$_2$	μ_{NR}	SD R$_{805/940}$	% R$_{805/940}$	SD R$_{660/940}$	% R$_{660/940}$	SNR 805	SNR 940	SNR 660
Foot	0.9878	0.0721	0.0085	1.038691	0.0066	1.239886	30.74378	32.38646	26.8666
	0.978	-0.019	0.0129	1.614221	0.0205	3.736614	27.32921	29.17276	24.00168
	0.9806	-0.0457	0.0091	1.148149	0.0108	1.996816	33.56745	35.64142	29.98604
	0.9831	0.0366	0.0149	1.837193	0.0104	1.923817	31.28527	32.38646	26.8666
	0.9818	-0.0073	0.0074	0.923638	0.006	1.109909	34.22365	36.11382	30.65967
Average	0.98226	0.00734					31.42987	33.14018	27.67612
S.D.	0.003623	0.046828							
Leg	0.9213	0.1781	0.0289	3.384051	0.0229	3.306577	29.14855	30.46608	27.29702
	0.9035	0.0872	0.0277	3.312624	0.034	4.65719	23.55188	25.15549	22.45087
	0.9073	0.2486	0.0298	3.414502	0.022	3.014339	26.95206	27.82788	25.51636
	0.9168	0.2363	0.0175	2.015934	0.0184	2.604358	25.42289	26.70916	23.62772
	0.9406	0.2059	0.0131	1.528888	0.0162	2.496744	28.73152	30.07472	26.33366
Average	0.9179	0.19122					26.76138	28.04667	25.04513
S.D.	0.014558	0.064289							
Tail	0.9612	0.089	0.006	0.725891	0.0118	1.986301	32.89271	34.57487	29.96842
	0.9631	-0.0056	0.015	1.864317	0.0079	1.353273	34.34442	36.17907	31.48526
	0.9558	-0.0861	0.008	1.016347	0.0101	1.695869	33.5108	35.54564	30.9486
	0.9597	0.0069	0.0093	1.150957	0.0092	1.553346	31.48896	33.23209	28.67476
	0.9788	-0.1338	0.0158	2.045339	0.021	3.893438	32.56533	34.65977	29.36576
Average	0.96372	-0.02592					32.96044	34.83829	30.08856
S.D.	0.008846	0.08654							

Average SNR was highest when probing the tail, probably because this placement probes the tail arteries. However, SpO$_2$ was highest and had the lowest standard deviation when the probe was placed on the foot. The measurement of nanorod optical density was also the closest to zero. Measurements taken from the leg showed the largest variability and lowest SNR. This was probably because of the added pressure placed on the tissue by the leg probe which could irritate the animal causing excess movement and because of the non-homogenous tissue at this location. From the data it was determined

that the optimal probe location was the foot due to the demonstration of reproducible measurement and high SNR.

5.1.5 Animal Experiments

The accuracy of the pulse photometer in measuring vascular nanorod concentration was tested using five BALB/c mice. The mice were anesthetized using the same protocol as described previously. The pulse photometer was then attached to the animal and allowed to collect data at all three wavelengths. Once signal stability was obtained, an injection of nanorods from the batch used for calibrating the pulse photometer was given via tail vein catheter at a dose of 4.5 μL/g. An observable change in $R_{805/940}$ and $R_{660/940}$ resulted from each injection and an initial estimate of nanorod optical density and SpO_2 was obtained after 2-5 minutes. An example of the typical change in $R_{805/940}$ and $R_{660/940}$ can be seen in Figure 30.
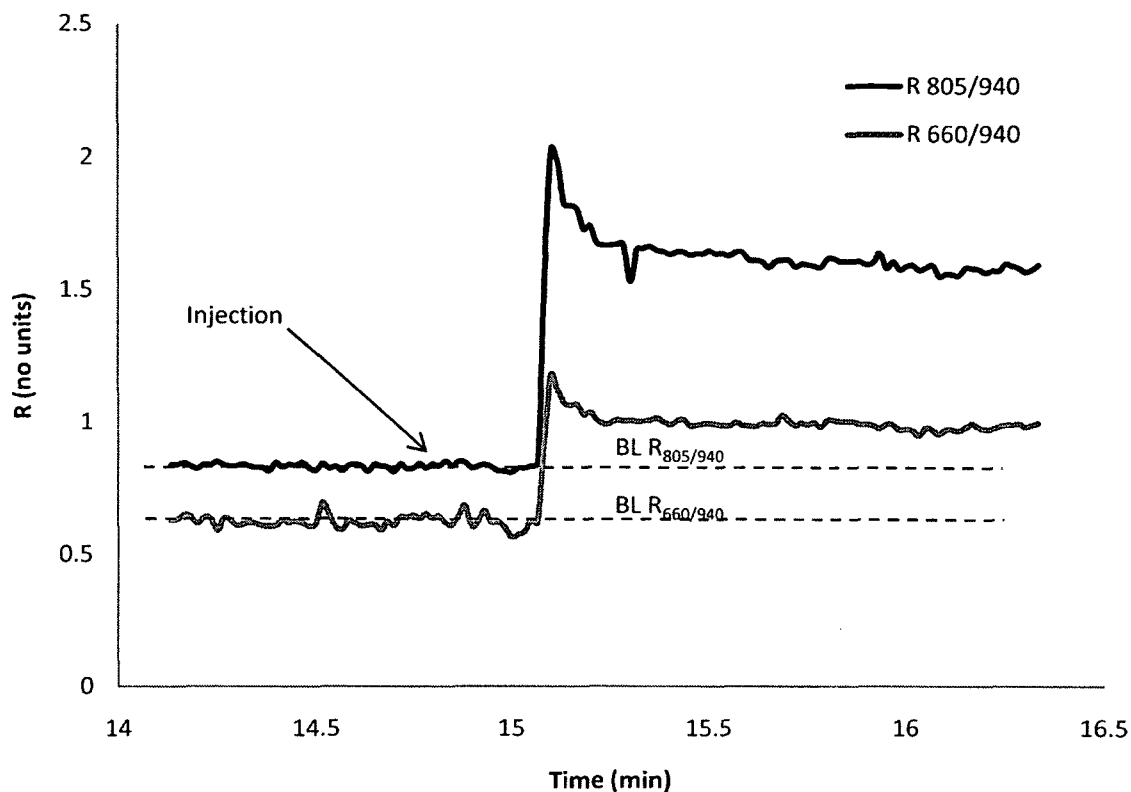
Figure 30. Changes in $R_{805/940}$ and $R_{660/940}$ resulting from the injection of gold nanorods.

A 5 μL blood draw was then taken, processed, and analyzed with UV/Vis spectrophotometry as described previously. Subsequent measurements were taken at various time points for up to four hours. The mice were allowed to fully recover from anesthesia between each measurement.

5.2 Results

Estimates of nanorod optical density were obtained using both the pulse photometer and UV/Vis spectrophotometry. The correlation between these measurements was assessed using a linear model presented in Figure 31. The agreement

between the two methods was assessed using a Bland-Altman analysis as described

previously. This can be seen in Figure 32.
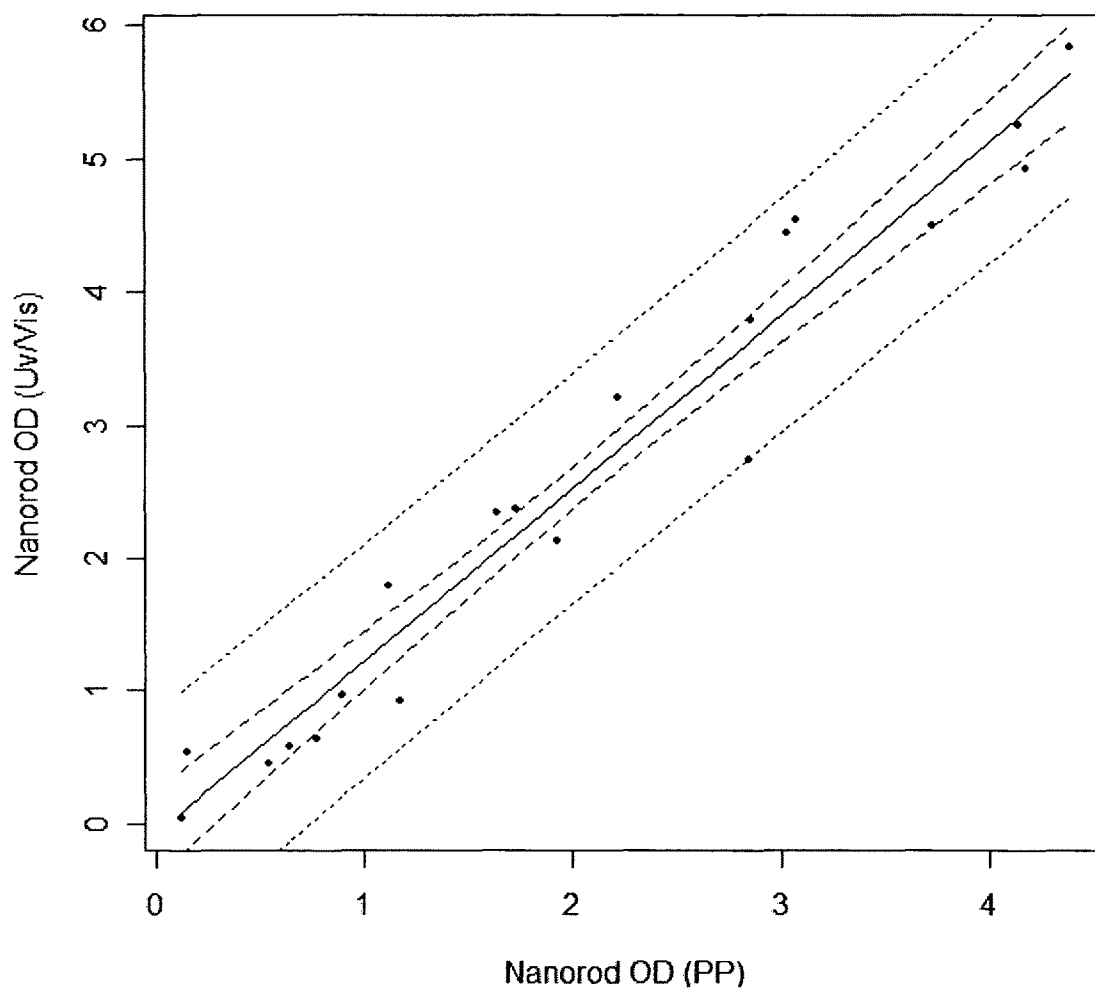
Figure 31. Linear model showing the correlation between nanorod optical density measured by pulse photometry and UV/Vis spectrophotometry.
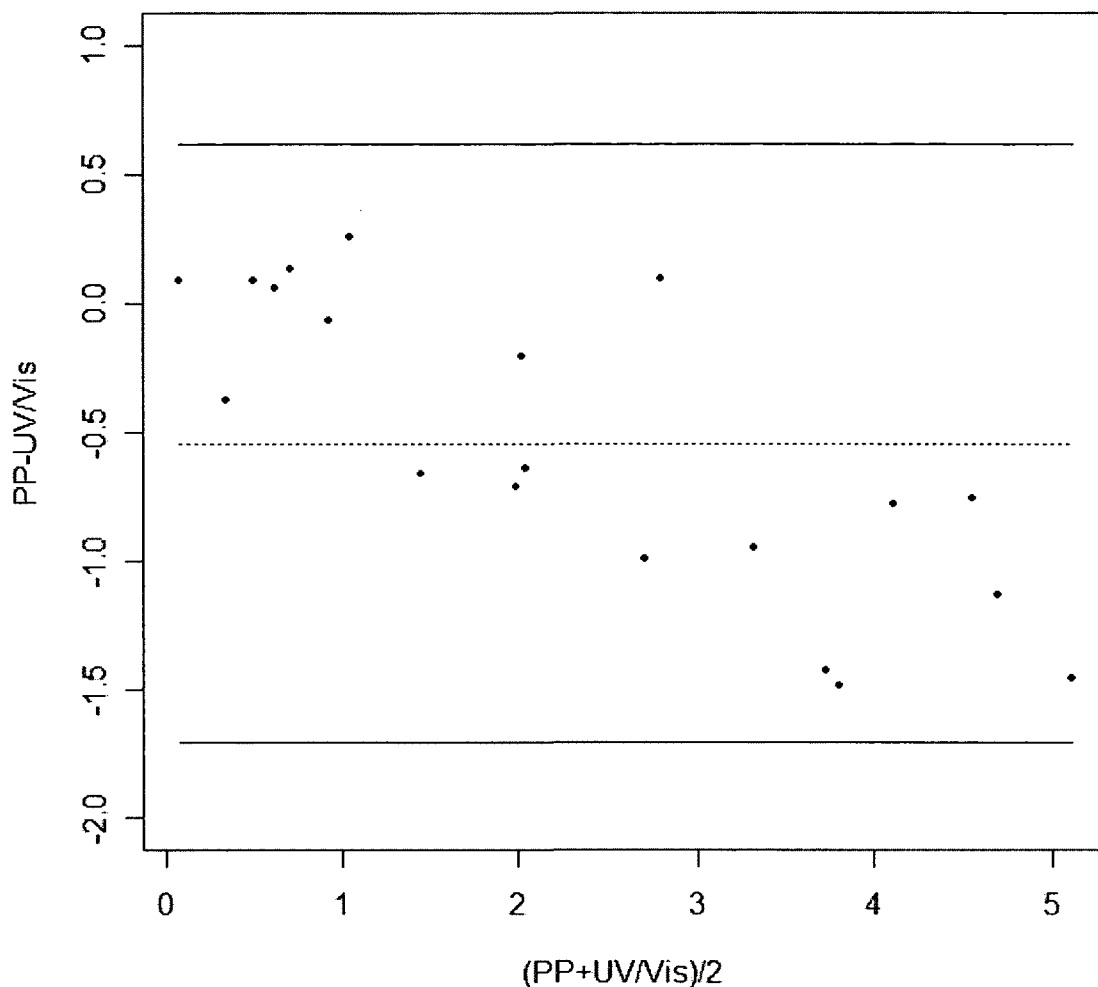
Figure 32. Bland-Altman plot showing the bias and precision of nanorod optical density measurement.

The linear model showed good correlation between the measurements using the pulse photometer and UV/Vis spectrophotometry with a high coefficient of determination ($R^2 = 0.9544$). The model also showed that the pulse photometer improved the accuracy as compared to the prototype 1 photometer. The measurements in this experiment tended to only slightly underestimate the nanorod optical density (y = 1.3036x − 0.0781, p = 1.62 x 10^{-13}). The small y-intercept also indicated that the pulse photometer should measure zero nanorod optical density when no nanorods were present, indicating lack of an

artificial offset in the measurements. The 95% confidence (dashed line) and prediction (dotted line) intervals were calculated. All of the data were within the 95% prediction interval indicating that the pulse photometer could accurately estimate nanorod optical density in future measurements. The Bland-Altman plots also suggest improved accuracy in measuring nanorod optical density. The linear model showed a low bias of -0.5455 OD, an improvement of 69.61% compared to bias demonstrated with the prototype I photometer. Bland-Altman analysis revealed a precision of $\pm$ 1.1591 OD indicating a 61.25% improvement in the precision of the measurements as compared to the prototype I photometer.

The ability of the pulse photometer to accurately measure oxygen saturation concurrent to nanorod optical density was semi-quantitatively assessed. Since there was no method to verify oxygen saturation, quality in SpO_2 measurement was assessed by examining how close the measurements tended to be to normal physiological oxygen saturation (95-100%). SpO_2 was calculated concurrent to each measurement of nanorod optical density using the three wavelength calculation described previously. These data can be seen in Figure 33.
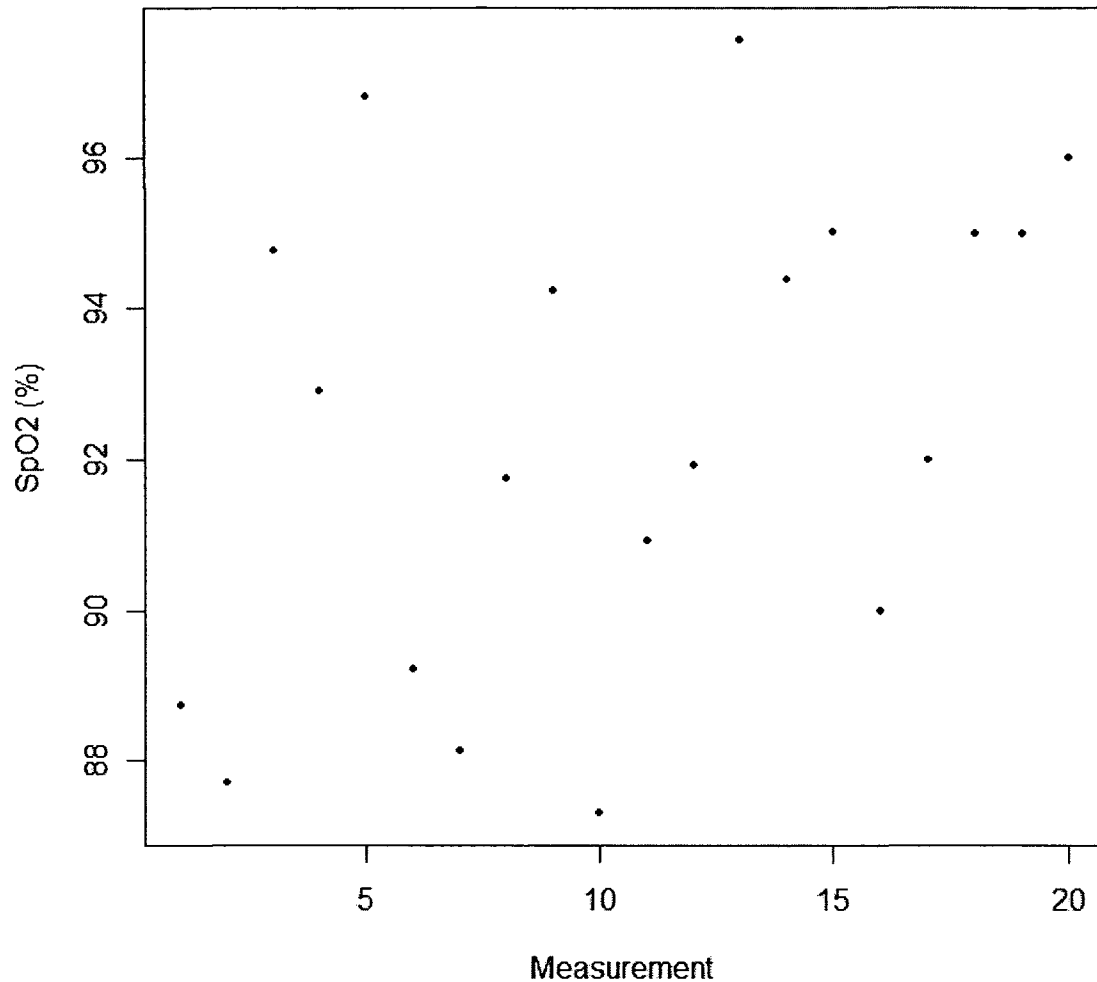
Figure 33. Oxygen saturation measured by pulse photometry concurrent to nanorod optical density measurement.

The average estimate of oxygen saturation for all measurements was 92.464 ± 3.172%. This suggests that the pulse photometer tended to underestimate oxygen saturation in the presence of nanorods. This is assumed because the mice were connected to the oxygen concentrator. This effect was more dramatic at higher measured nanorod optical densities. However, the technique did show good reproducibility indicated by the small standard deviation and did not indicate severe hypoxemia with the average measurement well above 90%.

5.3 Discussion

The use of three wavelength pulse photometry has shown to accurately measure the optical density of nanorods in the circulating blood in murine models. The technique also shows promise in concurrent monitoring of arterial blood oxygen saturation. Errors in calculating the nanorod optical density could be accounted for by the fact that the attenuation coefficients for HbO_2 and HbR at the three wavelengths used by the pulse photometer are averages of semi-empirically derived values. These could vary from animal to animal with changes in hematocrit, a variable that is crucial in determining the scattering coefficient of whole blood. Intermittent decreases in oxygen saturation could also be the source of these errors. Issues relating to the optics of the pulse photometer could also have caused errors. For example, the foot of the mouse was found to be the optimal probing location based on the study explained in the site-by-site analysis. However, it is possible that in such a small probing volume, optical shunting could occur. This is due to light at any wavelength passing through the probing volume without interacting with the arterial blood. This would affect the measurement of ΔA at any wavelength and may have been more dramatic at the longer wavelengths since it was reported that the effective attenuation coefficients are smaller at 810 nm and 950 nm than at 650 nm [104]. These are all close to the wavelengths used in the experiment. Lastly, the extinction spectrum of the nanorods was determined prior to injection into the animals by dilution of the stock into DI water and scanning the UV/Vis spectrophotometer. The contribution of the optical density at 660 nm and 940 nm was modeled by a fraction of that at 805 nm, close to the peak optical density of the nanorods. This may not have been true after the nanorods were injected into the animal, subjecting

them to blood plasma and changing the local refractive index. This may shift the peak extinction wavelength causing the contribution of the optical densities at 660 nm and 940 nm to be different than measured prior to injection with spectrophotometry. The assumption of the stock solution optical densities was also only based on accounting for dilution. It is well known that Beer's law does not behave well in extremely optically dense media and may not have accurately modeled the extinction of light in the animal at each wavelength correctly. This would definitely lead to errors in measurement of nanorod optical density and may also account for the artificially low SpO_2 readings indicating that the extinction of light may have been more prevalent at 660 nm than assumed in the model. Evidence of this is also shown by the more dramatic decrease in SpO_2 at higher concentrations of nanorod optical density.

As a side point of discussion, the gold nanorods used in this experiment did not display the same circulation half lives as expected from a clinically applicable batch. Typical PEG coated gold nanorods have been reported to circulate for many hours. This batch showed much faster clearance from the blood stream with half lives ranging from 106 to 30 minutes as measured by spectrophotometry. This may have been due to deterioration of the PEG coatings over the shelf life of the particles. This was suggested by the fact that the manufacturing date on the vial of the particles was April 24, 2009, and these experiments were performed during March 2010. Nevertheless, this did not affect the concentration estimates and did not appear to cause aggregation of the particles before or after injection as observed with spectrophotometry.

Regardless of the limitations of the pulse photometer and the Beer's law model, it has been shown that vascular nanorod optical density can be monitored concurrent to SpO_2

calculation. Vast improvements have been made to the device since the first prototype photometer leading to increased precision and accuracy.

CHAPTER 6

CONCLUSIONS AND FUTURE WORK

This dissertation has presented the development of a medical instrument capable

of providing quality control in nanoparticle therapy and has been shown to be compatible

with two classes of optically active metal nanoparticles. Real-time *in vivo* determination

of vascular nanoparticle concentration is essential in optimizing therapy since patient

reactions to nanoparticles are often variable and difficult to quantify using conventional

invasive techniques. The reaction to nanoparticles is also important to monitor because it

affects the efficacy of the treatment, and optimal circulation time is critical in target

tissue accumulation. Thus, a powerful tool in optimizing nanoparticle treatments has

been presented.

This report summarizes the development of three prototypes of this device, each

design having significant advantages over the previous. In testing the prototype I

photometer, it was shown that injection of standard doses of optically extinguishing gold

nanoshells could be detected using NIR light, which was a significant finding. This

proved that non-invasive optical monitoring was indeed feasible and warranted further

investigation. The prototype II pulse photometer demonstrated that monitoring of long

circulating NIR extinguishing nanoparticles could be achieved by adapting the principles

of dual-wavelength photoplethysmography, the same technique used in pulse oximetry.

This allowed for the monitoring of only vascular concentration of nanoparticles and point

measurements taken by attachment, removal, and reattachment of the device. These were the two main improvements in the prototype II pulse photometer and presented significant advances in the technology. The prototype III pulse photometer made use of multi-wavelength measurements to demonstrate feasibility of the measurement of oxygen saturation concurrent to vascular nanoparticle monitoring. It employed a model based on Beer's law accounting for the contribution of HbO_2, HbR, and gold nanorods, which could be displayed in real time. Excellent improvement in determining nanoparticle concentration was demonstrated compared to the prototype I photometer as well as the addition of SpO_2 calculation. It was able to not only give an absolute measurement of nanorod optical density, but could also be taken on and off just like the prototype II device. This allowed for long time monitoring which is essential for effective nanoparticle treatments. In summary, a novel and completely non-invasive optical technique has been developed, which is compatible with a variety of optically active nanoparticles and is capable of providing real time feedback critical in effective nanoparticle therapy.

This dissertation has also presented a new and effective *ex vivo* spectrophotometric blood analysis technique capable of replacing expensive and often time consuming conventional methods. The technique of using low volume cuvettes to examine the spectral characteristics of processed blood samples using focused beam UV/Vis spectrophotometry was validated in this report. The technique showed excellent correlation to an industry standard method, nuclear activation analysis, eliminating the need to rely on this expensive and time consuming analysis technique to validate measurements in future experiments.

Although several designs of the pulse photometer have been built and tested, there are several future improvements that can be made. In order for this instrument to clinically applicable, it must be modified to be compatible with standard power supplies (110-120 V_{p-p} @ 60 Hz) and must have signal processing algorithms built in using either a microcontroller or a standardized software program. In its current state, the user interface is achieved using a LabVIEW front panel and the signal processing is achieved using pre-programmed LabVIEW VI's. This design could be "locked down" using the creation of a standalone program which is not reprogrammable without a version of LabVIEW, but can be executed on any computer meeting the minimum system requirements, even if it does not have LabVIEW installed. This would expand the use of the pulse photometer to off site locations and would not require expensive software, but would still require the use of a data acquisition card. Currently, the use of this device requires a level of technical knowledge about the instrumentation and murine physiology, which is a hurdle to the development of almost any medical instrument. The production of standard operating protocols developed through experience using the pulse photometer will hopefully help to train operators not familiar with the finer details of the operation of the instrument to use it effectively. This is an issue currently being addressed. Improvements in the instrumentation and algorithms could also be made in future designs. Currently, LED's and a photodiode are used in the emission and detection of light transmitted through the tissue. The incorporation of lasers could prove advantageous since these sources are less polychromatic than LED's making the application of a single point measurements of tissue/blood optical properties more accurate. However, the issue of coupling these light sources to murine tissue is not trivial

and would require novel design of the optics used to accomplish this. The use of reflectance photoplethysmography has not been investigated, but could prove to an avenue for expanding the realm of possible probing locations. This was a design improvement made in many recent developments of PPG based instruments described in the literature review. Multi-wavelength PPG is another subject that has only recently been explored in the latest prototype III pulse photometer. The use of multiple wavelengths in conjunction with more sophisticated algorithms could improve the performance of the device. Perhaps Beer's law may be an over simplified approximation of light propagation in pulsatile tissue which would warrant a more rigorous theoretical approach. Delivery of multiple wavelengths could allow for the analysis of more optically attenuating species in bulk tissue and improve the robustness of the instrument. This device has not been tested on humans receiving experimental nanoparticle treatments. The pulse photometer has demonstrated murine compatibility and uses a non-invasive optical technique to give feedback in these nanoparticle therapies. Human use of this device is of course the ultimate goal and is an exciting and possible application in the near future.

APPENDIX A

THE USE OF THE BEER-LAMBERT LAW

IN PHOTOPLETHYSMOGRAPHY

Beer's law states that the intensity of light transmitted through a medium is dependent on the concentration of the absorbing species in the medium. A very small change in intensity of light traveling in the x-direction can be expressed as a function of characteristics of the optical medium.

$$dI = -(\beta I c)dx$$

β is a proportionality constant, I is the intensity of the light incident at the location $x = 0$, and c is the concentration. The negative sign implies that the transmitted light is less intense than the incident light, which is intuitive. A schematic of light traveling through an attenuating medium can be seen in Figure 34.
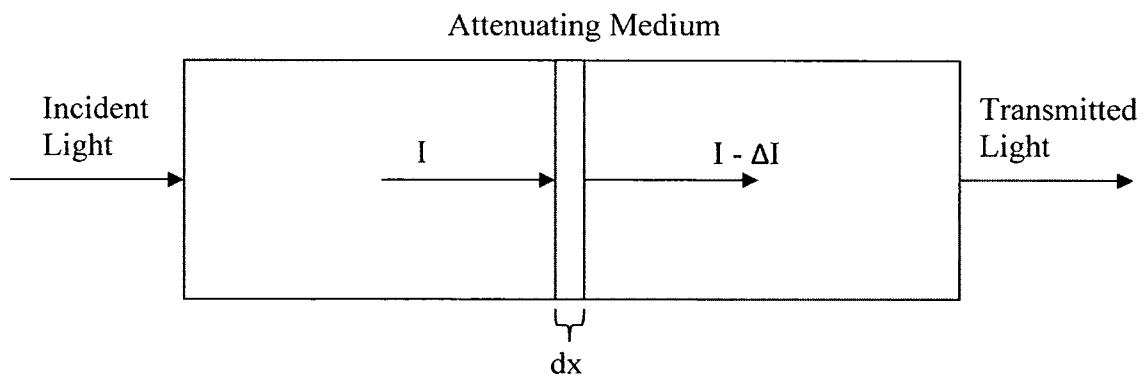
Figure 34. Change in light intensity as it travels through an attenuating medium.

If both sides of the equation are integrated, we can obtain the intensity of light as a function of its linear position.

$$\int_{I_0}^{I} \frac{dI}{I} = -\beta c \int_{0}^{d} dx$$

$$\ln \frac{I_0}{I} = \beta c d$$

$$I = I_0 e^{-\beta c d}$$

We define extinction, A, using the linear relationship between the logarithm of the ratio of the incident intensity and transmitted intensity.

$$A = \log \frac{I_0}{I} = \frac{\beta c d}{\ln 10}$$

$$\frac{\beta}{\ln 10} = \varepsilon$$

$$A = \varepsilon c d$$

ε is the molar extinction coefficient with units of $M^{-1} cm^{-1}$.

If a medium contains more than one extinguishing species, the effects of each species can be modeled as additive and depend on their characteristic extinction coefficients. A medium with n extinguishing species can be modeled by the summation of the effects of each species for one wavelength.

$$A = \left(\sum_{i=0}^{n} \varepsilon_i c_i \right) d$$

If a medium is pulsatile, changes in the optical path length result in changes in extinction. This is the case for the pulsing blood in the body. The primary absorbing species in blood is hemoglobin. In the case where there are no dyshemoglobinemias, hemoglobin can take the form of either oxy-hemoglobin (HbO) or reduced hemoglobin (Hb). During a pulse from the heart, small changes in the blood fraction caused by

arterial distension in distal areas of the body like the fingers and toes cause a small

change in transmitted light resulting in a small change in extinction. The small change in

extinction, ΔA, can be accounted for by the concentration of hemoglobin, the molar

extinction coefficients of HbO and HbR, and the degree of oxygen saturation, S.

$$\Delta A = (S\varepsilon_{HbO}c_{Hb} + (1 - S)\varepsilon_{HbR}c_{Hb})\Delta d$$

ΔA can be measured using a photodiode that converts the intensity of light into

current. If this is connected to a current to voltage amplifier, the resulting voltages are

proportional to the intensity of the detected light. ΔA can therefore be determined using

the change in voltage due to an arterial pulse.

$$\Delta A = \log\left(\frac{1}{1 - \Delta I}\right) = \log\left(\frac{I_{DC}}{I_{DC} - I_{AC}}\right) = \log\left(\frac{V_{DC}}{V_{DC} - V_{AC}}\right)$$

V_{DC} is the non-pulsitle voltage and V_{AC} is the peak to peak magnitude of the

pulsitle voltage. If V_{AC} is very small compared to V_{DC}, then ΔA can be approximated

using the ratio of the AC voltage to the DC voltage.

$$\Delta A = \log\left(\frac{V_{DC}}{V_{DC} - V_{AC}}\right) \sim \frac{V_{AC}}{V_{DC}}$$

The model using the molar extinction coefficients of HbO and HbR does not

account for light scattering by blood cells. We can use the modified effective attenuation

coefficient to account for the scattering in both oxygenated and reduce whole blood.

$$\mu^{\lambda}_{eff_{Hb}} = \sqrt{3(\mu^{\lambda}_{a_{HbR}})(\mu^{\lambda}_{a_{HbR}} + (1 - g_{HbR})\mu^{\lambda}_{s_{HbR}})}$$

$$\mu^{\lambda}_{eff_{Hbo}} = \sqrt{3(\mu^{\lambda}_{a_{Hbo}})(\mu^{\lambda}_{a_{Hbo}} + (1 - g_{Hbo})\mu^{\lambda}_{S_{Hbo}})}$$

$$\mu^{\lambda}_{a_{HbR}} = \varepsilon_{a_{HbR}} c_{Hb}$$

$$\mu^{\lambda}_{a_{Hbo}} = \varepsilon_{a_{Hbo}} c_{Hb}$$

$$\mu^{\lambda}_{S_{HbR}} = \varepsilon_{S_{HbR}} c_{Hb}$$

$$\mu^{\lambda}_{S_{HbR}} = \varepsilon_{a_{Hbo}} c_{Hb}$$

The μ^{λ}_{eff} of both oxygenated and reduced whole blood can be calculated from the absorption (μ_a's) and scattering coefficients (μ_s's) and using the anisotropy (g's). The oxygenation of the blood can then be found by using the ratio of ΔA's at two wavelengths.

$$\frac{\Delta A_{\lambda 1}}{\Delta A_{\lambda 2}} = R$$

$$S = \frac{\mu^{\lambda 1}_{eff_{HbR}} - R\mu^{\lambda 2}_{eff_{HbR}}}{R(\mu^{\lambda 2}_{eff_{Hbo}} - \mu^{\lambda 2}_{eff_{HbR}}) - \mu^{\lambda 1}_{eff_{Hbo}} + \mu^{\lambda 1}_{eff_{HbR}}}$$

The thickness change, Δd, is eliminated because it is assumed equal for both wavelengths. Upon addition of an exogenous optically extinguishing species (assume nanoparticles), its optical density can be added as a variable in the equations and can be found with simultaneous oxygen saturation calculation if at least three wavelengths are used.

$$\Delta A_{\lambda 1} = (S\mu^{\lambda 1}_{eff_{Hbo}} + (1 - S)\mu^{\lambda 1}_{eff_{HbR}} + \mu^{\lambda 1}_{NP})\Delta d$$

$$\Delta A_{\lambda 2} = (S\mu_{effHbo}^{\lambda 2} + (1 - S)\mu_{effHbR}^{\lambda 2} + \mu_{NP}^{\lambda 2})\Delta d$$

$$\Delta A_{\lambda 3} = (S\mu_{effHbo}^{\lambda 3} + (1 - S)\mu_{effHbR}^{\lambda 3} + \mu_{NP}^{\lambda 3})\Delta d$$

The nanoparticles will have different optical densities depending on the wavelength which is determined by its extinction spectrum. In the case of the nanorods, the maximal optical density is at 805 nm. The optical densities at 940 nm and 660 nm were 20.18 % and 35.23 % of the optical density at 805 nm respectively. Therefore, nanorod optical density in each equation can be expressed as fractions of one term.

$$\mu_{NR}^{940} = 0.2018\mu_{NR}^{805}$$

$$\mu_{NR}^{660} = 0.3523\mu_{NR}^{805}$$

If the ratios of the ΔA's at 805/940 nm and 660/940 nm are used, two equations with two unknowns are obtained and can be solved using linear algebra. These unknowns are the oxygen saturation, S, given in units of % and the nanorod optical density, μ_{NR}, given in units of cm^{-1}. This can be shown in matrix form.

$$R_1 = \frac{\Delta A_{805}}{\Delta A_{940}}$$

$$R_2 = \frac{\Delta A_{660}}{\Delta A_{940}}$$

$$AX = Y$$

$$A = \begin{bmatrix} R_1(\mu_{effHbo}^{940} - \mu_{effHbR}^{940}) - (\mu_{effHbo}^{805} - \mu_{effHbR}^{805}) & 0.2018 - 1 \\ R_2(\mu_{effHbo}^{940} - \mu_{effHbR}^{940}) - (\mu_{effHbo}^{660} - \mu_{effHbR}^{660}) & 0.2018 - 0.3523 \end{bmatrix}$$

$$Y = \begin{bmatrix} (\mu_{eff_{HbR}}^{805} - R_1\mu_{eff_{HbR}}^{940}) \\ (\mu_{eff_{HbR}}^{660} - R_2\mu_{eff_{HbR}}^{940}) \end{bmatrix}$$

$$X = \begin{bmatrix} S \\ \mu_{NR} \end{bmatrix}$$

$$X = A^{-1}Y$$

APPENDIX B

DETAILED SCHEMATIC OF LIGHT EXTINCTION

IN PULSITLE TISSUE

This section gives a schematic description of the change in the pulsatile signals resulting from arterial blood upon addition of optically absorbing nanoparticles shown in Figure 35 and Figure 36. The purpose is to clarify for the reader the preferential attenuation of certain wavelengths based on the extinction spectrum of the nanoparticles.
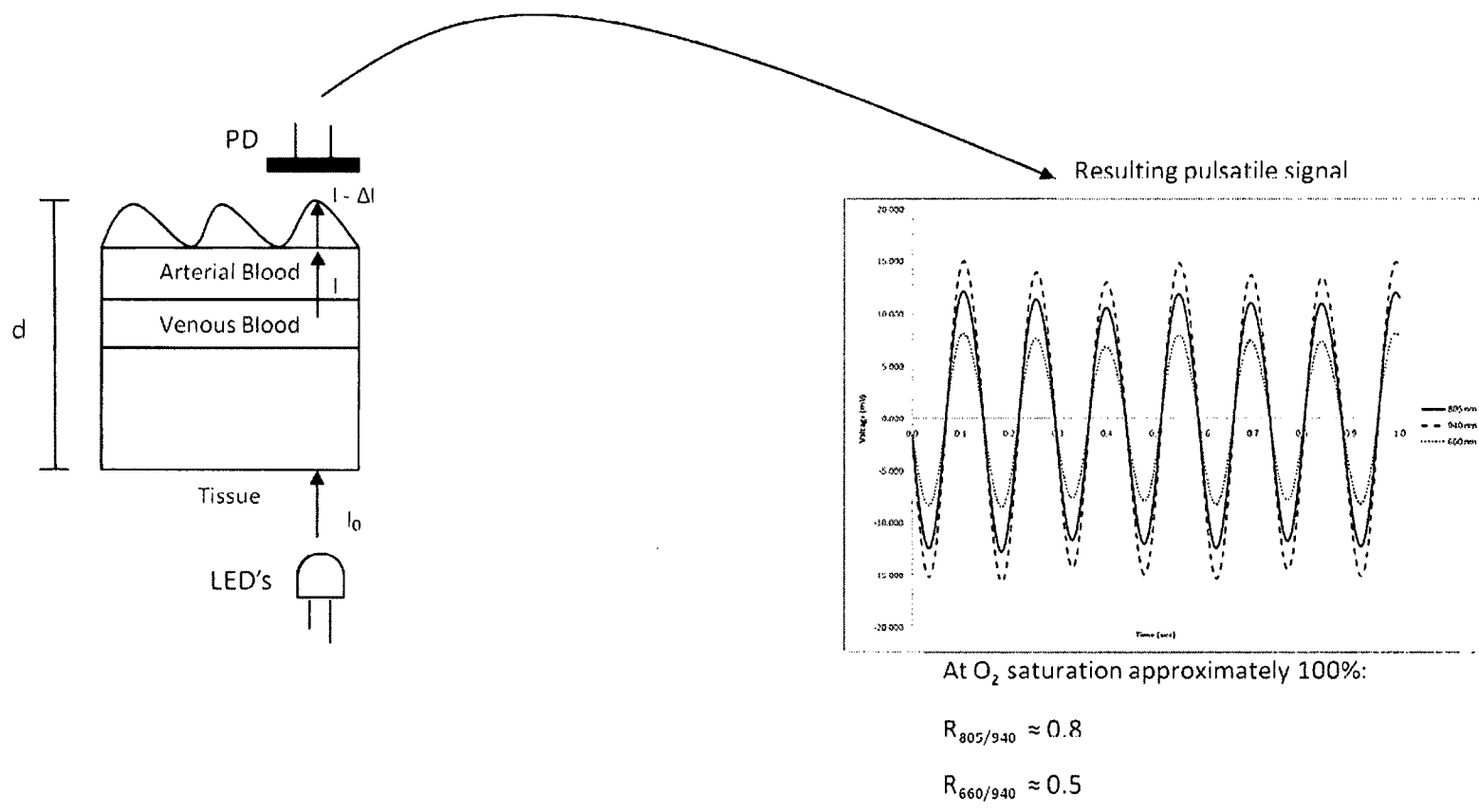
Figure 35. Pulsatile changes in transmitted light in oxygenated arterial blood.
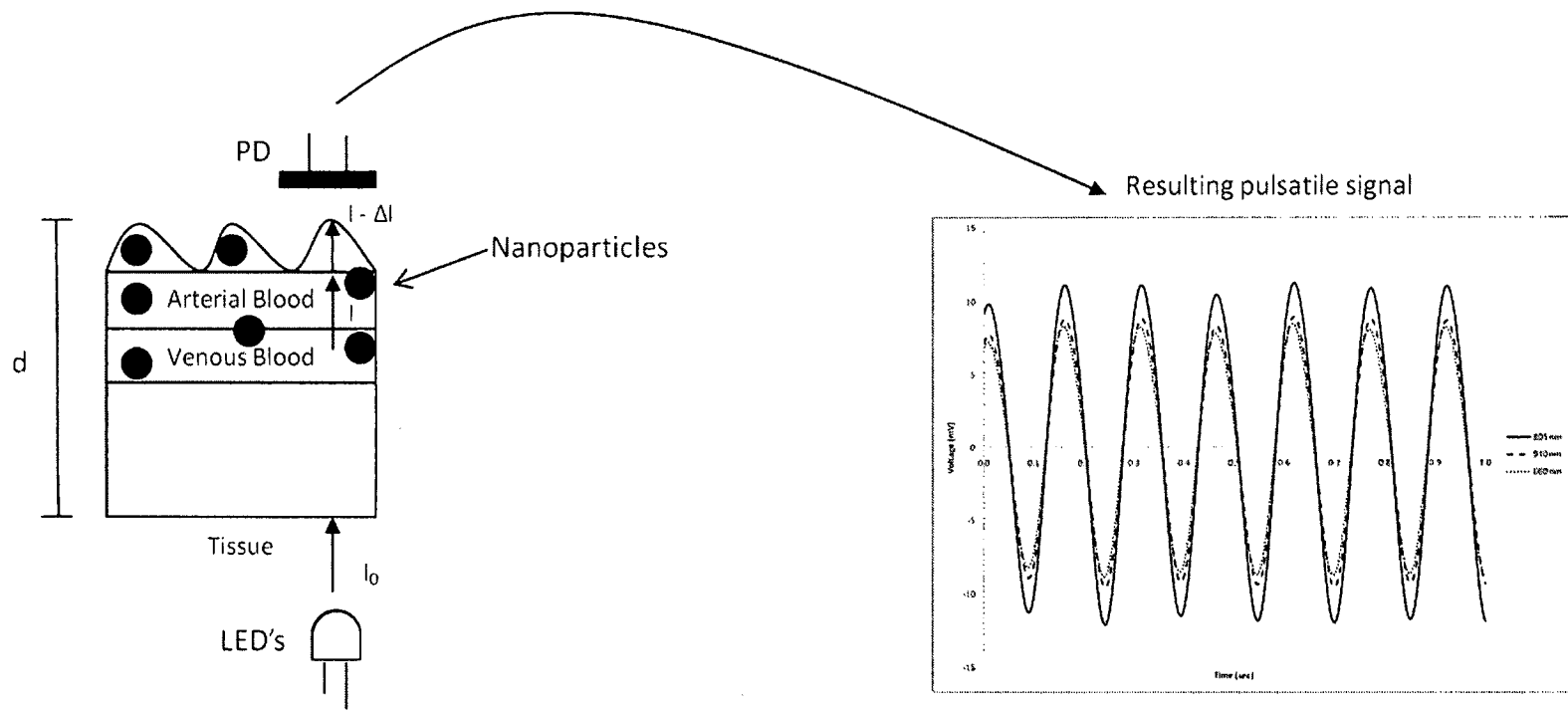
Addition of nanoparticles (nanorods in this case) causes changes in the AC and DC magnitudes at each wavelength. The most noticeable change is in the 805 nm wavelength due to preferential extinction by the nanoparticles at this wavelength.

Figure 36. Pulsatile changes in transmitted light when optically extinguishing nanoparticles are injected.

APPENDIX C

PROTOTYPE I, II, AND III INSTRUMENTATION,

SOFTWARE, AND ANESTHESIA SETUP

This section presents information about the specific instrumentation and software comprising the prototype I photometer (Figure 37) and the prototype II/III pulse photometer (Figure 38-44). It also gives a description of the murine interface with the pulse photometer and anesthesia delivery system (Figure 45) as well as a schematic of the anesthesia delivery system (Figure 46).
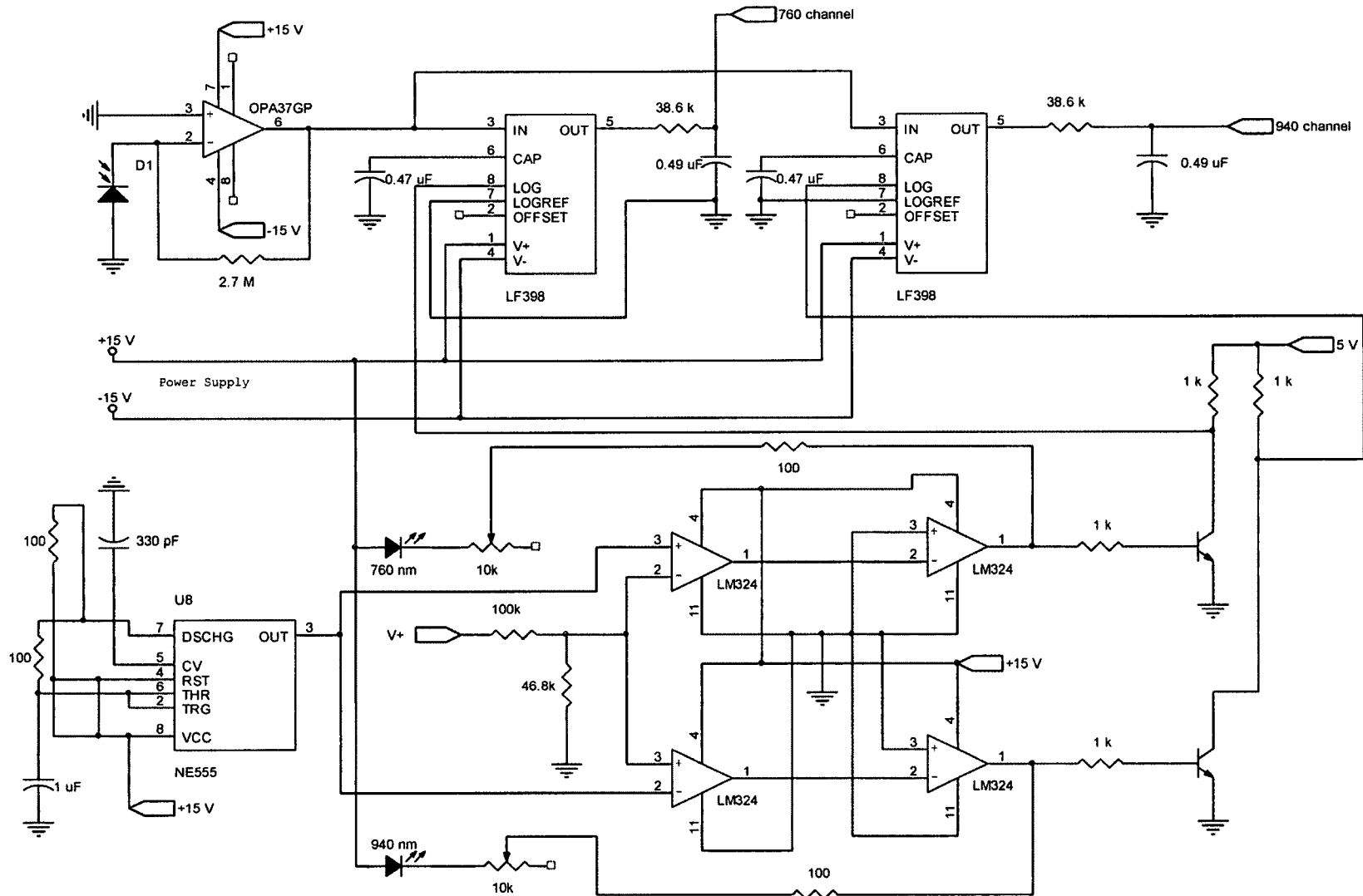
Figure 37. Prototype I photometer circuit diagram.
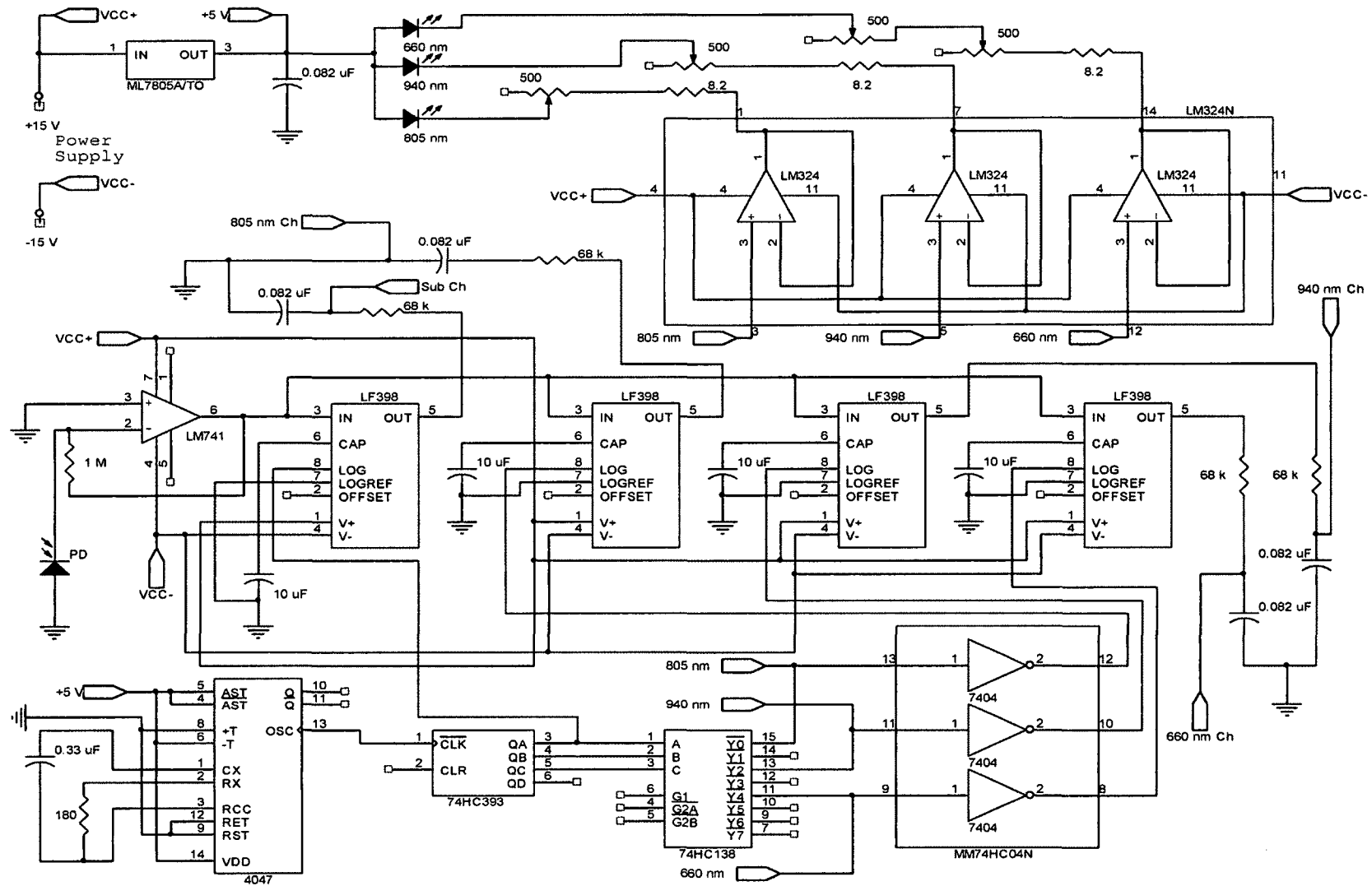
Figure 38. Prototype II/III pulse photometer circuit diagram.
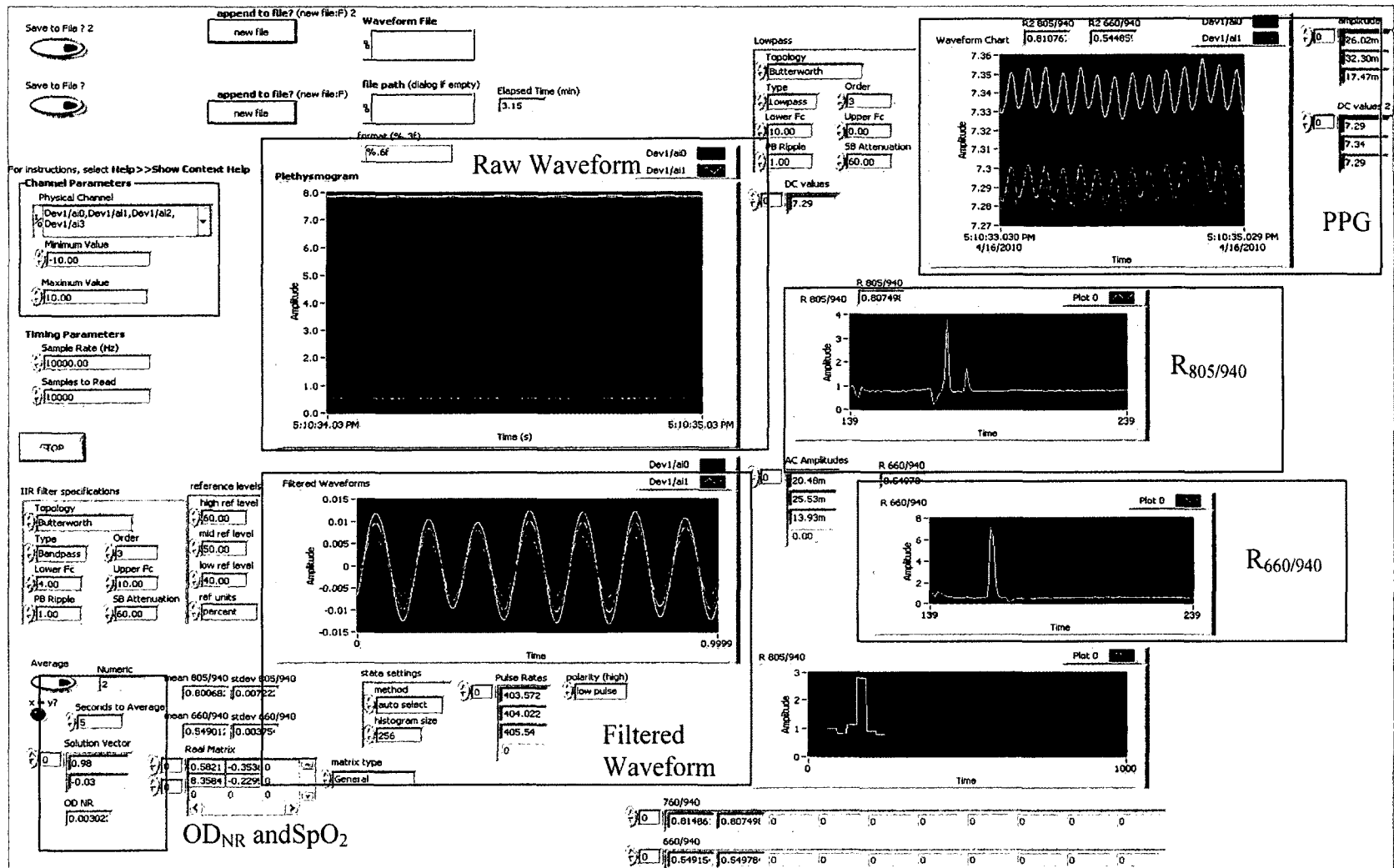
Figure 39. LabVIEW front panel of the prototype III pulse photometer
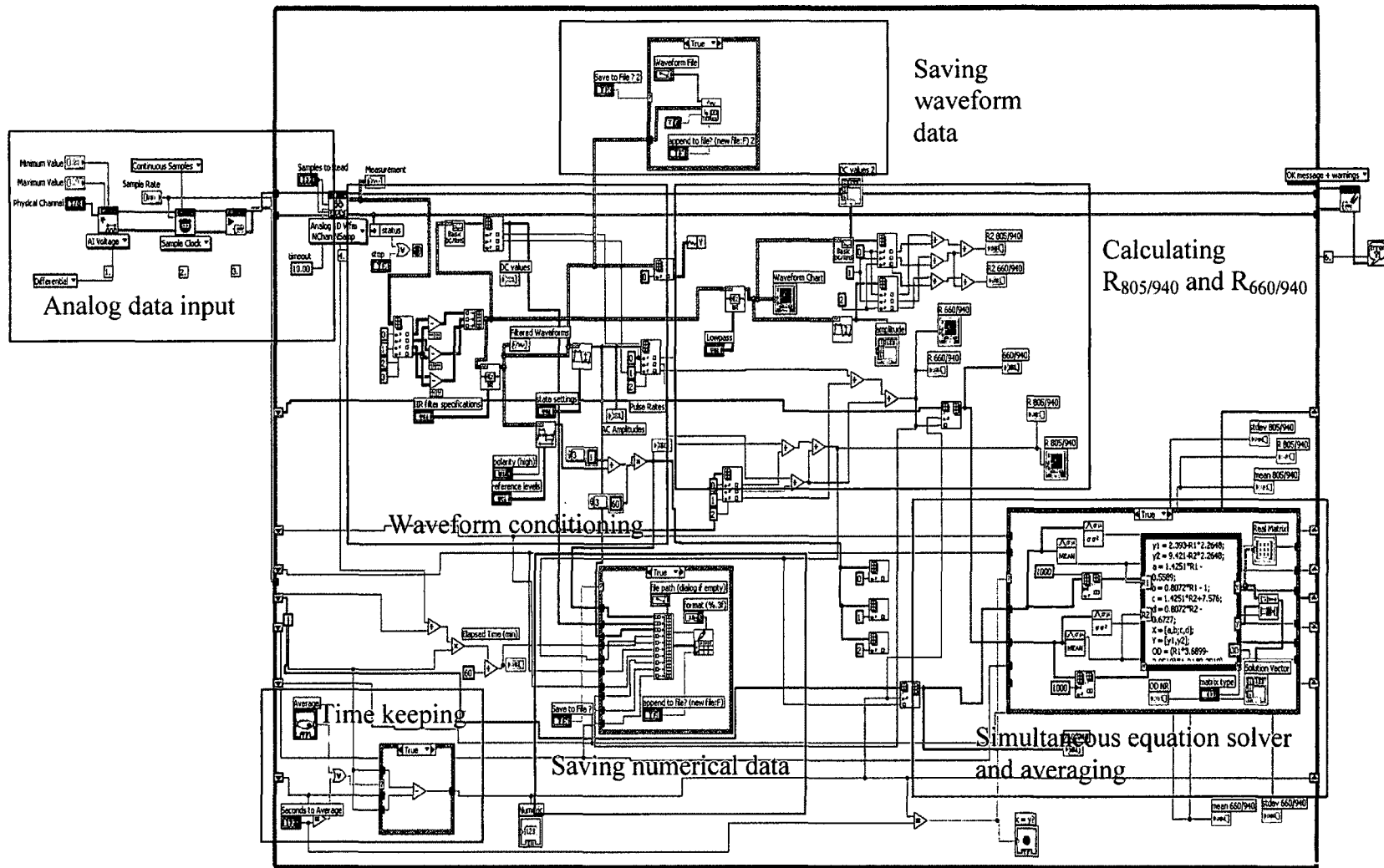
Figure 40. LabVIEW block diagram of the prototype III pulse photometer.
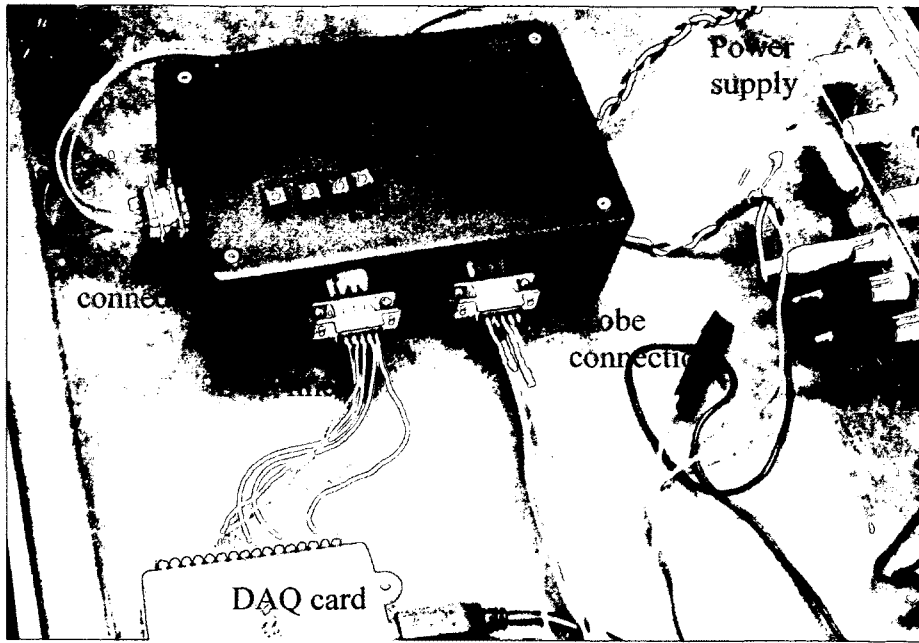
Figure 41. Prototype II/III instrumentation.
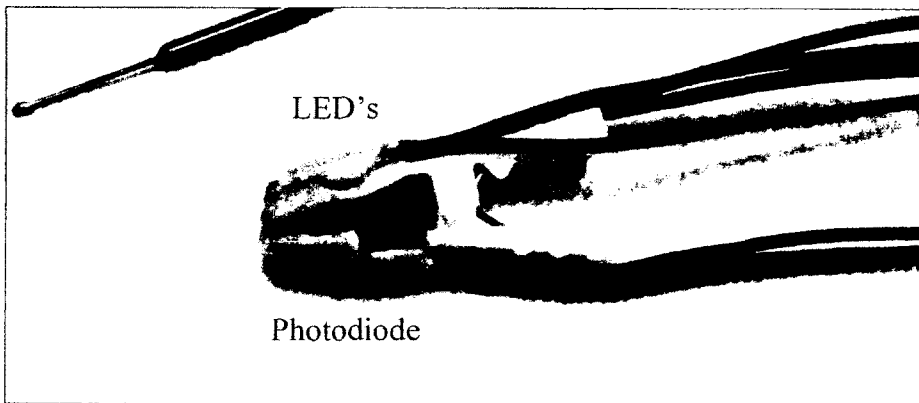
Figure 42. Leg clip for prototype II/III pulse photometer.
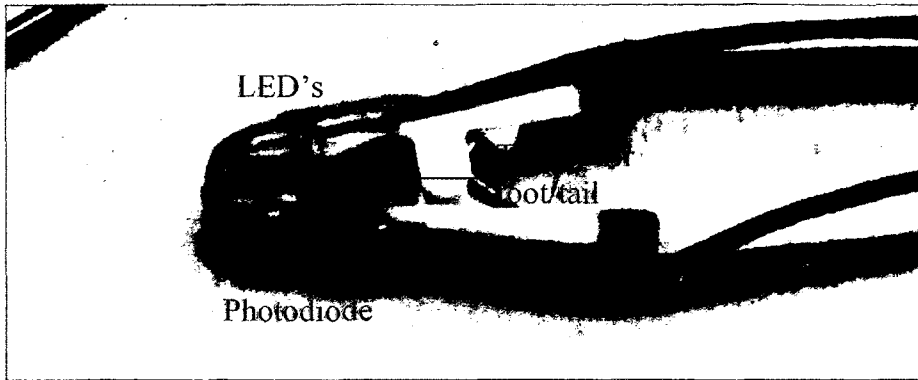
Figure 43. Foot/leg clip for the prototype II/III pulse photometer.
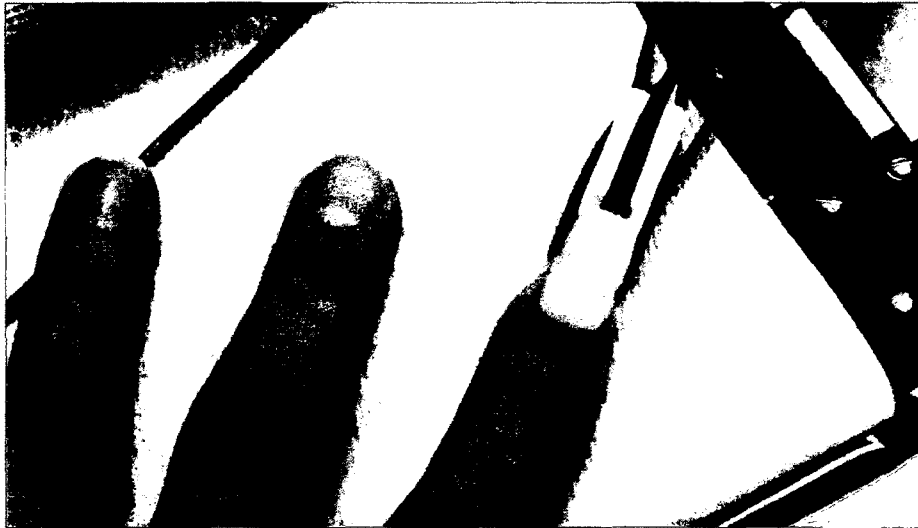
Figure 44. Human index finger interface with mouse leg probe.
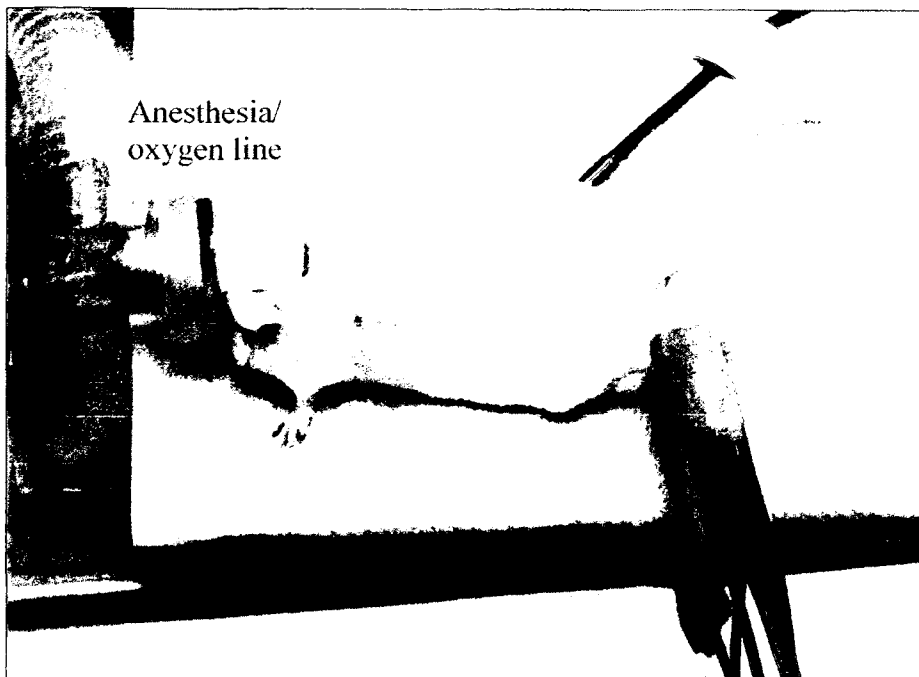
Figure 45. Murine interface with the foot/tail probe while under anesthesia.
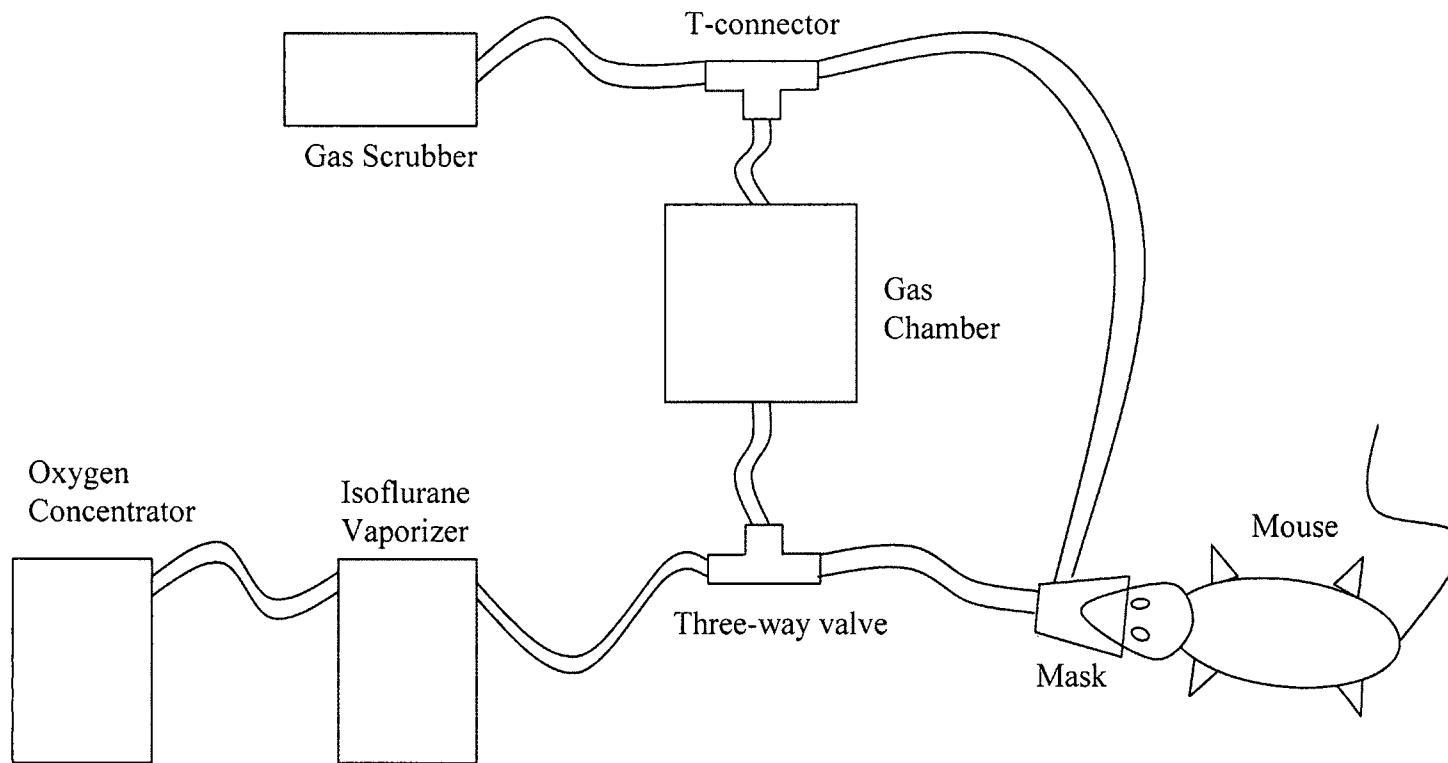
Figure 46. Schematic diagram of the isoflurane anesthesia setup.

APPENDIX D

NANOPARTICLE BIOAVAILABILITY CURVES

The experimental gold nanoshell bioavailability curves measured with a single

wavelength (760 nm) using the prototype I photometer described in Chapter 3 are given

in Figure 47, Figure 48, and Figure 49. The estimates of nanoshell concentration using

the photometer are displayed as the grey continuous plots with the half-life determined

using the black section of these plots fitted to a single exponential decay. The point

measurements of nanoshell concentration using UV/Vis spectrophotometry are displayed

as black dots and are also fitted to single exponential decays to determine the circulation

half-life.
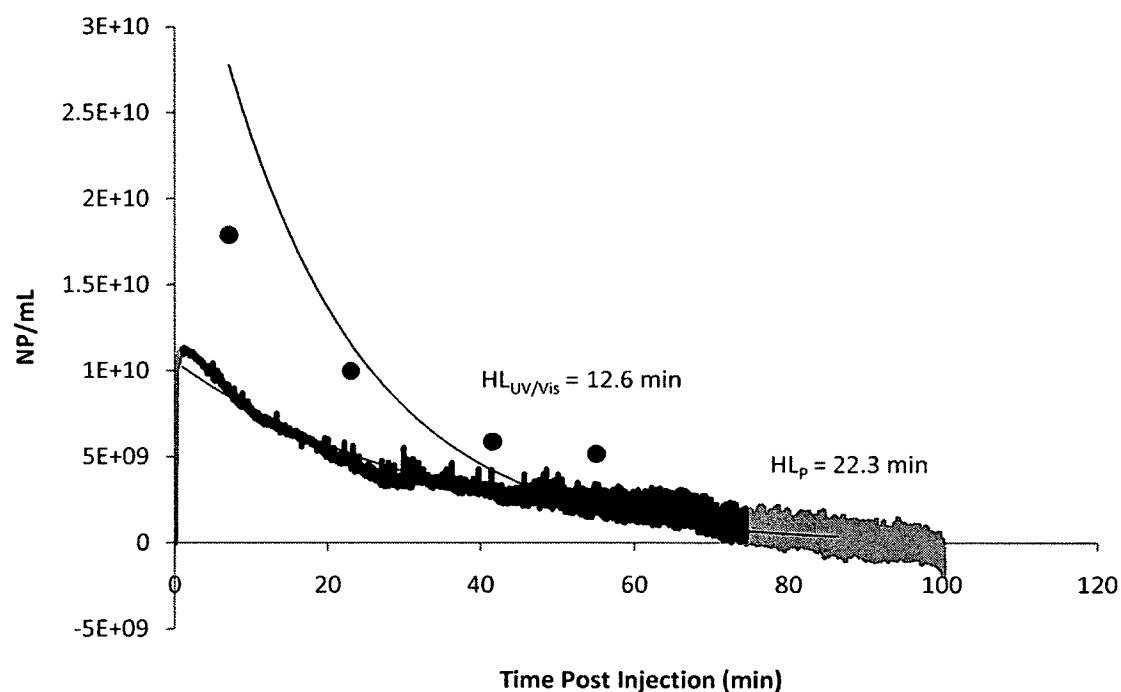
Figure 47. Experimental gold nanoshell bioavailability in mouse B.
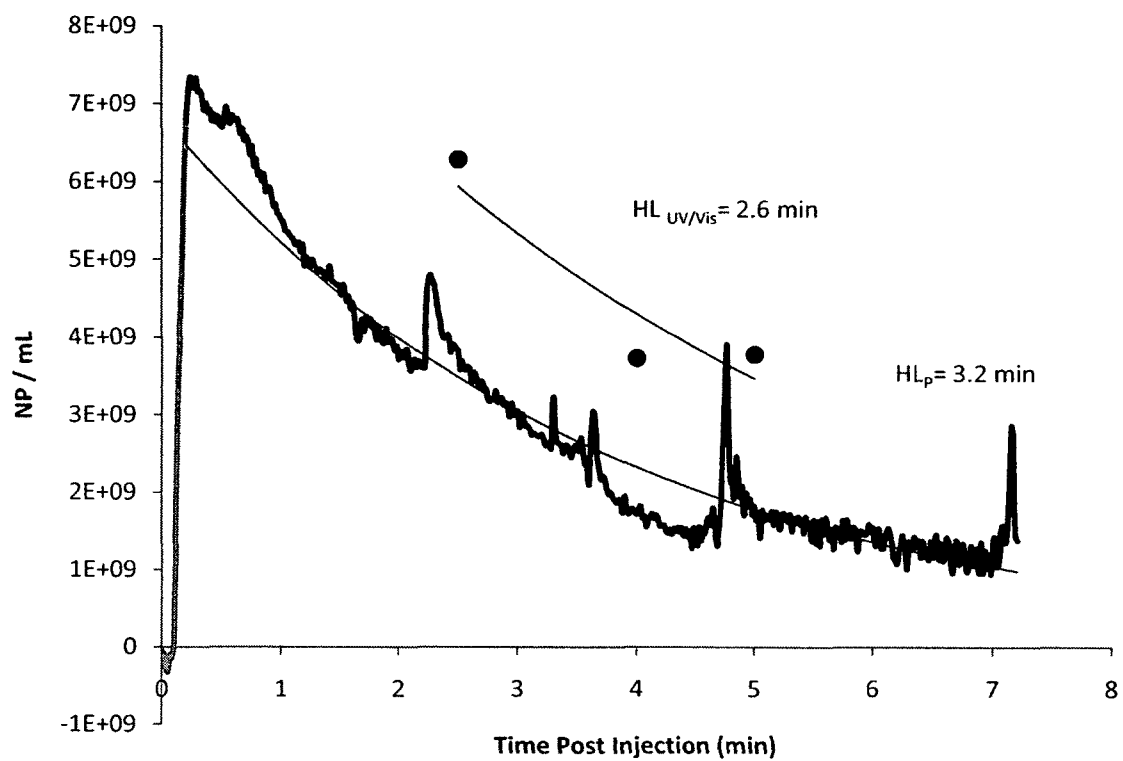
Figure 48. Experimental gold nanoshell bioavailability in mouse C.
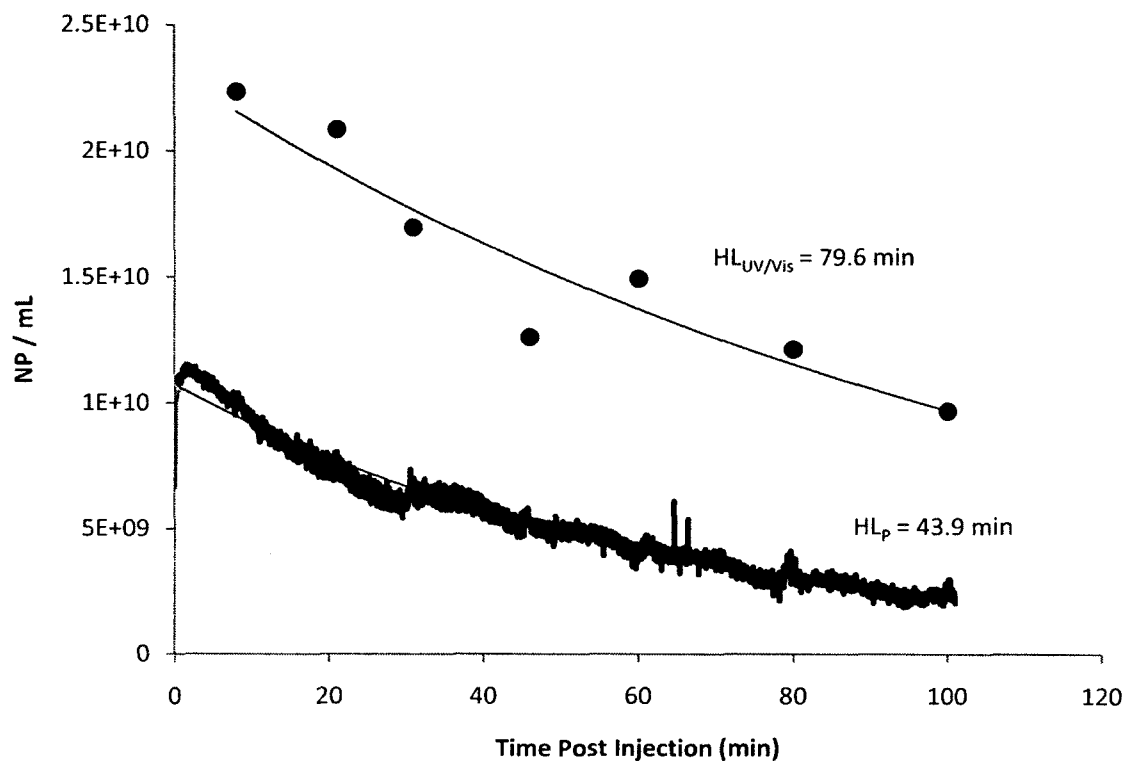
Figure 49. Experimental gold nanoshell bioavailability in mouse D.

The point measurements of nanoshell optical density as measured with UV/Vis

spectrophotometry and the corresponding ΔR as measured by pulse photometry from

Chapter 4 are presented (Figures 50-54). Circulation half-lives were calculated using a

single exponential decay for each data set and are displayed in the graphs. The

measurements of ΔR are represented with the black boxes plotted with respect to the right

axis. The measurements of optical density are represented with grey diamonds plotted

with respect to the left axis.
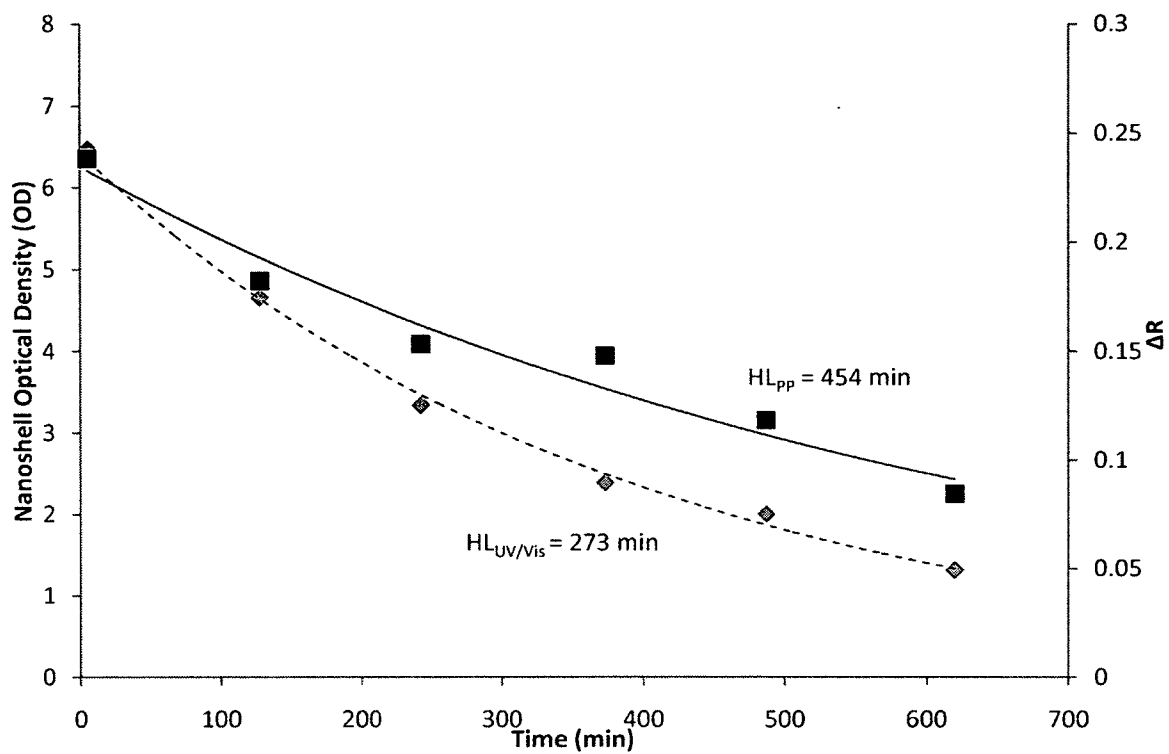
Figure 50. Gold nanoshell bioavailability in mouse 1.

156
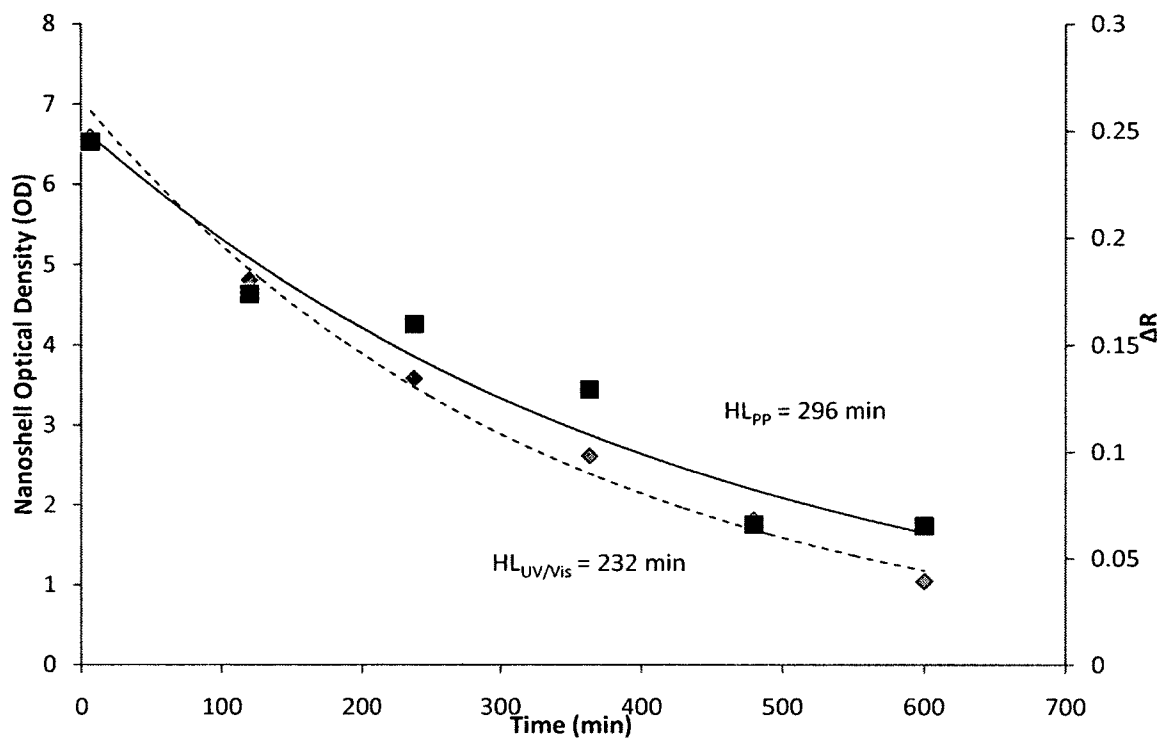
Figure 51. Gold nanoshell bioavailability in mouse 2.
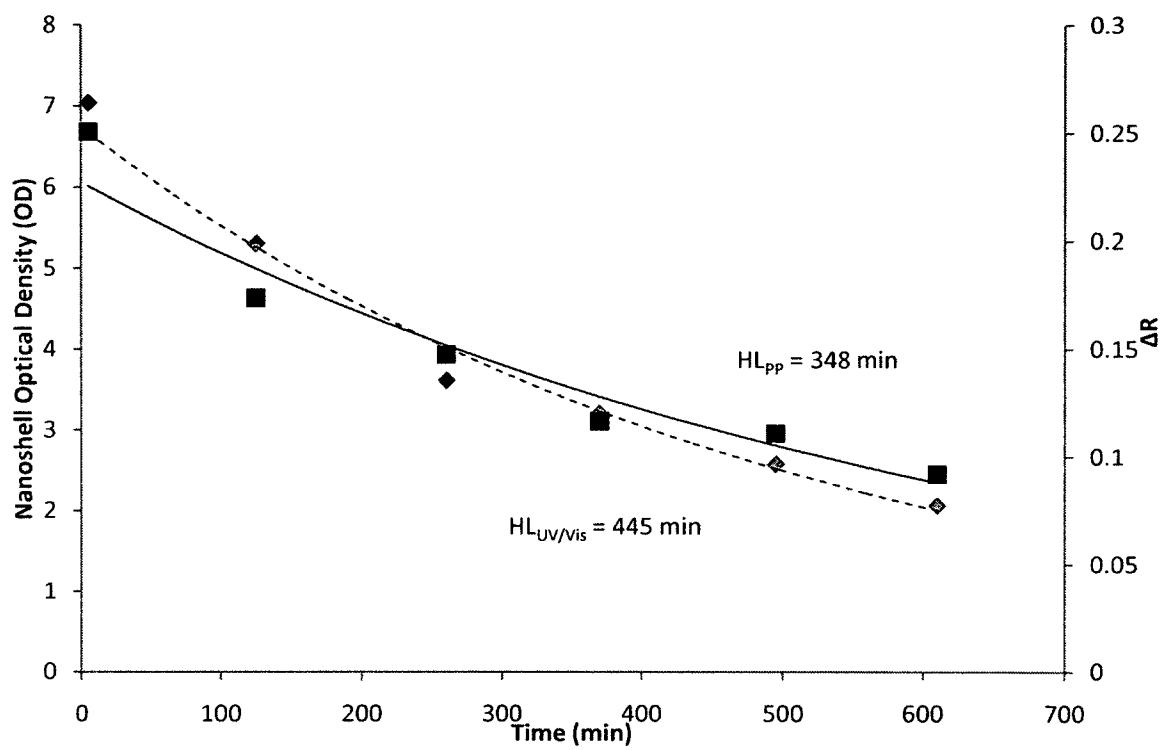
Figure 52. Gold nanoshell bioavailability in mouse 3.
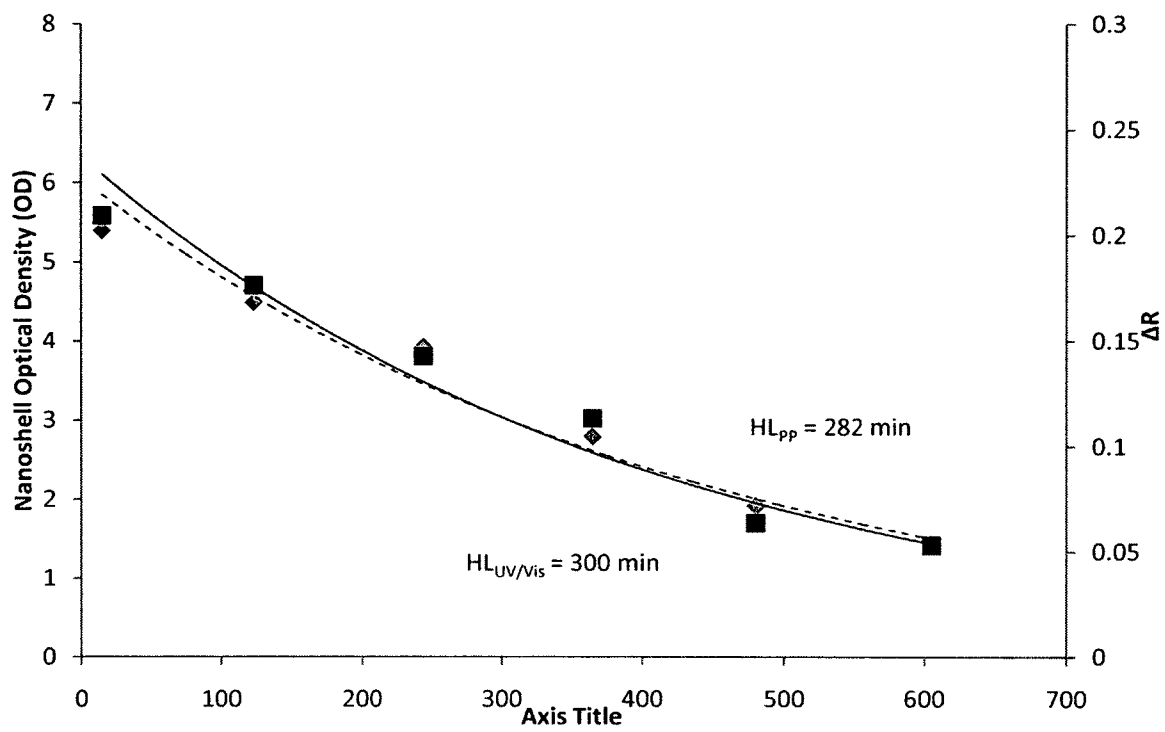
Figure 53. Gold nanoshell bioavailability in mouse 4.
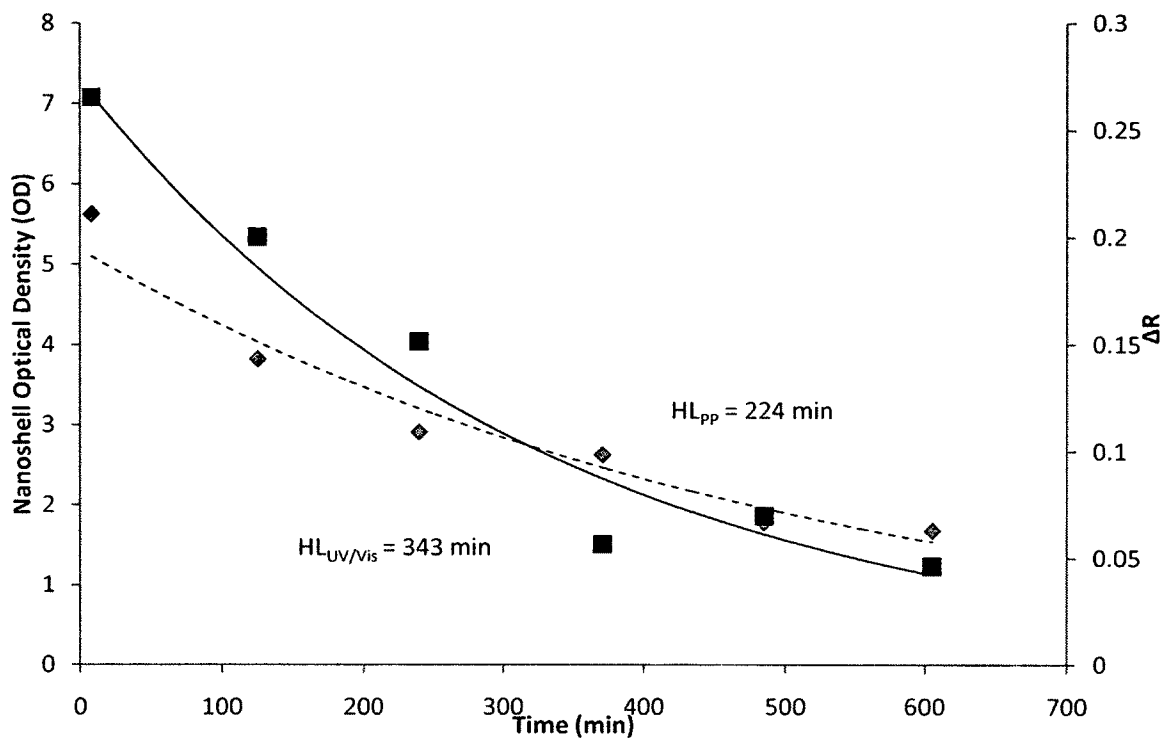
Figure 54. Gold nanoshell bioavailability in mouse 5.

The point measurements of nanorod optical density in whole blood determined with pulse photometry and UV/Vis spectrophotometry described in Chapter 5 are presented in Figure 55-59. The estimates using the pulse photometer are represented by the black squares and the estimates using spectrophotometry are represented with the grey diamonds. Circulation half-lives are estimated using single exponential functions fitted to the data.
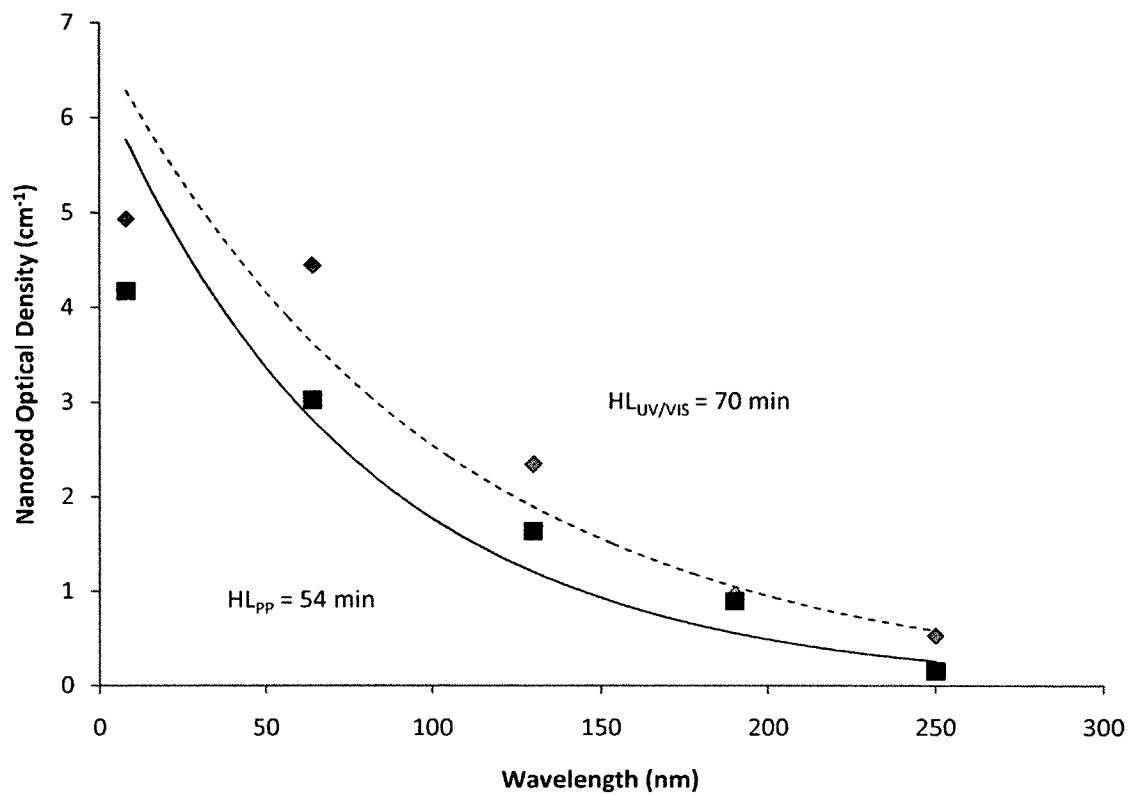
Figure 55. Gold nanorod bioavailability in mouse 1.
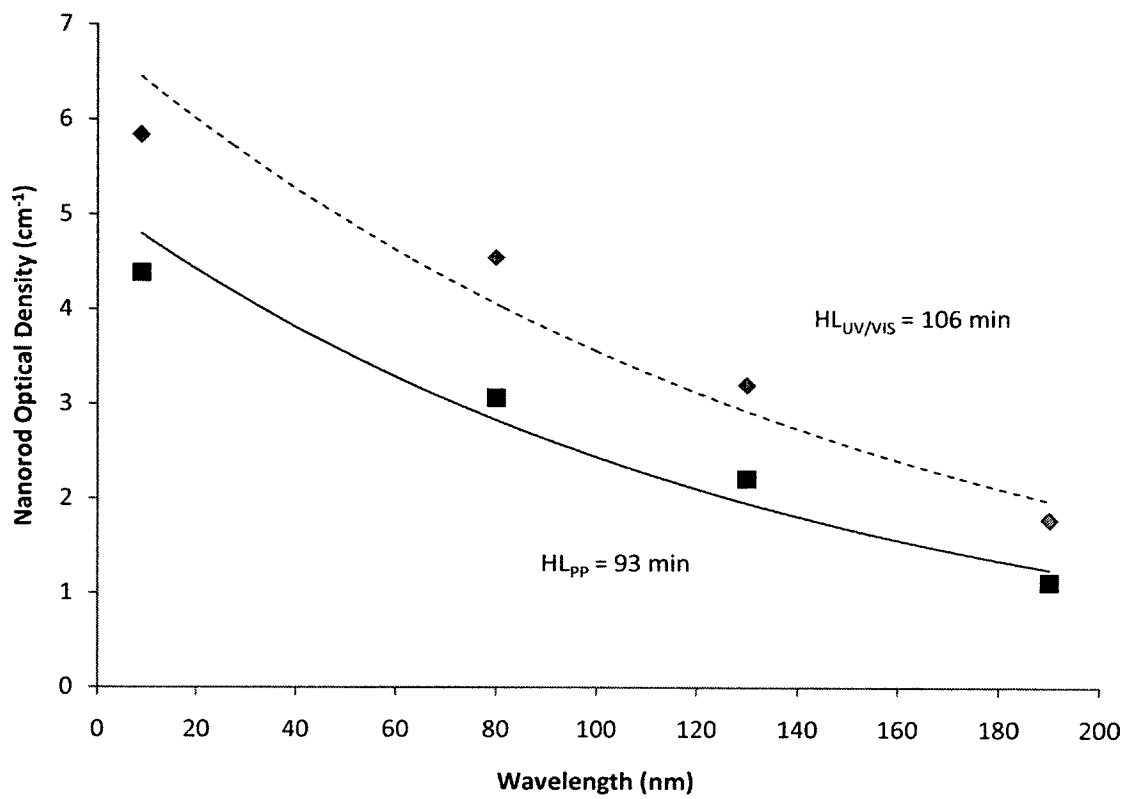
Figure 56. Gold nanorod bioavailability in mouse 2.
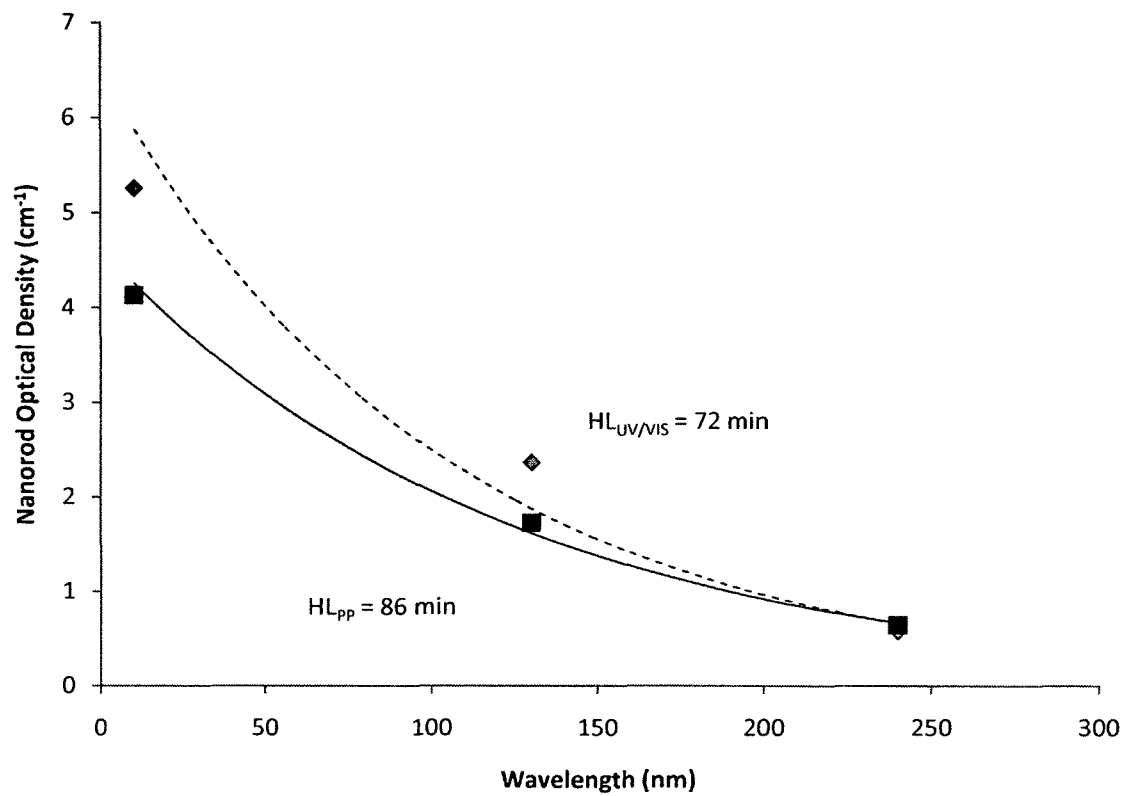
Figure 57. Gold nanorod bioavailability in mouse 3.
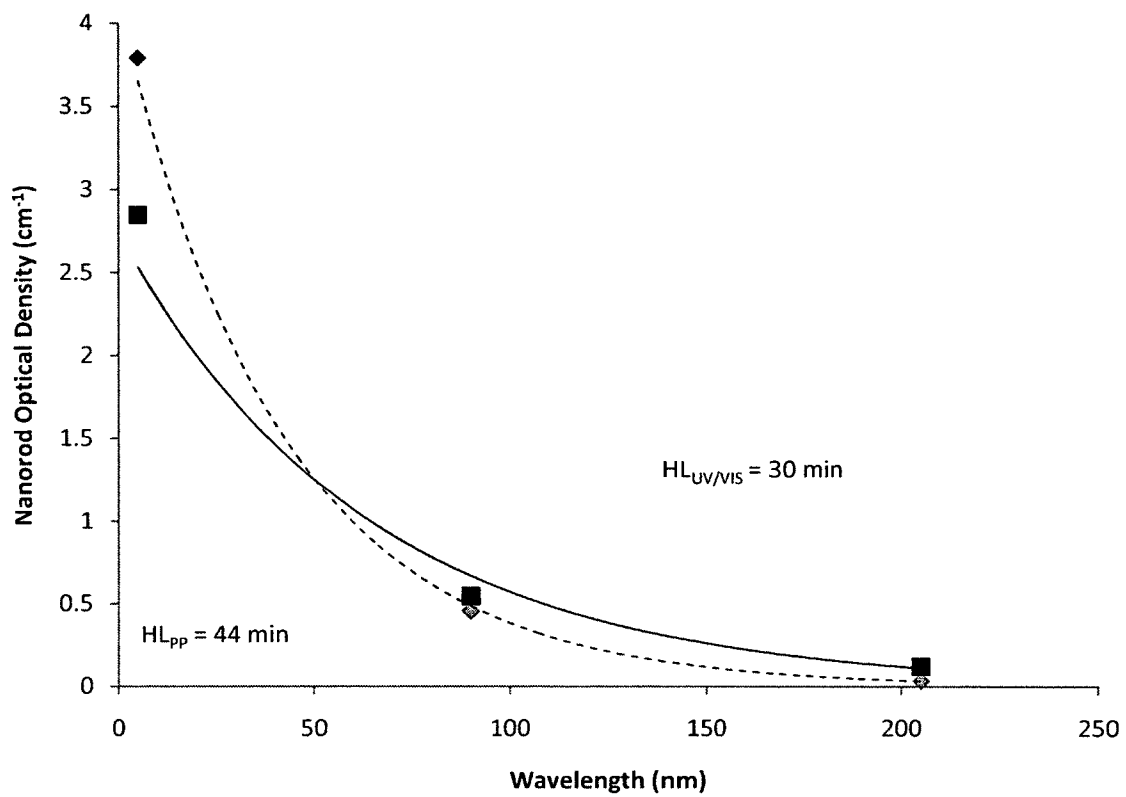
Figure 58. Gold nanorod bioavailability in mouse 4.
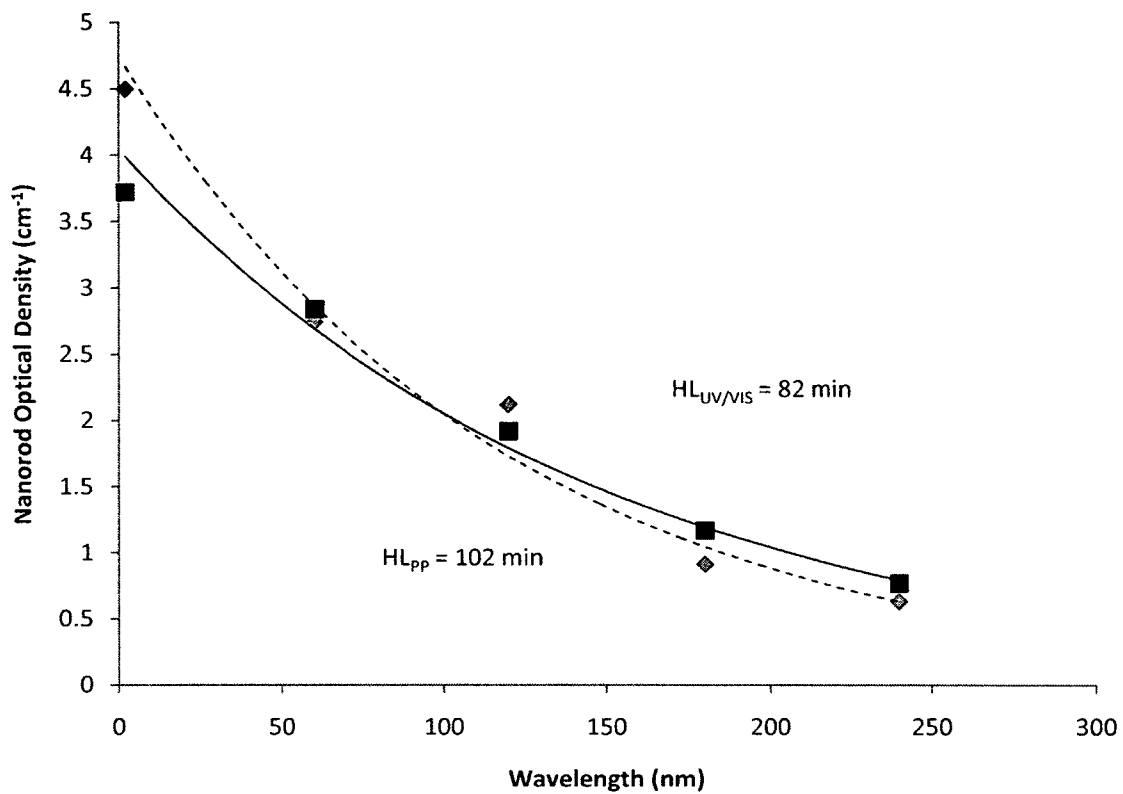
Figure 59. Gold nanorod bioavailability in mouse 5.

APPENDIX E

SAMPLE PHOTOPLETHYSMOGRAMS

FROM SITE-BY-SITE ANALYSIS

Example PPG's taken from the mouse used in the site-by-site analysis are presented in Figures 60-62. These waveforms show one second of bandpass filtered data at 805, 940, and 660 nm taken from the foot, leg, and tail of the mouse and therefore account only for the AC magnitude of the PPG.
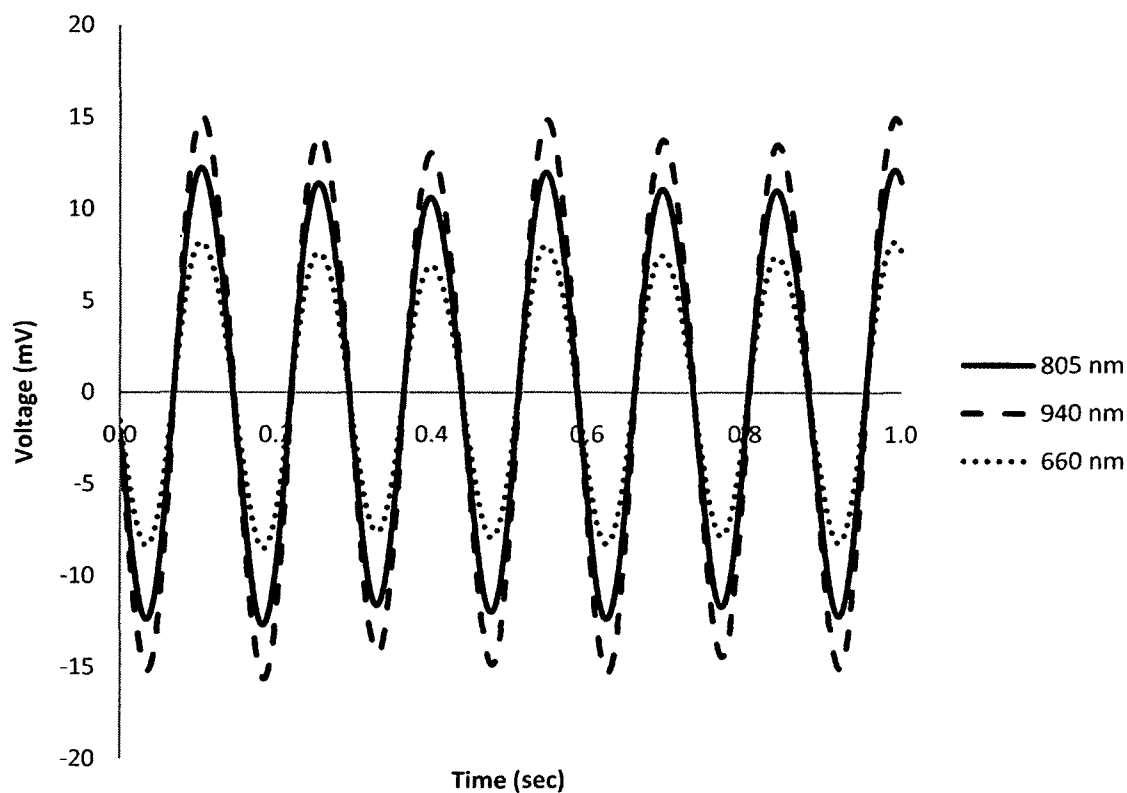
Figure 60. Three-wavelength PPG collected from a mouse's foot.
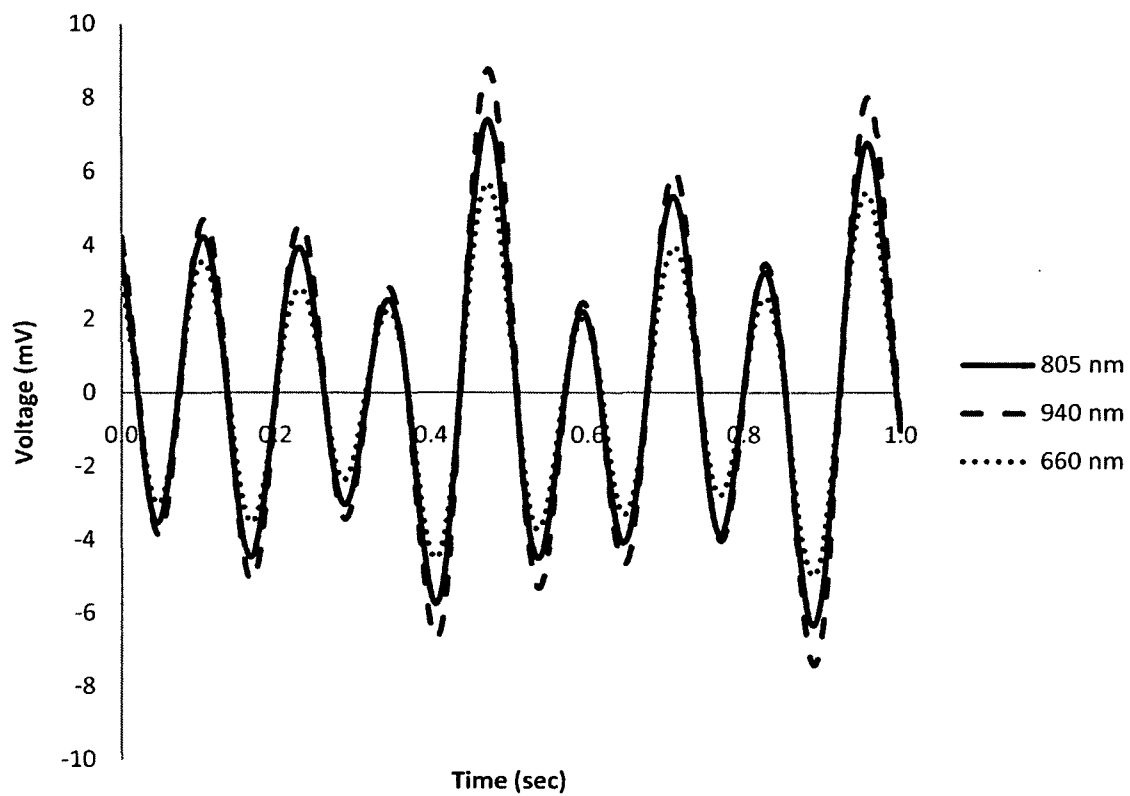
Figure 61. Three-wavelength PPG collected from a mouse's leg.
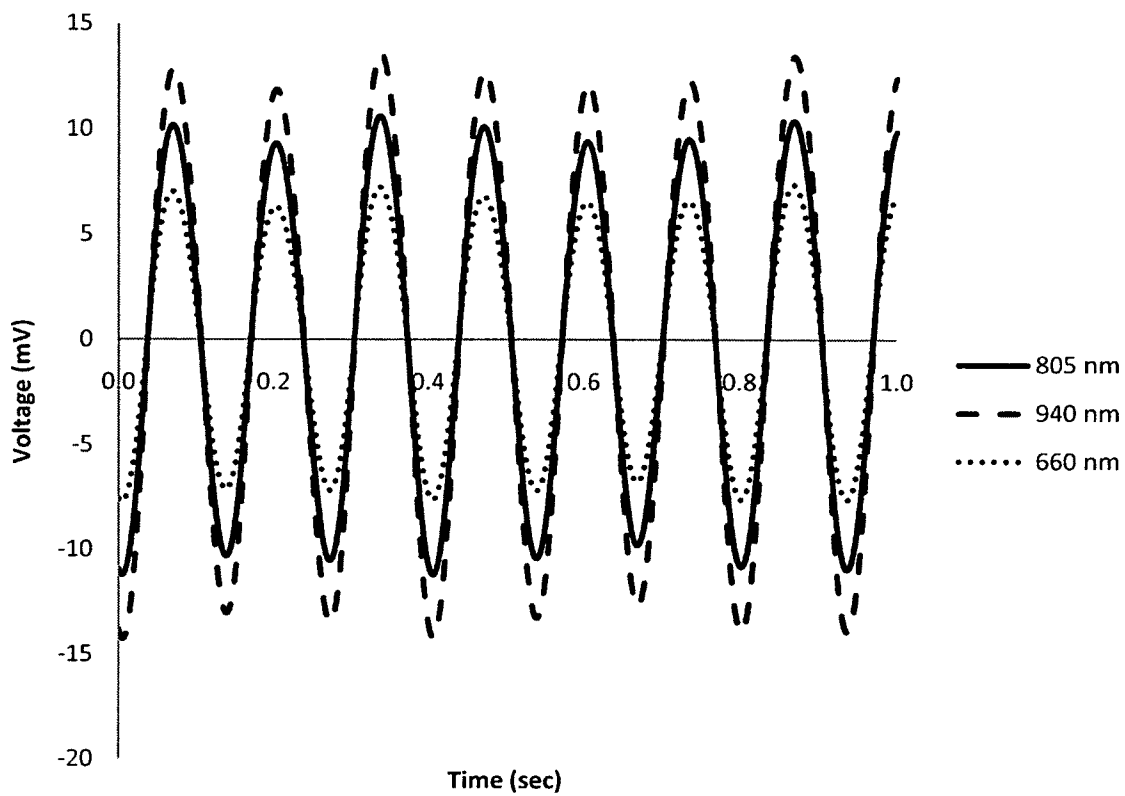
Figure 62. Three-wavelength PPG collected from a mouse's foot.

APPENDIX F

INSTITUTIONAL ANIMAL CARE AND

USE COMMITTEE APPROVAL

INSTITUTIONAL ANIMAL CARE AND USE COMMITTEE
Louisiana Tech University

10 October 2007

Dr. Patrick O'Neal
Biomedical Engineering
Louisiana Tech University
Campus P.O. Box # 58

Dear Dr. O'Neal:

The Institutional Animal Care and Use Committee (IACUC) met and approved the expedited of your experimental protocol entitled:

Real-Time Optical Nanoparticle Tracking in Circulation

The proposed procedures have scientific merit and were found to provide reasonable and adequate safeguards for the comfort of the animals, the safety of the researchers and the participating students.

Please remember that you are required to keep adequate and accurate records of all procedures, results, and the number of animals used in this protocol for three years after termination of the project. These records must be available for review by the IACUC or state and federal animal use agencies. Each year in October you will be required to complete a summary of animals used for the United States Agricultural Agency (USDA). Note that failure to follow this protocol as approved may result in the termination of research. If you have any questions please call me at 257-5206 or best via e-mail at jgspauld@latech.edu.

Sincerely,
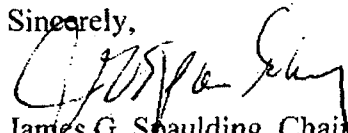
James G. Spaulding, Chair
Louisiana Tech University IACUC

REFERENCES

[1] H. Ai, S. A. Jones, and Y. M. Lvov, "Biomedical applications of electrostatic layer-by-layer nano-assembly of polymers, enzymes, and nanoparticles," *Cell Biochemistry and Biophysics*, vol. 39, pp. 23-43, 2003.

[2] G. T. Hermanson, *Bioconjugate Techniques*, San Diego, CA, Academic Press, 1996.

[3] T. G. Shutava, S.S. Balkundi, P. Vangala, J. Steffan, R. L. Bigelow, J. A. Cardelli, D. P. O'Neal, and Y. M. Lvov, "Layer-by-Layer-Coated Gelatin Nanoparticles as a Vehicle for Delivery of Natural Polyphenols," *ACS Nano*, vol. 3, pp. 1877-1885, 2009.

[4] E. I. Altinoglu, T. J. Russin, J. M. Kaiser, B. M. Barth, P. C. Eklund, M. Kester, and J. H. Adair, "Near-Infrared Emitting Fluorophore Doped Calcium Phosphate Nanoparticles for *In Vivo* Imaging of Human Breast Cancer," *ACS Nano*, vol. 2, pp. 2075-2084, 2008.

[5] M. Ferrari, "Cancer Nanotechnology: Opportunities and Challenges," *Nature Reviews: Cancer*, vol. 5, pp. 161-171, 2005.

[6] R. A. Weinberg, *The Biology of Cancer*, New York, NY: Garland Science, 2007.

[7] M. P. Melancon, W. Lu, Z. Yang, R. Zhang, Z. Cheng, A. M. Elliot, J. Stafford, T. Olsen, J. Z, Zhang, and C. Li, "*In vitro* and *in vivo* targeting of hollow gold nanoshells directed at epidermal growth factor receptor for photo thermal therapy," *Molecular Cancer Therapy*, vol. 7, no. 6, pp. 1730-1739, 2008.

[8] G. Prencipe, S. M. Tabakman, K. Welsher, Z. Liu, A. P. Goodwin, L. Zhang, J. Henry, and H. Dai, "PEG branched polymer for functionalization of nanomaterials with ultralong blood circulation," *Journal of the American Chemical Society*, vol. 131, pp. 4783-4787, 2009.

[9] T. Niidome, M. Yamagata, Y. Okamoto, Y. Akiyama, H. Takahashi, T. Kawano, Y. Katayama, Y. Niidome, "PEG-modified gold nanorods with stealth character for *in vivo* applications," *Journal of Controlled Release*, vol. 114, pp. 343-347, 2006.

[10]   Y. Akiyama, T. Mori, Y. Katayama, T. Niidome, "The effects of PEG grafting level and injection dose on gold nanorod biodistribution in the tumor-bearing mice," *Journal of Controlled Release*, vol. 139, pp. 81-84, 2009.

[11]   L. R. Hirsch, A. M. Gobin, A. R. Lowery, F. Tam, R. A. Drezek, N. J. Halas, and J. L. West, "Metal Nanoshells," *Annals of Biomedical Engineering*, vol. 34, no. 4, 2006.

[12]   S. J. Oldenburg, R. D. Averitt, S. L. Westcott, N. J. Halas, "Nanoengineering of optical resonances," *Chemical Physics Letters*, 28, 243-247, 1998.

[13]   H. Wang, T. B. Huff, D. A. Zweifel, W. He, P. S. Low, A. Wei, J. Cheng, "*In vitro* and *in vivo* two-photon luminescence imaging of single gold nanorods," *Proceedings of the National Academy of Sciences*, vol. 102, no. 44, pp. 15752-15756, 2006.

[14]   A. M. Elliot, R. J. Stafford, J. Schwartz, J. Wang, A. M. Shetty, C. Bougoyne, P. O'Neal, and J. D. Hazle, "Laser-induced thermal response and characterization of nanoparticles for cancer treatment using magnetic resonance thermal imaging," *Medical Physics*, vol. 34, no. 7, pp. 3102-3108, 2007.

[15]   X. Huang, P. K. Jain, I. H. El-Sayed, and M. A. El-Sayed, "Plasmonic photo thermal therapy (PPTT) using gold nanoparticles," *Lasers in Medical Science*, vol. 23, pp. 217-228, 2008.

[16]   H. Liu, D. Chen, F. Tang, G. Du, L. Li, X. Meng, W. Liang, Y. Zhang, X. Teng, and Y. Li, "Photo thermal therapy of Lewis lung carcinoma in mice using gold nanoshells on carboxylated polystyrene spheres," *Nanotechnology*, vol. 19, pp. 1-7, 2008.

[17]   P. Diagaradjane, A. Shetty, J. C. Wang, A. M. Elliot, J. Schwartz, S. Shentu, H. C. Park, A. Deorukhkar, R. J. Stafford, S. H. Cho, J. W. Tunnell, J. D. Hazle, and S. Krishnan, "Modulation of *in vivo* tumor radiation response via gold nanoshell-mediated vascular-focused hyperthermia: Characterizing an integrated antihypoxic and localized vascular disrupting targeting strategy," *Nanoletters*, vol. 8, no. 5, pp. 1492-1500, 2008.

[18]   J. Park, G. von Maltzhan, M. J. Xu, V. Fogal, V. R. Kotamraju, E. Ruoslahti, S. N. Bhatia, and M. J. Sailor, "Cooperative nanomaterial system to sensitize, target, and treat tumors," *Proceedings of the National Academy of Sciences*, vol. 107, no. 3, pp. 981-986, 2010.

[19]   Y. Huang, K. Sefah, S. Bamrungsap, H. Chang, and W. Tan, "Selective photo thermal therapy for mixed cancer cells using aptamer-conjugated nanorods," *Langmuir*, vol. 24, pp. 11860-11865, 2008.

[20]   R. S. Norman, J. W. Stone, A. Gole, C. J. Murphy, and T. L. Sabo-Attwood, "Targeted photo thermal lysis of the pathogenic bacteria, pseudomonas aeruginosa, with gold nanorods," *Nanoletters*, vol. 8, no. 1, pp. 302-306, 2007.

[21]   T. Kawano, Y. Niidome, T. Mori, Y. Katayama, and T. Niidome, "PNIPAM gel-coated gold nanorods for targeted delivery responding to a near-infrared laser," *Bioconjugate Chemistry*, vol. 20, pp. 209-212, 2009.

[22]   H. Huang, S. Barua, D. B. Kay, and K. Rege, "Simultaneous enhancement of photo thermal stability and gene delivery efficacy of gold nanorods using polyelectrolytes," *ACS Nano*, vol. 3, no. 10, pp. 2941-2952, 2009.

[23]   S. Lal, S. E. Clare, and N. J. Halas, "Nanoshell-enabled photo thermal cancer therapy: Impending clinical impact," *Accounts of Chemical Research*, vol. 41, no. 12, pp. 1842-1851, 2008.

[24]   A. M. Gobin, M. H. Lee, N. J. Halas, W. D. James, R. A. Drezek, and J. L. West, "Near-infrared resonant nanoshells for combined optical imaging and photo thermal cancer therapy," *Nanoletters*, vol. 7, no. 7, pp. 1929-1934, 2007.

[25]   R. T. Zaman, P. Diagaradjane, J. C. Wang, J. Schwartz, N. Rajaram, K. L. Gill-Sharp, S. H. Cho, H. G. Rylander, J. D. Payne, S. Krishnan, and J. W. Tunnell, "*In vivo* detection of gold nanoshells in tumors using diffuse optical spectroscopy," vol. 13, no. 6, pp. 1715-1720, 2007.

[26]   W. D. James, L. R. Hirsch, J. L. West, P. D. O'Neal, and J. D. Payne, "Application of INNA to the build-up and clearance of gold nanoshells in clinical studies in mice," *Journal of Radioanalytical and Nuclear Chemistry*, vol. 271, no. 2, pp. 455-459, 2007.

[27]   H. Xie, K. L. Gill-Sharp, and D. P. O'Neal, "Quantitative estimation of gold nanoshell concentrations in whole blood using dynamic light scattering," *Nanomedicine: Nanotechnology, Biology, and Medicine*, vol. 3, pp. 89-94, 2007.

[28]   T. Niidome, Y. Akiyama, K. Shimoda, T. Kawano, T. Mori, Y. Katayama, and Y. Niidome, "*In vivo* monitoring of intravenously injected gold nanorods using near-infrared light," *Small*, vol. 4, no. 7, pp. 1001-1007, 2008.

[29]   J. Webster, *Medical Instrumentation: Application and Design*, Hoboken, NJ, John Wiley & Sons, 1998.

[30]   J. W. Severinghaus, and Y. Honda, "History of blood gas analysis VII. Pulse oximetry," *Journal of Clinical Monitoring*, vol. 3, pp. 135-138, 1987.

[31]   S. Prahl, Tabulated hemoglobin molar extinction coefficients at the Oregon
        Medical Laser Center website, http://omlc.ogi.edu/spectra/hemoglobin/index.html
        (accessed April 20, 2010)

[32]   W. G. Zijlstra, A. Buursma, and W. P. Meeuwsen-van der Roest, "Absorption
        spectra of human fetal and adult oxyhemoglobin, de-oxyhemoglobin,
        carboxyhemoglobin, and methemoglobin," *Clinical Chemistry*, vol. 37, no. 9, pp.
        1633-1636, 1991.

[33]   J. G. Webster, *Design of Pulse Oximeters*, New York, NY, Taylor & Francis
        Group, 1997.

[34]   J. Spigulis, "Optical non-invasive monitoring of skin blood pulsations," *Appied
        Optics*, vol. 44, no. 10, pp. 1850-1857, 2005.

[35]   J. Spigulis, L. Gailite, A. Lihachev, and R. Erts, "Simultaneous recording of skin
        blood pulsations at different vascular depths by multiwavelength
        photoplethysmography," *Applied Optics*, vol. 46, no. 10, pp. 1754-1759, 2007.

[36]   M. Sandberg, Q. Zhang, J. Styf, B. Gerdie, and J. L. Lindberg, "Non-invasive
        monitoring of muscle blood perfusion by photoplethysmography: evaluation of a
        new application," *Acta Physiology Scandanavia*, vol. 183, pp. 335-343, 2005.

[37]   M. Nitzan, S. Turivnenko, A. Milston, A. Babchenko, and Y. Mahler, "Low-
        frequency variability in the blood volume and in the blood volume pulse
        measured by photoplethysmography," *Journal of Biomedical Optics*, vol. 1, no. 2,
        pp. 223-229, 1996.

[38]   S. Bergstrand, L. G. Lindberg, A. Ek, M. Linden, and M. Lindgren, "Blood flow
        measurements at different depths using photoplethysmography and laser doppler
        techniques," *Skin Research and Technology*, vol. 15, pp. 139-147, 2009.

[39]   K. Yamakoshi, and Y. Yamakoshi, "Pulse glucosimetry: a new approach for
        noninvasive blood glucose measurement using instantaneous differential near-
        infrared spectrophotometry," *Journal of Biomedical Optics*, vol. 11, no. 5, pp.
        054028-1-054028-9, 2006.

[40]   Z. Miwa, M. Ikawa, H. Iijima, M. Saito, and Y. Takagi, "Pulpal blood flow in
        vital and nonvital young permanent teeth measured by transmitted-light
        photoplethysmography: and pilot study," *Pediatric Dentistry*, vol. 24, no. 6, pp.
        594-598, 2002.

[41]   M. Nitzan, A. Patron, Z. Glik, and A. T. Weiss, "Automatic noninvasive measurement of systolic blood pressure using photoplethysmography," *Biomedical Engineering Online*, vol. 8, no. 28, pp. 1-8, 2009.

[42]   B. Jonnson, C. Laurent, T. Skau, and L. G. Lindberg, "A new probe for ankle systolic blood pressure measurement using photoplethysmography (PPG)," *Annals of Biomedical Engineering*, vol. 33, no. 2, pp. 232-239, 2005.

[43]   T. Ijima, T. Aoyagi, Y. Iwao, J. Masuda, M. Fuse, N. Kobayashi, and H. Sankawa, "Cardiac output and circulating blood volume analysis by pulse dye-densitometry," *Journal of Clinical Monitoring*, vol. 13, pp. 81-89, 1997.

[44]   A. Schuster, "Radiation through a foggy atmosphere," *The Astrophysical Journal: An International Review of Spectroscopy and Astronomical Physics*, vol. 21, no. 1, pp. 1-22, 1905.

[45]   T. Imai, C. Mitaka, T. Nosaka, A. Koike, S. Ohki, Y. Isa, and F. Kunimoto, "Accuracy and repeatability of blood volume measurement by pulse dye densitometry compared to the conventional method using 55Cr-labeled red blood cells," *Intensive Care Medicine*, vol. 26, pp. 1343-1349, 2000.

[46]   M. Reekers, M. J. G. Simon, F. Boer, R. A. G. Mooren, J. W. van Kleef, A. Dahan, and J. Vuyk, "Cardiovascular monitoring by pulse dye densitometry or arterial indocyanine green dilution," *Anesthesia and Analgesia*, vol. 109, no. 2, 2009.

[47]   E. Belin de Chantemele, G. Gauquelin-Koch, M. Duvareille, N. Pellet, C. Gharib, and M. Custaud, "Blood volume measurement: the comparison of pulse dye densitometry and Dill and Costill's methods," *Life Science*, vol. 78, 2006.

[48]   N. Aladangady, T. Leung, K. Costeloe, and D. Delpy, "Measuring circulating blood volume in newborn infants using pulse dye densitometry and indocyanine green," *Pediatric Anesthesia*, vol. 18, pp. 865-871, 2008.

[49]   S. Sakka, K. Reinhart, and A. Meier-Hellmann, "Comparison of invasive and noninvasive measurements of indocyanine green plasma disappearance rate in critically ill patients with mechanical ventilation and stable hemodynamics," *Intensive Care Medicine*, vol. 26, pp. 1553-1556, 2000.

[50]   O. Okachi, T. Kaneko, H. Sugimoto, S. Inoue, S. Takeda, and A. Nakao, "ICG pulse spectrophotometry for perioperative liver function in hepatectomy," *Journal of Surgical Research*, vol. 103, pp. 109-113, 2002.

[51] H. Akita, Y. Sasaki, T. Yamada, K. Gotoh, H. Ohigashi, H. Eguchi, M. Yano, O. Ishikawa, and S. Imaoka, Real-time intraoperative assessment of residual liver functional reserve using pulse dye densitometry," *World Journal of Surgery*, vol. 32, pp. 2668-2674, 2008.

[52] U. Merle, O. Sieg, W. Stremmel, J. Encke, and C. Eisenback, "Sensitivity and specificity of plasma disappearance rate of indocyanine green as a prognostic indicator in acute liver failure," *BMC Gastroenterology*, vol. 9, no. 91, pp. 1-7, 2009.

[53] Y. Watanabe and K. Kumon, "Assessment by pulse dye-densitometry indocyanine green (ICG) clearance test of hepatic function of patients before cardiac surgery: Its value as a predictor of serious postoperative liver dysfunction," *Journal of Cardiothoracic and Vascular Anesthesia*, vol. 13, no. 3, pp. 299-303, 1999.

[54] J. A. Tichy, M. Loucka, Z. M. Trefny, M. Hojerova, J. Svacinka, J. Muller, and M. Friedrichova, "New clearance evaluation method for hepatological diagnostics," *Physiological Research*, vol. 58, no. 2, pp. 287-292, 2009.

[55] R. Graff, A. C. M. Dassel, W. G. Zijlstra, F. F. M. de Mul, and J. G. Aarnoudse, "How tissue optics influences reflectance pulse oximetry," *Oxygen Transport to Tissue XVII*, pp. 117-132, 1996.

[56] A. Roggan, M. Friebel, K. Dorschel, A. Hahn, and G. Muller, "Optical properties of circulating human blood in the wavelength range 400-2500 nm," *Journal of Biomedical Optics*, vol. 4, no. 1, pp. 36-46, 1999.

[57] D. K. Sardar and L. B. Levy, "Optical properties of whole blood," *Lasers in Medical Science*, vol. 13, pp. 108-111, 1998.

[58] W. Cheong, S. A. Prahl, and A. J. Welch, "A review of the optical properties of biological tissues," *IEEE Journal of Quantum Electronics*, vol. 26, no. 12, 1990.

[59] D. J. Faber, M. C. G. Aalders, E. G. Mik, B. A. Hooper, M. J. C. van Gemert, and T. G. van Leeuwen, "Oxygen saturation-dependant absorption and scattering of blood," *Physical Review Letters*, vol. 93, no. 2, pp. 028102-1-028102-4, 2004.

[60] J. E. Sinex, "Pulse oximetry: Principles and limitations," *American Journal of Emergency Medicine*, vol. 17, no. 1, pp. 59-66, 1999.

[61] P. Talke and C. Stapelfeldt, "Effect of peripheral vasoconstriction on pulse oximetry," *Journal of Clinical Monitoring and Computing*, vol. 20, pp. 305-309, 2006.

[62]   Y. Yusim, D. Livingstone, A. Sidi, and D. A. Paulus, "Blue dyes, blue people: the systemic effects of blue dyes when administered via different routes," *Journal of Clinical Anesthesia*, vol. 19, pp. 315-321, 2007.

[63]   A. Sidi, W. R. Rush, D. A. Paulus, N. Gravenstein, and R. F. Davis, "Effect of fluorescene, indocyanine green, and methylene blue on the measurement of oxygen saturation by pulse oximetry," *Anesthesiology*, vol. 65, no. 3A, 1986.

[64]   M. S. Scheller, R. J. Unger, and M. J. Kelner, "Effects of intravenously administered dyes on pulse oximetry readings," *Anesthesiology*, vol. 65, no. 5, pp. 550-552, 1986.

[65]   V. H. Larsen, A. Freudendal-Pedersen, and N. Fogh-Andersen, "The influence of patent blue V on pulse oximetry and haemoximetry," *Acta Anesthesiologica Scandinavica*, vol. 39, supplementum 107, pp. 53-55, 1995.

[66]   L. Vokach-Brodsky, S. S. Jeffrey, H. J. M. Lemmens, and J. G. Brock-Utne, "Isosulfan blue affects pulse oximetry," *Anesthesiology*, vol. 93, no. 4, pp. 1002-1003, 2000.

[67]   M. El-Tamer, I. K. Komenaka, S. Curry, A. B. Troxel, B. Ditkoff, and F. R. Schnabel, "Pulse oximeter changes with sentinel lymph node biopsy in breast cancer," *Archives of Surgery*, vol. 138, pp. 1257-1260, 2003.

[68]   A. Pinero, J. Illana, C. Garcia-Palenciano, F. Canizares, M. Canteras, V. Canadillas, E. Duran, and P. Parrilla, "Effect on oximetry of dyes used for sentinel lymph node biopsy," *Archives of Surgery*, vol. 139, pp. 1204-1207, 2004.

[69]   R. W. Hoskin and R. Granger, "Intraoperative decrease in pulse oximeter readings following injection of isosulfan blue," *Canadian Journal of Anesthesia*, pp. 38-40, 2000.

[70]   Y. Chia, K. Liu, P. Kao, G. Sun, and K. Wang, "Prolonged interference of patent blue on pulse oximetry readings," *Acta Anesthesiology Singapore*, vol. 39, pp. 27-32, 2001.

[71]   P. Motiani, S. Ahuja, and S. Agrawal, "Prolonged interference of patent blue dye on pulse oximetry readings," *Journal of Anesthesia and Clinical Pharmacology*, vol. 22, no. 1, pp. 87-89, 2006.

[72]   M. Haruna, K. Kumon, N. Yahagi, Y. Watanabe, Y. Tshida, N. Kobayashi, and T. Aoyagi, "Blood volume measurement at the bedside using ICG pulse spectrophotometry," *Anesthesiology*, vol. 89, no. 6, pp. 1322-1328, 1998.

[73] W. Baulig, E. O. Bernhard, D. Bettex, D. Schmidlin, and E. R. Schmid, "Cardiac output measurement by pulse dye densitometry in cardiac surgery," *Anaesthesia*, vol. 60, pp. 968-973, 2005.

[74] N. Aravindhan and D. G. Chisholm, "Sulfhemoglobinemia presenting as pulse oximetry desaturation," *Anesthesiology*, vol. 93, no. 3, pp. 883-884, 2000.

[75] R. J. Carrico, J. Peisach, and J. O. Alben, "The preparation and some physical properties of sulfhemoglobin," *The Journal of Biological Chemistry*, vol. 253, no. 7, pp. 2386-2391, 1978.

[76] T. Aoyagi and K. Miyasaka, "Pulse Oximetry: Its invention, contribution to medicine, and future tasks," *Anesthesia and Analgesia*, vol. 94, pp. 51-53, 2002.

[77] T. Aoyagi and K. Miyasaka, "The theory and applications of pulse spectrophotometry," *Anesthesia and Analgesia*, vol. 94, pp. S93-S95, 2002.

[78] T. Aoyagi, M. Fuse, N. Kobayashi, K. Machida, and K. Miyasaka, "Multiwavelength pulse oximetry: theory for the future," *Anesthesia and Analgesia*, vol. 105, no. 6, pp. S53-S58, 2007.

[79] J. Kraitl, H. Ewald, and H. Gehring, "An optical device to measure blood components by a photoplethysmographic method," *Journal of Optics A: Pure and Applied Optics*, vol. 7, pp. S318-S324, 2005.

[80] N. Taguchi, S. Nakagawa, K. Miyasaka, M. Fuse, and T. Aoyagi, "Cardiac output measurement by pulse dye densitometry using three wavelengths," *Pediatric Critical Care Medicine*, vol. 5, no. 4, pp. 343-350, 2004.

[81] Y. Fujita, T. Yamamoto, M. Fuse, N. Kobayashi, and T. Aoyagi, "Pulse dye densitometry using indigo carmine in useful for cardiac output measurement, but not for circulating blood volume measurement," *European Journal of Anaesthesiology*, vol. 21, pp. 632-637, 2004.

[82] S. Bro Dunn, R. G. Haahr, K. Birkelund, and E. V. Thomsen, "A ring-shaped photodiode designed for use in a reflectance pulse oximetry sensor in wireless health monitoring applications," *IEEE Sensors Journal*, vol. 10, no. 2, pp. 261-268, 2010.

[83] Y. Mendelson, R. M. Lewinsky, and Y. Wasserman, "Multi-wavelength reflectance pulse oximetry," *Anesthesia and Analgesia*, vol. 94, pp. S26-S30, 2002.

[84]   S. Reichelt, J. Fiala, A. Werber, K. Forster, C. Heilmann, R. Klemm, and H. Zappe, "Development of an implantable pulse oximeter," *IEEE Transactions on Biomedical Engineering*, vol. 55, no. 2, pp. 581-588, 2008.

[85]   M. Rothmaier, B. Selm, S. Spichtig, D. Haensse, and M. Wolf, "Photonic textiles for pulse oximetry," *Optics Express*, vol. 16, no. 17, pp. 12973-12986, 2008.

[86]   J. Goldman, M. T. Petterson, R. J. Kopotic, and S. J. Barker, Masimo signal extraction pulse oximetry," *Journal of Clinical Monitoring*, vol. 16, pp. 475-483, 2000.

[87]   S. J. Barker, J. Curry, D. Redford, and S. Morgan, "Measurement of carboxyhemoglobin and methemoglobin by pulse oximetry," *Anesthesiology*, vol. 105, pp. 892-897, 2006.

[88]   J. Schoevers, C. Scheffer, R. Dippenaar, "Low-oxygen-saturation quantification in human arterial and venous circulation," *IEEE Transactions on Biomedical Engineering*, vol. 56, no. 3, pp. 846-854, 2009.

[89]   C. Hornberger, P. Knoop, W. Nahm, H. Matz, E. Konecny, H. Gehring, R. Bonk, H. Frankenberger, G. Meyfroidt, P. Wouters, J. Gil-Rodriguez, L. Ponz, K. Benekos, J. Valais, J. Avgerinos, A. Karoutis, A. Ikiades, and S. Weininger, "A prototype device for standardized calibration of pulse oximeters," *Journal of Clinical Monitoring and Computing*, vol. 16, pp. 161-169, 2000.

[90]   C. Hornberger, P. Knoop, W. Nahm, H. Matz, E. Konecny, H. Gehring, J. Otten, R. Bonk, H. Frankenberger, P. Wouters, J. Gil-Rodriguez, L. Ponz, J. Avgerinos, A. Karoutis, A. Ikiades, and S. Weininger, "A prototype device for standardized calibration of pulse oximeters II," *Journal of Clinical Monitoring and Computing*, vol. 17, pp. 203-209, 2002.

[91]   C. Hornberger, H. Matz, E. Konecny, H. Frankenberger, R. Bonk, J. Avgerinos, K. Benekos, J. Valais, A. Ikiades, J. Gil-Rodriguez, P. Wouters, G. Meyfroidt, L. Ponz, and S. Weininger, "Design and validation of a pulse oximeter calibrator," *Anesthesia and Analgesia*, vol. 94, pp. S8-S12, 2002.

[92]   J. Reuss and D. Siker, "The pulse in reflectance pulse oximetry: modeling and experimental studies," *Journal of Clinical Monitoring and Computing*, vol. 18, no. 4, pp. 289-299, 2004.

[93]   F. P. Wieringa, F. Mastik, and A. F. W. van der Steen, "Contactless multiple wavelength photoplethymographic imaging: a first step toward "SpO2 camera" technology," *Annals of Biomedical Engineering*, vol. 33, no. 8, pp. 1034-1041, 2005.

[94] G. J. Michalak, G. P. Goodrich, J. A. Schwartz, W. D. James, and D. P. O'Neal, "Murine Photoplethysmography for *In Vivo* Estimation of Vascular Gold Nanoshell Concentration," *JBO Letters*, (accepted May, 2010).

[95] G. J. Michalak, H. A. Anderson, D. P. O'Neal, "Feasibility of Using a Two-Wavelength Photometer to Estimate the Concentration of Circulating Near-Infrared Extinguishing Nanoparticles," *Journal of Biomedical Nanotechnology*, vol. 6, no. 1, pp. 73-81, 2010.

[96] D. P. O'Neal, L. R.Hirsch, N. J. Halas, J. D. Payne, J. L. West, "Photo-thermal tumor ablation in mice using near infrared-absorbing nanoparticles," *Cancer Letters*, vol. 209, 171-176, 2004.

[97] C. Loo, A. Lowery, N. Halas, J. West, R. Drezek, "Immunotargeted nanoshells for integrated cancer imaging and therapy," *Nano Letters*, vol. 5, 709-711, 2005.

[98] G. F. Paciotti, D. Weinreich, D. Goia, N. Pavel, R. E. McLaughlin, L. Tamarkin, "Colloidal Gold: A Novel Nanoparticle Vector for Tumor Directed Drug Delivery," *Drug Delivery*, vol. 11, 169-183, 2004.

[99] E. C. Bradley and J. W. Barr, "Determination of blood volume using indocyanine green (Cardio-Green®) dye," *Life Sciences*, vol. 7, 1001-1007, 1968.

[100] J. B. Jackson, S. L. Westcott, L. R. Hirsch, J. L. West, N. J. Halas, "Controlling the surface enhanced Raman effect via the nanoshell geometry," *Applied Physics Letters*, vol. 82, 257-259, 2003.

[101] S. A. Glantz, *Primer of Biostatistics*, New York, NY, McGraw-Hill, 1997.

[102] W.D. James, L. R. Hirsch, J. L. West, P. D. O'Neal, and J. D. Payne, "Application of INAA to the build-up and clearance of gold nanoshells in clinical studies in mice," *Journal of Radioanalytical and Nuclear Chemistry*, vol. 271, no. 2, 455-459, 2007.

[103] D. C. Montgomery, E. A. Peck, and G. G. Vining, *Introduction to Linear Regression Analysis: Fourth Edition*, Hoboken, NJ, Wiley & Sons, Inc., 2006.

[104] A. J. Welch and M. J. C. van Gemert, *Optical-Thermal Response of Laser-Irradiated Tissue*, New York, NY, Plenum Press, 1995.